Hydrogen in Motorsport

Liquid Hydrogen Storage System Study of a High Performance Vehicle

ME55035: ME-EFPT MSc Thesis

Tommaso Longoni

Delft University of Technology

Hydrogen in Motorsport

Liquid Hydrogen Storage System Study of a High Performance Vehicle

by

Tommaso Longoni

Student Number:	5110688
University Supervisor:	Emanuele Zanetti
Company Supervisor:	Amedeo Alberti

Cover: Dallara Stradale at Track Day
Style: TU Delft Report Style, with modifications by Daan Zwaneveld

Acknowledgments

This thesis has offered me a truly unique opportunity for me to combine my studies with my passion for the motorsport industry. My time at Dallara has been filled with invaluable learning experiences and inspiring connections, serving as a natural bridge between my academic background and the professional world. I am sincerely thankful to my supervisor Amedeo Alberti and Aldo Costa for giving me the chance to work within a world class automotive company and contribute to such an exciting project, as well as Massimo Stellato and Elisa Serioli for their support throughout the work.

I would also like to express my heartfelt thanks to my university supervisor Emanuele Zanetti and Marloes Peeters-Reus, for supporting my ambition and making it possible for me to pursue this dream. Organizing such an opportunity was not without any challenges, but it has definitely been worth the effort.

Furthermore, I am deeply thankful to the University of Delft for allowing me to spend a year at Forze Hydrogen Racing. That experience has been of major importance in my academic journey and played a fundamental role in shaping my career aspirations within motorsport. This thesis represents a continuation of the mission I carried out at Forze, and I am proud to be making my contribution towards a more sustainable future for racing.

This journey has been filled with emotions, learning and growth and I am grateful to everyone who has been part of this chapter of my life. I look forward with excitement to the opportunities that lie ahead.

Thank you

Tommaso Longoni
Delft, September 2025

Abstract

The transition to alternative propulsion technologies is driving the development of hydrogen powered vehicles in both road and motorsport applications. Liquid hydrogen offers significant advantages compared to other sustainable fuels due to its high energy density, making it a compelling solution for high performance racing. This thesis investigates the design and simulation of a liquid hydrogen storage system for a fuel cell electric vehicle developed in collaboration with Dallara Automobili S.p.A. and within the regulatory framework of the FIA.

A modular, system level 1D model of the complete LHSS was developed to evaluate the integration of a cryogenic tank, pump, and heat exchanger into the Dallara Stradale platform. The study addresses key research questions concerning the performance of liquid versus gaseous hydrogen storage, the optimization of tank and heat exchanger design and thermal behavior, and alternative system layouts.

Simulation results show that, despite packaging constraints and the Dallara Stradale's architecture, a liquid hydrogen configuration can achieve competitive dormancy and boil-off performance. The heat exchanger analysis highlights the potential for radiator downsizing when effectively integrated with the vehicle cooling system. Sensitivity analyses on insulation, ambient temperature, and MLI quality further underline the critical role of thermal management in achieving robust and predictable operation.

This work provides a validated modeling framework for the design of LHSS in motorsport applications and delivers key insights for future development. The results support the feasibility of liquid hydrogen as a high performance racing fuel while identifying key technological gaps such as pump reliability, insulation robustness, and system calibration that must be addressed to enable competitive hydrogen powered vehicles.

Contents

Nomenclature

Abbreviations

Abbreviation	Definition
1D	One Dimensional
3D	Three Dimensional
AC	Alternate Current
ACO	Automobile Club de l'Ouest
BOG	Boil-Off Gas
BOP	Balance of Plant
CAD	Computer-Aided Design
CFD	Computational Fluid Dynamics
CHF	Critical Heat Flux
DC	Direct Current
EV	Electric Vehicle
EMS	Energy Management Strategies
ESS	Energy Storage System
EGW	Ethylene Glycol Water Mixture
FC	Fuel Cell
FIA	Federation Internationale de l'Automobile
FCEV	Fuel Cell Electric Vehicle
GT	Gamma Technologies
GH2	Gaseous Hydrogen
ICE	Internal Combustion Engine
LH2	Liquid Hydrogen
LHSS	Liquid Hydrogen Storage System
MHF	Minimum Heat Flux
MLI	Multi-Layer Insulation
MEOP	Maximum Exceedable Operating Pressure
NTU	Number of Heat Transfer Units
NASA	National Aeronautics and Space Administration
NIST	National Institute of Standards and Technology
PU	Power Unit
PHE	Plate Heat Exchanger
PRV	Pressure Relief Valve
PFHE	Plate-Fin Heat Exchanger
PEMFC	Proton Exchange Membrane Fuel Cell
P&ID	Piping and Instrumentation Diagram
SAS	Scale Adaptive Simulation
SOC	State of Charge
STI	Scientific and Technical Information
VOF	Volume of Fluid

Symbols

Symbol	Definition	Unit
H_2	Hydrogen	$[-]$
H^+	Hydrogen ions	$[-]$
e^-	Electron	$[-]$
O_2	Oxygen	$[-]$
H_2O	Water	$[-]$
A	Area	$[m^2]$
AR	Flow channels aspect ratio	$[-]$
$\%bb$	Brake bias	$[\%]$
Bo	Boiling number	$[-]$
c	Specific heat	$[J/kgK]$
Co	Convection number	$[-]$
CS	Aerodynamic drag coefficient	$[-]$
C_f	Fanning friction factor	$[-]$
C_{batt}	Battery capacity	$[kWh]$
$C_{H_2,eq}$	Equivalent hydrogen consumption	$[\%]$
C	Capacitance	$[F/mAh]$
dx	Length of mass element in the flow direction	$[mm]$
dp	Pressure differential acting across dx	$[bar]$
D	Diameter	$[mm]$
E	Voltage	$[V]$
Fr	Froude number	$[-]$
F_{12}	Surface view factor	$[-]$
F	Faraday constant	$[C/mol]$
g	Gravity	$[m/s^2]$
Gr	Grashof number	$[-]$
h_{in}	Inlet enthalpy	$[kJ/kg]$
h_{out}	Outlet enthalpy	$[kJ/kg]$
Δh_s	Isentropic enthalpy change	$[kJ/kg]$
h	Heat transfer coefficient	$[W/m^2K]$
h_{chan}	Channel Height	$[mm]$
h_λ	Enthalpy of vaporization	$[kJ/kg]$
H_p	Pump pressure head	$[m]$
H	Total specific enthalpy	$[J/kg]$
H_{tank}	Tank height	$[mm]$
I	Current	$[A]$
Ja	Jakob number	$[-]$
k	Thermal conductivity	$[W/mK]$
K_p	Pressure loss coefficient	$[-]$
l	Filling level	$[mm]$
L	Length	$[mm]$
$\dot{m}$	Mass flow rate	$[kg/s]$
m	Mass	$[kg]$
m''	Mass flux	$[kg/m^2/s]$
M	Molecular mass	$[g/mol]$
MC	Main channel length	$[mm]$
n	Units	$[-]$
NTU	Number of heat transfer units	$[-]$
Nu	Nusselt number	$[-]$
p	Pressure	$[bar]$
P	Power	$[W]$
Pr	Prandtl number	$[-]$
q	Heat flux	$[W/m^2]$

Symbol	Definition	Unit
qt	Quality	$[-]$
Q	Heat transfer rate	$[W]$
Q_c	Stored charge	$[C]$
r	Tire rolling radius	$[mm]$
Re	Reynolds number	$[-]$
R_f	Fouling resistance	$[m^2K/W]$
R	Thermal resistance	$[K/W]$
s	Thickness	$[mm]$
SoC	State of Charge	[%]
S	Range	$[km]$
SH	Stack height	$[mm]$
t	Time	$[s]$
T	Temperature	$[K]$
T_m	Motor torque	$[Nm]$
u	Internal Energy	$[J/kg]$
U	Overall heat transfer coefficient	$[W/m2K]$
v	Velocity	$[m/s]$
V	Volume	$[l]$
W	Width	$[mm]$
We	Weber number	$[-]$
Y	Distance	$[mm]$
α	Heat capacity ratio	$[-]$
β	Volume expansion ratio	$[-]$
γ	Specific heat ratio of incoming gas	$[-]$
δ	Fuel utilization coefficient	$[-]$
ϵ_{eff}	Effectiveness	$[-]$
ϵ	Emissivity	$[-]$
η	Efficiency	$[-]$
μ	Dynamic viscosity	$[Pas]$
ν	Kinematic viscosity	$[m^2/s]$
ρ	Density	$[kg/m^3]$
σ	Boltzmann constant	$[J/K]$
χ	Relative humidity	$[-]$
ω	Angular velocity	$[rad/s]$

1

Introduction

With the recent urbanization and growth of the world's population and economy, a considerable increase in energy demand has occurred. Today, most of the global consumption of energy is fulfilled by fossil fuels, which are being diminished dramatically [1]. Energy that is generated in such way has a significant increase in greenhouse gases and CO_2 in the environment, causing adverse climate changes. Researchers, supported by the policies established in the Paris Agreement [2], have developed their interested in sustainable and green energy systems to tackle this challenge.

To this day, hydrogen represents one of the most promising chemical elements and a candidate for revolutionizing the energy transitions in the transport sector. Even though still in its infancy, the application of hydrogen in the transport sector is being studied by different research institutions worldwide with encouraging results [3].

In this context, the motorsport industry is feeling increasing pressure to find sustainable alternatives to the petrol powered internal combustion engine (ICE) [4]. The main regulatory body in the world championships of motorsport, the FIA, has declared to become carbon neutral by 2030 [5]. This implies introducing clean energy in all world championship cars by the same year. To achieve this goal racing cars, originally powered by gasoline, will need to change their energy source. One viable option is represented by hydrogen, which comes with either internal combustion engines (ICE) or fuel cells (FC).

Hydrogen cars are being explored as sustainable racing vehicles by multiple different organizations. The first hydrogen-powered off-road motorsport Extreme H has been launched as evolution of the electric powered class Extreme E [6]. Additionally, the mission of promoting the potential of hydrogen in motorsport is being carried out by the dutch student team Forze Hydrogen Racing [7]. Their recently developed hydrogen fuel cell prototype Forze IX is designed to further push the boundaries of performance, thus making it a competitive alternative to conventional racing cars.

Hydrogen can be stored in liquid (LH2) or gaseous form (GH2), with considerable differences in storage capacity and system architecture. In the recent ACO press conference, liquid hydrogen emerged as the preferable fuel for sporting competitiveness [8]. For this purpose, the french team Mission H24 is exploring this new technology, thus serving as a testbed for a future hydrogen class in the endurance championship [9].

This project also involves the Italian car manufacturer Dallara Automobili s.p.a., which has been actively engaged in various initiatives related to hydrogen mobility. In particular, the company is collaborating with the FIA and ACO on the design and development of a high performance vehicle powered by liquid hydrogen. The thesis work is carried out at this company and aims to support this effort by developing a model of the liquid hydrogen storage system (LHSS) for a fuel cell vehicle. The work focuses on analyzing the individual components of the LHSS and their interaction on a system-level as well as in relation to the rest of the vehicle.

Chapter 2 presents the relevant background on liquid hydrogen storage solutions, the principles of the technology and previous models found in literature. In Chapter 3 the models developed in this work are explained, along with the relevant theory of heat transfer and fluid dynamics, and the simulated cases are outlined. The outcomes are reported in Chapter 4, followed by a critical discussion in Chapter 5. Chapter 6 provides a conclusion answering the research questions and recommendations for future work.

2

Background

This chapter will go into the supporting literature and background knowledge needed to understand the thesis and put its work into context of the research carried out so far. Additionally, the scope of the thesis will be highlighted by research questions and the plan proposed to tackle those.

At first, the current state of the research, including the gaps this research aims to fill, will be summarized in section 2.1. An overview on liquid hydrogen as sustainable fuel will be provided, with a focus on the challenges related to its application. To support this study, a modeling approach found in literature of the different subsystems that will be analyzed is presented. At last, the scope of the research will be defined with its corresponding plan in section 2.2.

2.1. Current State of the Art

Liquid hydrogen has been explored as fuel for mobility for the past years as a possible alternative. An overview on its recent history and major milestones is provided in [10]. This paper highlights two major fields of application in which this technology has been applied:

- automotive
- aerospace

In the 1990s and early 2000s BMW explored hydrogen technology by developing both liquid hydrogen ICE and FC powered experimental vehicles [11]. Similarly, Japanese manufacturer Toyota has been committing to the success of a hydrogen ecosystem for decades already, introducing commercial light-and heavy-duty gaseous hydrogen vehicles in the market [12]. More on the application of hydrogen in automotive engineering can be found in [13]. More, during the past decades the space industry has been using liquid hydrogen for rockets. This paper by the NASA Scientific and Technical Information (STI) program [14] explores the key design issues and potential solutions for liquid hydrogen storage systems for aircraft applications.

As previously mentioned, liquid hydrogen has increasingly gained popularity as alternative fuel for motorsport. The FIA has agreed upon introducing a hydrogen class at the highest level of endurance racing. This includes the world's famous 24h of Le Mans race, which is known for showcasing the latest innovations in the sector. During the last edition of the event, car manufacturer and WEC constructor Toyota Gazoo Racing revealed their liquid hydrogen racing concept, which is set to drive the development of this technology in motorsport [15].

Hydrogen has a specific energy (energy per unit mass) three times that of gasoline. However, its energy per unit volume (or equivalently, its density) is low, making hydrogen the lightest element in the Universe. In gaseous form, it is stored at 350 bar or 700 bar and has a density of 40 kg/m^3 at 700bar. In liquid form, its density is 71 kg/m^3 at a pressure of 1 bar, which is equivalent to atmospheric pressure [16]. In the context of racing, where the vehicle is subject to high g-forces, a low-pressure storage condition such as this poses a much lower hazard concern [17], [18].

According to the phase diagram of hydrogen [19], to be in liquid form, it has to be stored at a temperature of approximately $-253\,°C$, or $20\,K$, in thermally insulated tanks. An evaporation system, followed by a heat exchanger, is required to adapt its temperature to the fuel cell use, where gaseous hydrogen is used.

An overview of such process plant is provided by the simplified schematic in figure 2.1.

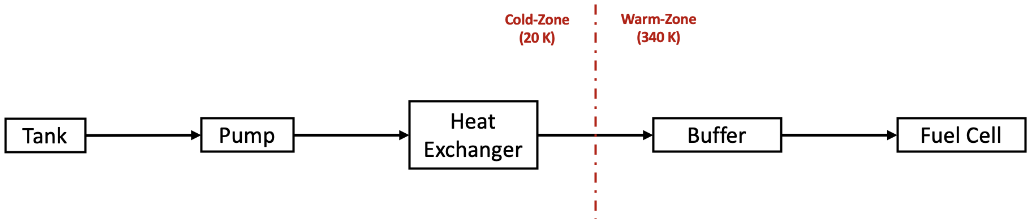

Figure 2.1: Liquid Hydrogen Storage System - Simplified Plant Overview

Another widely used method for storing hydrogen is in its gaseous state. In this configuration, hydrogen is delivered directly to the power unit, with a system consisting of a pressure regulator and prop valve regulating the supply pressure and temperature. This approach offers a simpler storage solution, as it eliminates the need for additional auxiliary systems to process the fuel. An illustration of this storage setup is shown in figure 2.2.

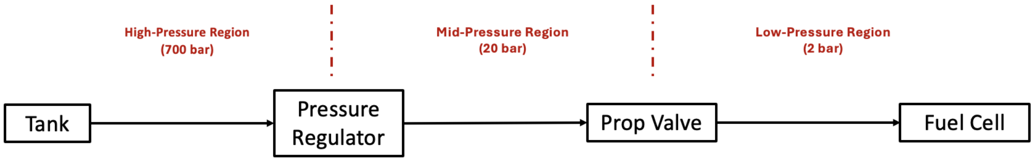

Figure 2.2: Gaseous Hydrogen Storage System - Simplified Plant Overview

These two fuel supply systems are integrated into a vehicle which is powered by either a fuel cell or an internal combustion engine operating on hydrogen. As outlined in chapter 1, the case study of this work focuses on a high-performance fuel cell vehicle developed by Dallara, originally designed with a gaseous hydrogen storage system. Consequently, sections 2.1.1, 2.1.2 and 2.1.3 present an overview and modeling approach of the key components of a fuel cell electric powertrain and the proposed liquid hydrogen storage solution.

2.1.1. Powertrain

This section outlines the modeling approach adopted for the primary components of a fuel cell electric vehicle. Although the core focus of this work lies in the liquid hydrogen storage system, its interaction with the overall vehicle is also taken into account. Therefore, a general understanding of the functionality and modeling of these key subsystems is essential to enable a comprehensive analysis of the integrated system.

At first, an overview of the various sub-systems of a fuel cell electric vehicle (FCEV) powertrain will be provided. Their modeling approach together with the tools provided by the GT Suite software will be introduced. A simplified schematic of these systems is presented in figure 2.3.

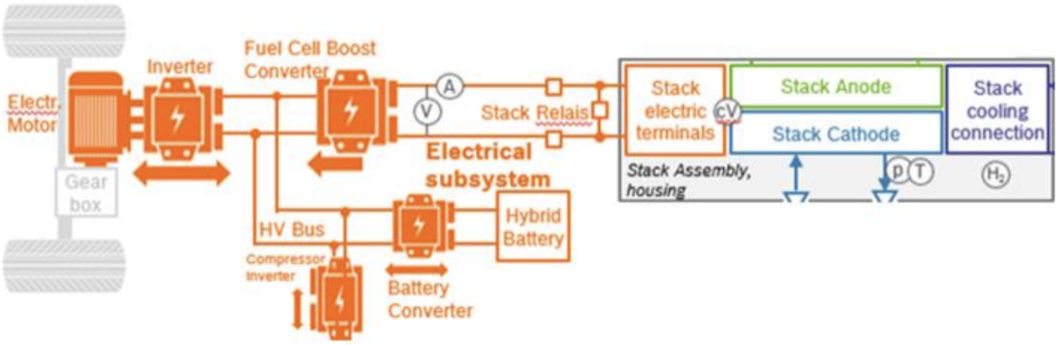

Figure 2.3: Vehicle Powertrain Macro Overview - concept study (provided by Dallara)

Looking at Figure 2.3, there are four components that need to modeled:

- **Fuel Cell Stack:** the stack is the main source of energy of the car and serves as substitute to the conventional battery of electric vehicles (EV). The different components of the balance of plant (BoP) will be individually approached in section 2.1.2.
- **Hybrid Battery:** energy buffer of the car that allows to compensate for the peak power demands of the vehicle that the fuel cell can't provide. These battery power cells allow to store energy while braking and increase the peak power output.
- **DC/DC Converter:** fuel cell boost converter is used to convert the relatively low voltage provided by the stack to the higher operating voltage of the accumulator. The higher voltage also allows the electro motors to use more power and operate more efficient as there are less ohmic losses. The battery converter can act as a power regulator, allowing for control of the power split between the fuel cell and the battery, thus enabling efficient energy management.
- **Electric Motor and Inverter:** electric power produced by the fuel cell and the energy stored in the battery supply the motor and inverter system, which drives the wheels. These components can also function in generator mode, recovering kinetic energy from the wheels when braking and converting it into electrical energy to be stored in the battery.

Fuel Cell Stack

Since most fuel cells used in automotive applications are Proton Exchange Membrane Fuel Cells (PEMFCs) [20], [21], [22], this subsection primarily focuses on them. However, the fundamental principles discussed also apply to other type of fuel cells. The entire fuel cell stack can be modeled in GT-Suite using a specific template. This combines the flow, thermal, electrical, and chemical domains.

At its core, a fuel cell is a simple system with no moving parts. It consists of two electrodes, anode and cathode, separated by an electrolyte. Each electrode facilitates a specific reaction:

- **Anode Reaction:** hydrogen entering the fuel cell splits into protons (H^+ ions) and electrons (e^-) as described by equation 2.1. The H^+ ions pass through the electrolyte (proton exchange membrane) to reach the cathode.

  $$2H_2 \longrightarrow 4H^+ + 4e^- \tag{2.1}$$

- **Cathode Reaction:** at the cathode, H^+ ions combine with oxygen (O_2) and the electrons that have traveled through an external circuit, where energy is extracted. This reaction produces water as the final byproduct, as shown in equation 2.2.

  $$O_2 + 4e^- + 4H^+ \longrightarrow 2H_2O \tag{2.2}$$

These reactions are also illustrated in figure 2.4.

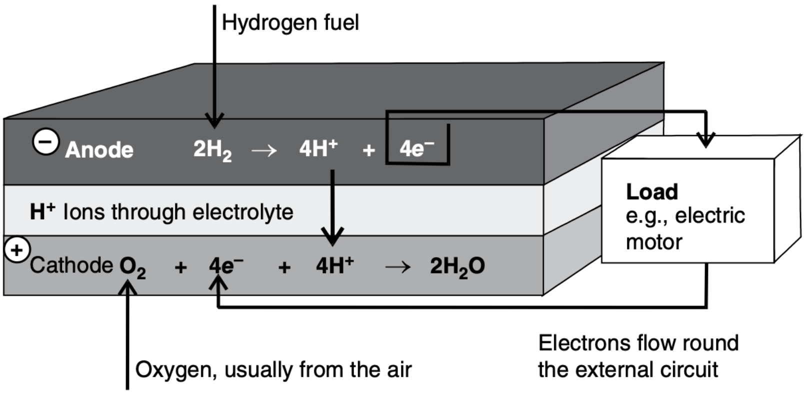

Figure 2.4: Fuel Cell Schematic [21] - Electrode reactions and charge flow for fuel cell with an acid electrolyte

The overall reaction within the fuel cell is:

$$2H_2 + O_2 \longrightarrow 2H_2O + electricity + heat \tag{2.3}$$

This process results in the generation of electrical energy while producing water as primary byproduct, while releasing some waste heat. The heat production must be carefully managed to ensure that the FC works in the correct range of temperature and membrane humidity, which are fundamental aspects that affect the system lifetime.

The module shown in figure 2.4 represents a single fuel cell, which generates a relatively low voltage, typically ranging between $0.6\,V$ and $1.2\,V$. The fuel cell stack is built by assembling in parallel configuration e multitude of these single cells. The exact voltage depends on various factors and serves as an indicator of the cell's efficiency, which can be calculated using equation 2.4:

$$\eta_{cell} = \delta_f \frac{E_{cell}}{E_{oc}} \tag{2.4}$$

where:

- η_{cell}: cell efficiency
- E_{cell}: cell voltage
- E_{oc}: open circuit voltage, representing the maximum theoretical voltage if all the energy from the hydrogen fuel (its calorific value) were converted into electrical energy. Typical values for E are $1.25\,V$ (lower heating value) and $1.48\,V$ (higher heating value).
- δ_f: fuel utilization coefficient, accounting for the fact that not all hydrogen is consumed in the reaction. A common approximation is $\delta_f \approx 0.95$ [21].

The voltage E_{cell} is influenced by several factors, including temperature, pressure, reactant concentration, and the current drawn by the load. Under steady conditions, often referred to as reference conditions, the relationship between the voltage and current can be illustrated by a polarization curve, as shown in figure 2.5.

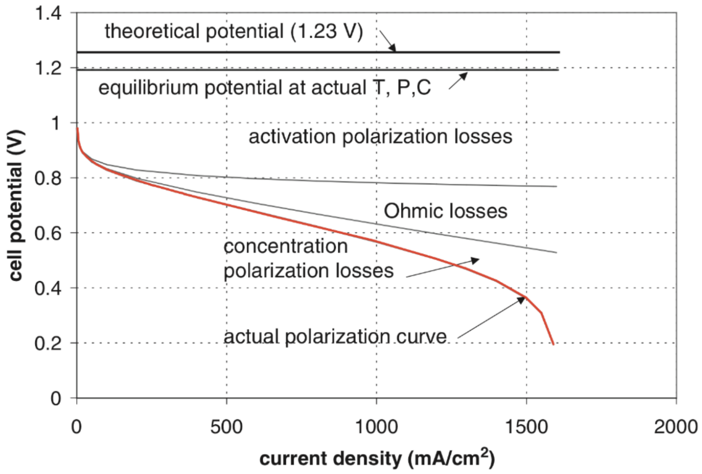

Figure 2.5: Polarization Curve including voltage losses (red line) [20]

As shown in figure 2.5, the cell voltage decreases as the current density increases. The voltage drop is caused by four main irreversibilities within the fuel cell which are also modeled in GT Suite.

- activation losses E_{act}
- fuel crossover and internal currents $E_{oc,loss}$
- ohmic losses E_{ohm}
- concentration losses E_{conc}

All these voltage losses contribute to a reduction of the fuel cell potential 2.5, which affects the system efficiency as shown through equation 2.4.

$$E_{cell} = E_{oc} - E_{oc,loss} - \Delta E_{ohm} - E_{act} - \Delta E_{conc} \tag{2.5}$$

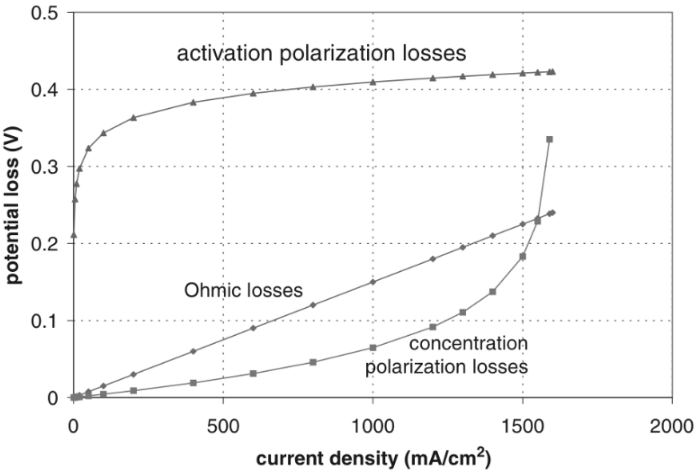

Figure 2.6: Losses Overview - voltage losses versus current density [20]

The polarization curve allows for determining the required current to achieve a specific power output from a fuel cell. Since power is given by the equation

$$P_{cell} = E_{cell} \cdot I_{cell} \tag{2.6}$$

the power output of a single fuel cell is very limited. To generate sufficient power for a road vehicle, a single cell would require impractically high currents.

To overcome this limitation, multiple fuel cells are connected in series, forming a fuel cell stack. This stack operates with its own polarization curve, which retains the same characteristic as figure 2.5, but now plots current on the x-axis for a specific stack configuration. An example of a fuel cell stack polarization curve is shown in figure 2.7.

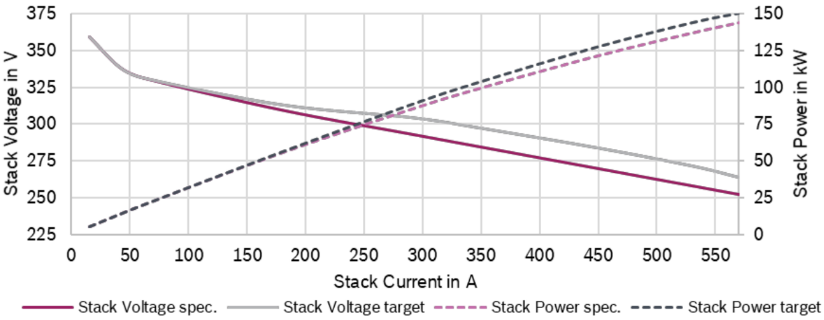

Figure 2.7: Polarization curve of a stack used for automotive applications (provided by Dallara) - stack voltage and power versus stack current

Once the operating point on the polarization curve is selected, the hydrogen consumption can be calculated using equation 2.7:

$$\dot{m}_{H_2} = \frac{I_{FC} M_{H_2}}{2F} \tag{2.7}$$

where:

- I_{FC}: current drawn from the stack
- F: Faraday constant
- M_{H_2}: molecular mass of hydrogen

Several methods can be used to model the fuel cell behavior, with the primary goal of predicting the power output and hydrogen consumption accurately. These include:

- empirical polarization curve model
- electrochemical model
- equivalent circuit model

While the first two have been described above and are also used in GT-Suite, the latter one provides an alternative approach to the modeling.

Energy Storage System

During vehicle operation, peak power demands are frequent. As previously mentioned, fuel cells do not have ideal dynamic capabilities, so they require a certain amount of time to respond to step load requests. To compensate for this delay and support the fuel cell system under maximum power conditions, an additional energy storage system (ESS) is almost always employed.

The ESS is an essential component of the FCEV for several reasons:

- stress reduction on the fuel cell during dynamic acceleration
- regenerative braking enabling
- power supply to the compressor during vehicle start-up
- fuel cell warm up in low-temperature conditions
- energy management strategies (EMS) enabling to optimize system efficiency

The two main types of ESS used are supercapacitors (supercaps) and/or batteries:

- supercapacitors provide high power density and have high charging/discharging efficiency, along with long lifetimes. However, their major drawback is a much lower energy density compared to batteries [23].
- batteries are more commonly used in FCEVs because they offer a balance of acceptable dynamic performance and higher energy density, making them suitable for hybrid vehicle applications [24].

To accurately capture the power-limiting effects near the operational limits of these devices, a modeling approach is required that enables the calculation of both their state of charge (SoC) and terminal voltage.

The SoC is often modeled using coulomb counting [25]. The voltage across the device can be determined using equation 2.8:

$$E_c = \frac{Q_c}{C} \tag{2.8}$$

where:

- Q_c: stored charge
- C: capacitance

Using coulomb counting, the state of charge can be calculated as:

$$I_c = \frac{dQ_c}{dt}, \quad SoC = \int \frac{I_c dt}{C(SoC)} \tag{2.9}$$

where:

- I_c: current through device
- $C(SoC)$: capacitance, which is often dependent on SoC

Various models exist for predicting the terminal voltage, differing in accuracy, computational cost and complexity.

- static RC circuit
- Thévenin model

DC/DC Converter

Since the fuel cell's output voltage differs from the battery's, a DC-DC converter is required to electrically connect the two systems. The converter can be placed on the battery side and/or on the fuel cell side. The efficiency of this conversion depends on input and output voltages, as well as the converted current. While studies such as [26], [27] propose models to quantify DC/DC converter losses, these have been considered outside the scope of this thesis, particularly since the efficiency data for the DC/DC converter is available. Simulation tool GT-Suite uses a simple map-based (efficiency map) model.

Electric Motor

The electric motor and inverter convert electrical energy into mechanical energy for propulsion and can also operate in regenerative mode, converting mechanical energy back into electricity. The power output of the electric motor is given by equation 2.10 [28]:

$$P_{m,motor} = \frac{T_m \cdot \omega_m}{\eta_m(\omega_m, T_m)} \tag{2.10}$$

$$P_{m,generator} = T_m \cdot \omega_m \cdot \eta_m(\omega_m, T_m) \tag{2.11}$$

where:

- $P_{m,motor}$: motor power output

- $P_{m,generator}$: generator power output
- T_m: motor torque
- ω_m: motor angular velocity
- $\eta_m(\omega_m, T_m)$: efficiency of the motor, which varies with speed and torque

The electric motor requires an inverter (for AC motors) to convert the DC voltage from the fuel cell and ESS into an AC signal. The inverter's efficiency can be:

- included in the motor efficiency model [29]
- modeled separately using a constant efficiency factor [30]

Additionally, most electric motors cannot directly drive the wheels, requiring a fixed-gear transmission. The efficiency of this gear system is typically modeled as a constant factor [31]. The motor efficiency (η_m) can be determined using different methods such as:

- efficiency maps [28]
- Willans Approach [28]

2.1.2. Balance of Plant

The fuel cell stack alone is insufficient to power the vehicle. It requires additional components to regulate the supply of reactants. The complete fuel cell system, including these auxiliary components, is commonly referred to as the Balance of Plant (BoP) [20]. These can be further divided into components that process air and hydrogen, which represent the cathode and anode subsystems respectively. An initial modeling approach will be provided, with a focus on the liquid hydrogen storage system (LHSS).

The auxiliary systems can be modeled using the following approaches:

- **Fuel Cell Power Dependent:** the simplest method assumes that the auxiliary components consume a fixed percentage of the fuel cell stack power
- **Mass Flow Dependent:** alternatively, the power consumption of auxiliary components (e.g. compressor, hydrogen recirculation device, cooling water pump) can be determined based on their operating conditions. This approach utilizes different models presented in literature to estimate power demand more accurately [32], [33].

Cathode Subsystem

The cathode subsystem supplies oxygen (O_2) from air to the cathode side of the fuel cell. Proper management of airflow, pressure, humidity, and temperature is crucial for maintaining fuel cell efficiency and longevity. A simplified schematic of these systems is presented in figure 2.8.

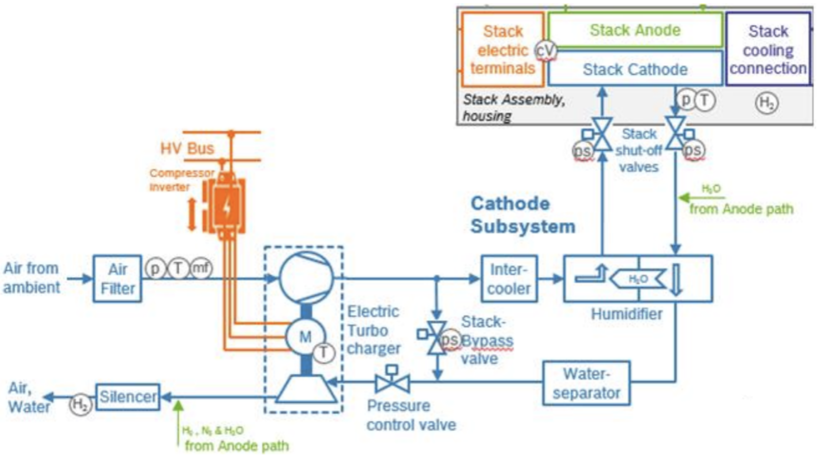

Figure 2.8: Cathode Subsystem Macro Overview - concept study (provided by Dallara)

The different components illustrated in figure 2.8 are described below:

- **Compressor:** increases the pressure of incoming air to enhance oxygen availability at the cathode. Typically electrically driven and controlled for optimal air supply based on power demand.
- **Turbine:** extracts energy from exhaust gases exiting the cathode. Typically coupled with the compressor to recover energy and improve the overall system efficiency.
- **Humidifier:** ensures the air is entering the cathode is sufficiently humidified to prevent the membrane from drying out. Uses water vapor from exhaust gases or external water sources to maintain the correct hydration level.
- **Intercooler:** cools the compressed air before in enters the cathode, reducing thermal stress on the fuel cell membrane. Liquid-to-air heat exchanger that helps maintain optimal operating temperatures and improves compressor efficiency by reducing the required compression work.

Anode Subsystem

The anode subsystem is responsible for delivering hydrogen (H_2) to the anode side of the fuel cell, where it undergoes an electrochemical reaction. Proper management of hydrogen flow, pressure, and utilization is essential for fuel cell efficiency and durability. A simplified schematic of these systems is presented in figure 2.9.

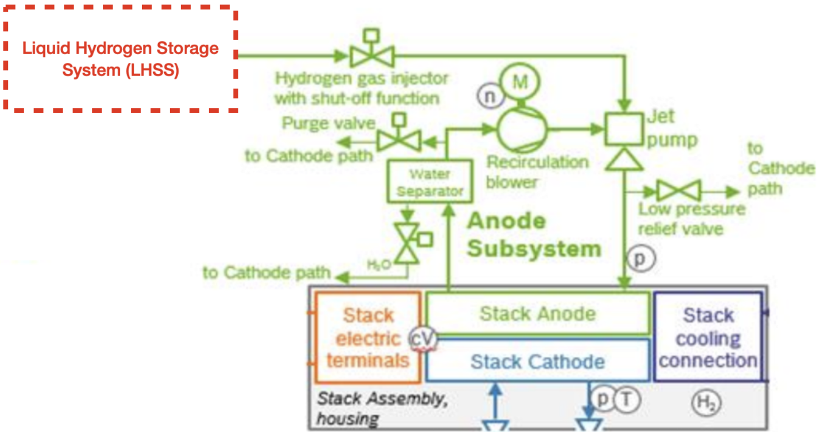

Figure 2.9: Anode Subsystem Macro Overview - concept study (provided by Dallara)

The different components illustrated in figure 2.9 are described below:

- **Hydrogen Recirculating System:** since not all hydrogen is consumed in a single pass through the anode, a hydrogen recirculating system improves fuel utilization and ensures efficient operation by reusing unreacted hydrogen.
- **Liquid Hydrogen Storage System**: represents the system consisting of the cryogenic components that are required to store, regulate and deliver hydrogen in its supercooled state. These components will be further evaluated in section 2.1.3.

2.1.3. Liquid Hydrogen Storage System

The liquid hydrogen storage system (LHSS) is responsible for storing, handling, and delivering hydrogen in its cryogenic liquid state to the fuel cell system. This system is designed to minimize boil-off losses, maintain safe pressure levels, and efficiently convert hydrogen into its gaseous state for use in the fuel cell. A simplified schematic of these systems is presented in figure 2.10.

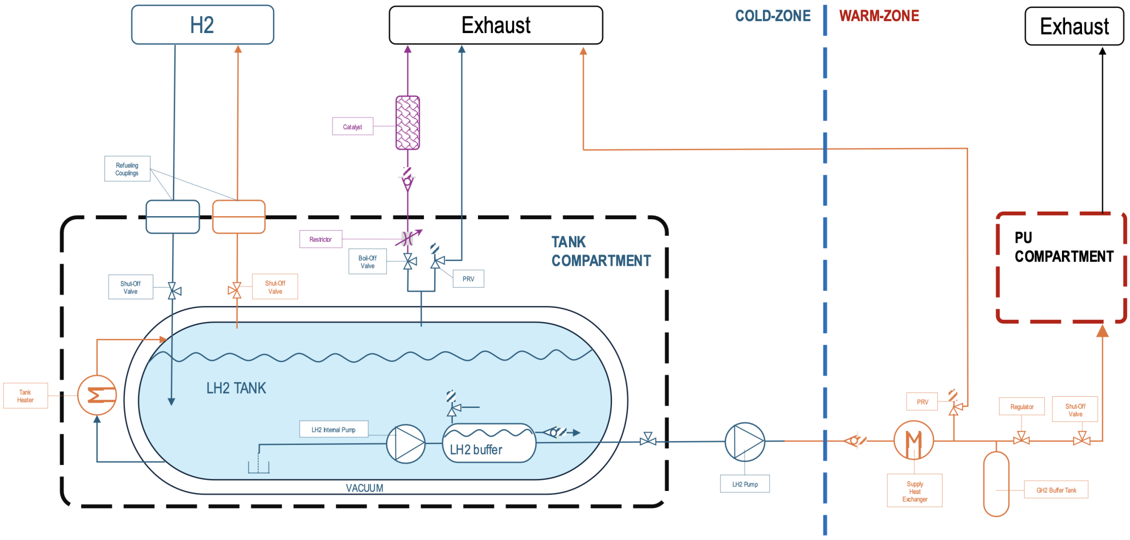

Figure 2.10: Liquid Hydrogen Storage System (LHSS) Macro Overview (provided by Dallara)

Figure 2.10 displays the path that the hydrogen follows from the refueling receptacle up to the exhaust. The cold-zone and warm-zone indicate the area where hydrogen is present at a cryogenic liquid or gas. The different components illustrated in figure 2.10 are described below:

- **Storage Tank:** stores liquid hydrogen while minimizing heat transfer. Uses vacuum insulation and multi-layer insulation (MLI) to reduce boil-off gas (BOG) losses. Designed to handle pressure buildup and controlled venting for safety.
- **Cryogenic Pump:** ensures consistent pressure and flow rate for optimal fuel cell operation. Must withstand extreme cryogenic temperatures and pressure fluctuations [34]. To avoid gaseous hydrogen flowing into the pump, an liquid hydrogen buffer may be placed within the tank with its corresponding pump placed at the bottom of the structure.
- **Heat Exchanger:** warms up liquid hydrogen delivered by the pump, converting it into gaseous hydrogen before it reaches the fuel cell (PU compartment).
- **Buffer tank:** acts as a storage to balance pressure variations and regulate gaseous hydrogen supply to the power unit (PU) compartment.
- **Cryogenic Valves (e.g. boil-off valve):** regulate hydrogen flow, pressure, and venting within the system. Include safety relief valves, shut-off valves, and vent valves to ensure system reliability.
- **Exhaust (catalyst):** critical safety component of the exhaust system that handles the vented hydrogen gas. It facilitates the controlled oxidation of hydrogen into water, preventing the risk of hydrogen buildup.

Tank Compartment

Storage at cryogenic temperatures implies major challenges in terms of material properties and efficiency [35]. These can be best summarized with the occurrence of the boil-off phenomenon, which consists of the evaporation of liquid hydrogen within the tank, thus causing a pressure increase in the vessel and the need for release of the hydrogen gas in the atmosphere.

The causes of hydrogen boil-off can be attributed to the following effects [36]:

- **Heat Leaks:** refers to the unintended transfer of thermal energy into the cryogenic storage tank, causing the liquid hydrogen to warm up and vaporize. Advanced materials and insulation techniques are being developed to minimize this.
- **Sloshing:** refers to the movement of liquid hydrogen within the tank due to acceleration, braking or vibrations. This causes an increase in surface area exposure between liquid and gas as well as the mixing between the two, thus enhancing heat transfer.

- **Ortho-to-Para Conversion:** hydrogen exists in two spin isomeric forms known as Ortho-and Para-Hydrogen. The latter dominates at cryogenic temperatures (low-energy state) and slowly, naturally converts to its other form. This exothermic reaction releases heat, further warming the stored liquid hydrogen and increasing boil-off rates.

Additionally, when designing a LHSS, two critical safety and durability concerns are hydrogen leakage and embrittlement effects. Given that hydrogen is the smallest molecule, it can permeate through microscopic gas, seals, and even some materials at the molecular level. This requires high-integrity seals and vacuum insulation to minimize permeation as well as venting and detection systems for the leaked hydrogen, which is colorless, odorless and highly flammable [37].

Effective insulation, tank design, and active thermal management systems are critical to minimizing hydrogen loss, maintaining storage efficiency, and ensuring safe handling of liquid hydrogen. Different studies have already been carried out by research institutions on this matter. These are based on developing models of the LHSS to simulate the aspects mentioned above together with the dormancy, filling and discharge effects. As indicated in detail in section 3.2, dormancy time is defined as the evolution of the pressure profile of the tank before a certain pressure threshold is reached.

Al Ghafri et al. present a model that allows for reliable calculations of the self-pressurization and boil-off losses for liquid hydrogen in different tank geometries and thermal insulation schemes [38]. The model accounts for the heat transfer from the gas to the liquid phase, as well as between each fluid phase and the wall individually. Reference equations of state are used to calculate thermodynamic properties and computer the overall heat transfer coefficients U_{gl}, U_l and U_g. These are predicted as the sum of two convection terms to account for the heat transfer between the tank wall and adjacent fluid layer, and a conductive term describing heat ingress through the tank wall:

$$\frac{1}{U} = \frac{A_{out}}{A_{in}h_{in}} + \frac{A_{out}}{A_e}\frac{s_e}{k_e} + \frac{1}{h_{out}}, \quad A_e = \frac{A_{out} - A_{in}}{ln\left(\frac{A_{out}}{A_{in}}\right)} \tag{2.12}$$

where:

- A_{out}: outer surface area
- A_{in}: inner surface area
- A_e: heat transfer area
- s_e: insulation layer thickness
- k_e: effective thermal conductivity of the multi-layer insulation
- h_{in}: internal convection coefficient
- h_{out}: external convection coefficient

The total amount of heat entering the liquid and gas phases from the boundary and the amount of heat transferred to the liquid phase from the gas phase are presented in equations 2.13:

$$Q_l = (U_l A_l (T_{int} - T_l) + Q_{floor})\Delta t \tag{2.13}$$

$$Q_g = (U_g A_g (T_{int} - T_g) + Q_{roof})\Delta t \tag{2.14}$$

$$Q_{gl} = U_{gl} A_{gl} (T_g - T_l)\Delta t \tag{2.15}$$

where:

- T_l, T_g, T_{int}: liquid, gaseous and interface temperatures
- A_l, A_g: liquid and gaseous areas
- Q_{floor}, Q_{roof}: heat transferred through the roof and floor
- Q_l, Q_g, Q_{lg}: heat transferred through the wall from liquid and gas phase and at the interface

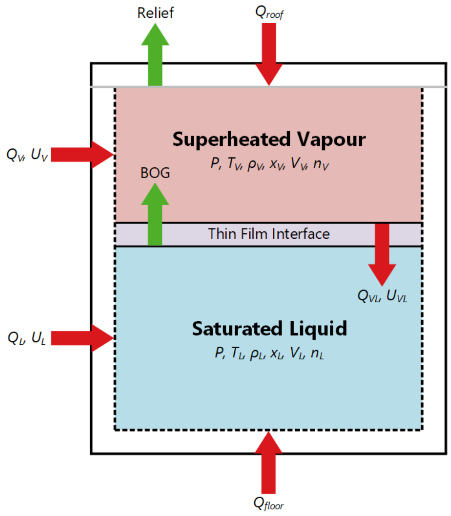

Figure 2.11: Conceptual Schematic of the Tank Model implemented in the BoilFAST tool [38]

The model based on the schematic shown in figure 2.11 uses BoilFAST simulation tool developed to estimate the boil-off from liquid hydrogen storage using a non-equilibrium approach. It proved that existing correlations for manually estimating wall-fluid heat transfer coefficients are sufficiently accurate to allow a robust representation of the boil-off gas phenomena, which provided an adequate detail on the insulation used.

Accurate equations of state and two phase behavior implementations are essential to describe hydrogen behavior (e.g. phase transition, super-heated warming, non-uniform temperature distributions across the saturation film). The balances of mass and energy during the various dynamic processes then enable to quantify the boil-off losses. Petitpas [39] uses a modified MATLAB code from NASA, which implements complex physical phenomena such as the competition between condensation and evaporation and the convection vs. conduction heat transfer as a function of the relative temperatures on both sides of the saturated film.

Models such as the one by Nuwantha et al. [40] present a more precise approach to modeling liquid hydrogen storage by dynamically computing the interfacial temperature rather than assuming saturation conditions. This model is based on the discretization shown in figure 2.12 includes non-equilibrium calculations for the heat and mass transfer across the interface, which is assumed as thin, massless and flat. It provides robust predictions under static conditions but does not include dynamic phenomena such as sloshing.

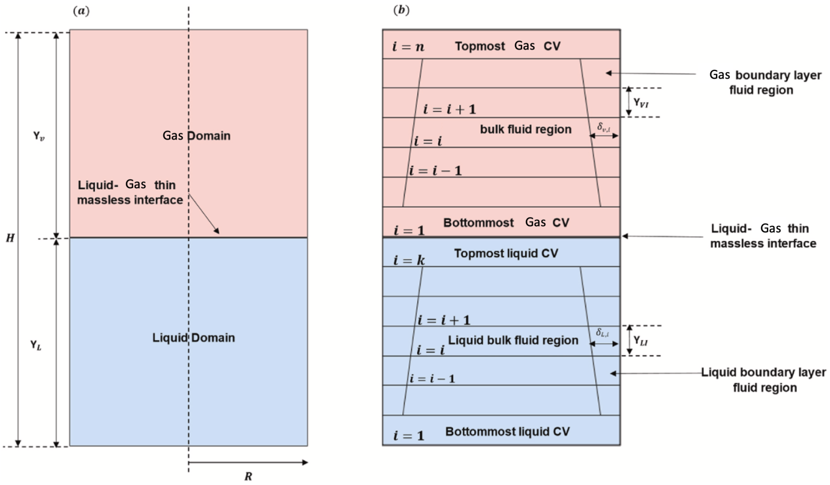

Figure 2.12: Simplified basic tank geometry and discretization [40]

Based on the dominant mode of heat transfer at the interface, the resultant mass transfer rate $\dot{m}_{lg}$ was calculated using the following equation:

$$\dot{m}_{lg} = \frac{Q_{ls} + Q_{gs}}{h_{lg}} \tag{2.16}$$

The term h_{lg} represents the latent heat of vaporization, while Q_{ls} and Q_{gs} can be considered as maximum numerical values based on convection and conduction heat transfer calculations, as shown by equations 2.17:

$$Q_{ls} = max\{Q_{ls}^{cond}, Q_{ls}^{conv}\} \tag{2.17}$$

$$Q_{gs} = max\{Q_{gs}^{cond}, Q_{gs}^{conv}\} \tag{2.18}$$

The heat transfer rate terms Q^{cond} and Q^{conv} represent the conductive and convective heat transfers occurring in the bulk fluid near the liquid-gas interface with respect to the phase. These can be calculated using equations 2.19:

$$Q^{cond} = kA\frac{(T_s - T_{B,i=k(0)})}{Y_{LI}/2} \tag{2.19}$$

$$Q^{conv} = h_{i=k(0)}A(T_s - T_{B,i=k(0)}) \tag{2.20}$$

where:

- $T_{lB,i=k}, T_{gB,i=0}$: bulk temperature at interface
- $Y/2$: ideal distance between T_s and $T_{lB,i=k}$ in liquid side and T_s and $T_{vB,i=0}$ from gas side respectively

The convective heat transfer coefficient can be calculated using equation 2.21:

$$Nu = 0.27Ra^{\frac{1}{4}}; \quad 10^5 < Ra < 10^{10} \tag{2.21}$$

At last, the Department of Aerospace of the University of Michigan provided a python model for the design of liquid hydrogen tanks with the goal of optimizing dormancy times, reducing boil-off and improving pressure management [41].

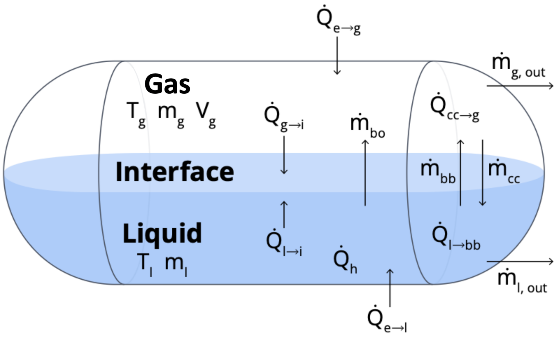

Figure 2.13: Thermodynamic model using three control volumes: gas, interface and liquid. Heat and mass transfer between them and with the external environment

The behavior of the liquid hydrogen in the tank displayed in figure 2.13 is governed by a set of ordinary differential equations for five state variables:

- gas mass

- liquid mass
- gas temperature
- liquid temperature
- gas volume

As the interface is massless, any boil-off mass flow from the liquid to the interface goes straight into the gas. As a result, the conservation of mass for the gas and liquid are:

$$\dot{m}_g = \dot{m}_{bo} - \dot{m}_{g,out} \tag{2.22}$$

$$\dot{m}_l = \dot{m}_{bo} - \dot{m}_{l,out} \tag{2.23}$$

Assuming the liquid is incompressible and the tank volume constant, this provides

$$\dot{V}_g = -\frac{\dot{m}_l}{\rho_l} = -\dot{V}_l \tag{2.24}$$

Applying the conservation of energy to the gas and liquid control volumes will deliver the rates of temperature change. These are derived through equations 2.25 and 2.26:

$$T_g = \frac{Q_{eg} - Q_{gi} - pV_g + \dot{m}_g(h_g - u_g)}{m_g c_{v,g}} \tag{2.25}$$

$$T_l = \frac{Q_{el} - Q_{li} + Q_h(1 - \eta_h) - pV_l + \dot{m}_l(h_l - u_l)}{m_l c_{p,l}} \tag{2.26}$$

This model adds a heater in the liquid portion of the tank in figure 2.13 to induce additional boil-off and prevent the pressure from decreasing too low as well as an estimation to predict the total tank weight. It does not model thermal stratification effects in the gas and assumed the liquid to be incompressible.

For what concerns the valve modeling, the API 520 standard for pressure relief valves (PRV) is employed [42]. These valves start to open at the set pressure, but the valve will be completely open only when a certain overpressure is reached. The blowdown is the difference between the set pressure and the closing pressure (figure 2.14).

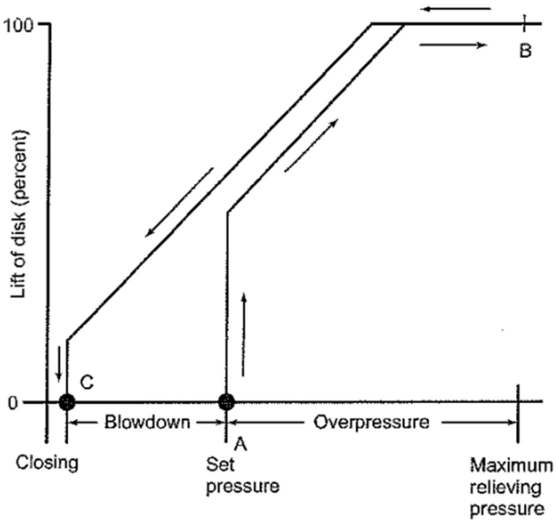

Figure 2.14: Proportional Relief Valve (PRV) sizing manual schematic [42]

Hydrogen at the given condition can be modeled as an ideal gas, for which the expansion relation 2.27 is valid:

$$pV^{\gamma} = constant \tag{2.27}$$

where:

$$\gamma = \frac{c_p}{c_v} \tag{2.28}$$

Heat Exchanger

Heat exchangers that work with cryogenic liquids are subject to some challenges that need to be taken into account in the modeling phase. One potential problem encountered in the operation of such heat exchanger is solidification of the liquid on the cold surface [43]. This would most likely occur at low liquid flow rates and low fluid temperatures. Under extreme conditions, the frozen layer may become thick enough to completely block the flow passage. Even though blockage does not occur, the presence of a frozen liquid layer will affect the heat-transfer characteristic of the heat exchanger.

Additionally, when modeling the thermal performance of a low-pressure cryogenic vaporizer, the effects of axial conduction and phase change of liquefied hydrogen are considered. More, hydrogen atoms diffuse into metals, where they weaken the atomic lattice, causing loss of ductility, crack initiation and premature fracture. At cryogenic temperatures, diffusion rates are lower, but during the heating process hydrogen can enter the metal lattice and accumulate over time [44]. For this reason, additive manufacturing technology is used to minimize this effect and at the same time allow for adaptable geometries to fit adaptable spaces and enable seamless integration.

The heat exchanger (evaporator) is located downstream of the cryogenic pump and responsible for the heating of the hydrogen. While in the pump the fluid is subject to a small temperature increase only, during the evaporation phase, a large enthalpy increase occurs.

A performance analysis model was developed by the modified effectiveness-NTU method, for which a plate-fin heat exchanger (PFHE) was chosen [45]. The operating conditions for the theoretical analysis of the low-pressure vaporizer for liquefied hydrogen are shown in figure 2.15.

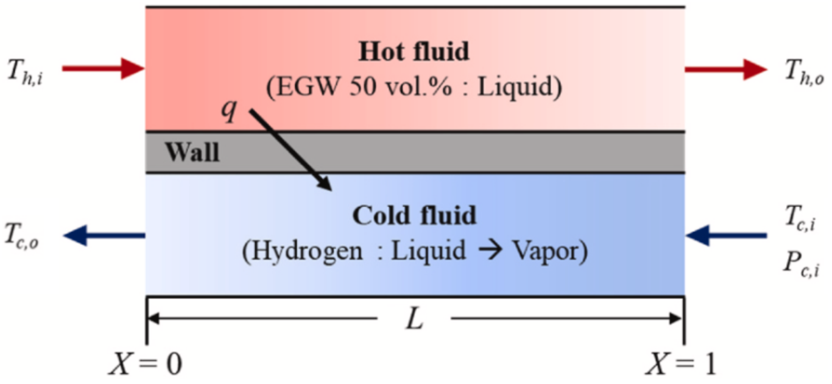

Figure 2.15: Vaporizer model schematic - ethylene glycol water mixture (EGW) and liquid hydrogen [45]

Effectiveness ϵ_{eff} is a measure of thermal performance of a heat exchanger. It is defined as a ratio of the actual heat transfer rate (Q) from the hot fluid to the cold fluid to the maximum heat transfer rate (Q_{max}) thermodynamically achievable as given by equation 2.29.

$$\epsilon_{eff} = \frac{Q}{Q_{max}} \approx f(NTU, \alpha_r) \tag{2.29}$$

$$\alpha_r = \frac{C_{min}}{C_{max}}, \quad NTU = \frac{UA_s}{C_{min}} \tag{2.30}$$

$$U = \frac{1}{R_{tot}}, \quad R_{tot} = \left(\frac{1}{h_h} + \frac{s_w}{k_w} + \frac{1}{h_c}\right) \tag{2.31}$$

where:

- A_s: heat transfer surface area
- α_r: heat capacity ratio
- h: heat transfer coefficients of cold and hot fluids (h_c, h_h)
- k_w: thermal conductivity of the wall
- R_{tot}: overall thermal resistance
- s_w: thickness of the wall
- NTU: overall number of heat transfer units for heat exchanger

In cryogenic heat exchangers the axial conduction effect becomes significant when there is a large temperature difference between the inlet and outlet. For this reason, it is important do design such vaporizer with $NTU > 90\,\%$ considering the axial conduction in the flow direction.

To calculate the heat transfer coefficient of EGW mixture in a rectangular channel, the following correlation for the fully developed Nusselt number is used [45]:

$$h_h = \frac{Nu_h k_h}{D_{h,h}} \tag{2.32}$$

$$Nu_h = 8.235 \left[1 - 2.0421\left(\frac{1}{AR_h}\right) + 3.0853\left(\frac{1}{AR_h}\right)^2 - 2.4765\left(\frac{1}{AR_h}\right)^3\right. \tag{2.33}$$

$$\left. +1.0578\left(\frac{1}{AR_h}\right)^4 - 0.1861\left(\frac{1}{AR_h}\right)^5\right] \tag{2.34}$$

where:

- AR: aspect ratio of flow channels
- D_h: hydraulic diameter
- Nu: Nusselt number

Unlike the single-phase flow of the EGW mixture, hydrogen in the low-pressure cryogenic vaporizer is supplied in liquid-phase and vaporized in gas-phase. Therefore, the phase change of hydrogen should be considered to calculate its heat transfer coefficient. For this purpose, the hydrogen pool boiling correlations of the tank model can be used.

Other studies present alternative geometries such as a shell and tube helical type heat exchanger for trains [46]. These provide useful insights into the fluid and thermal characteristics under various operating conditions but are not relevant designs for our type of application.

2.2. Research Directions and Questions

This section outlines the research directions derived from the background literature review and presents the resulting objectives established for this study.

2.2.1. Research Directions

With the relevant literature reviewed, the scope of this research can be defined. As noted in section 2.1.3, there is limited publicly available information on liquid hydrogen storage systems on vehicles equipped with fuel cell electric powertrains. Overall, the recent research directions that arose concerning the challenge of designing a liquid hydrogen storage system are summarized below.

- **Zero Boil-Off System:** relies on active cooling combined with passive insulation to completely remove hydrogen venting. NASA has developed these cryocooler-based systems for space applications, integrating multi-layer insulation with vapor-cooled shields.
- **Hydrogen Re-Liquefaction System:** instead of venting, boil-off gas can be re-liquefied, using cryogenic refrigeration cycles (e.g. reverse Brayton refrigeration cycle). Companies like Parker have been developing solutions to re-liquefy or utilize boil-off gas, thereby minimizing fuel loss and improving storage efficiency.
- **Compression and Utilization of Hydrogen Gas:** boil-off gas can be compressed and used in fuel cell vehicles, power generation, or refueling stations. Mechanical and non-mechanical compressors (e.g. electrochemical or ionic compressors) are being explored for efficient hydrogen compression. Recent developments aim to eliminate the need for pre-heating through cryogenic hydrogen compression. Car manufacturer Toyota has been developing a system that utilizes the pressure from boil-off gas to keep an optimal tank pressure, converting the vaporized hydrogen back into usable fuel without additional energy input.
- **Heat Recovery System:** study on heat exchanger than enables the vaporization and superheating of liquid hydrogen by recovering heat from turbine exhaust gases using a carrier fluid in a pipe-in-pipe design configuration.

Nearly all the studies mentioned above focus on the individual systems such as the storage tank and heat exchanger only. They do not consider the system as an entirety and do not evaluate the influence of a specific configuration on the whole powertrain. This work aims to address that gap by developing a model of the entire liquid hydrogen storage system line for a racing vehicle. A key feature of the proposed model will be its applicability to both hydrogen power unit types, fuel cell and internal combustion engine, providing greater flexibility and applicability.

Looking into the tank compartment itself, a model should be developed that is able to account for both static and dynamic conditions of the vehicle. This includes accounting for heat leakage as well as thermal stratification and sloshing effects by combining 1D system-level simulations with 3D CFD and particle-based analyses. Regarding the heat exchanger, the major novelty of this study resides in the development of such device for racing applications, in contrast to the aerospace focuses models commonly found in literature. Additionally, the integration of such device in the cooling system of the vehicle will be considered, with attention to radiator sizing.

On a broader scale, longitudinal dynamic, dormancy and boil-off simulations will be conducted to analyze range, power, fluid temperature and pressure on different driving cycles and boundary conditions. These will be carried out with the use of GT Suite, a 1D simulation platform for the analysis and optimization of the fuel cell systems and their components [47]. Additionally, 3D tools such as ANSYS Fluent and Particleworks will be used for the analysis of sloshing and thermal stratification effects.

2.2.2. Research Questions and Objectives

As the thesis is performed at an automotive company known as Dallara Automobili s.p.a., their racing vehicle Dallara Stradale [48] will be used as baseline. A basic CAD and 1D system simulation model developed in the pre-study are available for a gaseous hydrogen configuration. This serves as a benchmark for the study and to find an answer to the research questions.

The contribution of the thesis is therefore twofold. First, the liquid tank solution will be proposed and its performance will be evaluated through simulations. Second, the model will be integrated into the existing fuel cell electric vehicle to enable operation with this new technology. The objectives can be further boiled-down to the following research questions:

RQ1: Hydrogen Gas vs Liquid Technology Comparison
Which configuration (liquid or gaseous hydrogen storage) is more suitable for racing applications?

Verify the differences between a liquid and gaseous hydrogen fuel system on the vehicle. Specifically, the impact of these configurations on the vehicle's range, considering both the battery and hydrogen as limiting factors.

RQ2: Liquid Hydrogen Storage System Model Improvements
To what extent does a model improvement of the hydrogen heat transfer phenomenon affect the design of the tank?

Develop a thermal model model of the tank to simulate:

- Dormancy and Boil-Off
- Tank Design and Sensitivity
- Insulation Technologies
- Static and Dynamic Conditions
- Thermal Stratification
- Sloshing

What heat exchanger configuration is the most accurate for this type of application?

Develop a model that considers:

- Heat exchanger type
- Flow configuration
- Sizing
- Heat transfer and pressure drop

RQ3: System Design Alternatives
What effect would the use of a gaseous hydrogen compressor instead of the cryogenic liquid hydrogen pump have on the whole system?

The liquid hydrogen fuel cell powertrain layout is being defined by the regulatory bodies for racing applications. However, alternatives could be explored to find the optimal configuration.

3

Model Description

In a conventional liquid hydrogen storage system (LHSS), the fuel is extracted from the storage tank using a cryogenic pump. This device provides the necessary pressure increase before the liquid hydrogen is directed to the evaporator. There the fluid undergoes a phase transition and is subsequently delivered at the required temperature and in its gaseous state. Prior to entering the power unit, the fuel flows through a buffer tank, which serves to mitigate pressure fluctuations and to regulate the fuel supply to the downstream components. In this chapter, the setup of the full line model is described followed by a more detailed explanation of the tank and heat exchanger models.

3.1. Full Line Model

The model of the complete fuel supply line has been developed on the basis of the P&ID diagram of the LHSS plant provided by the company and presented in section 2.1.3. Figure 3.1 displays the different components that are modeled and addressed in this chapter.

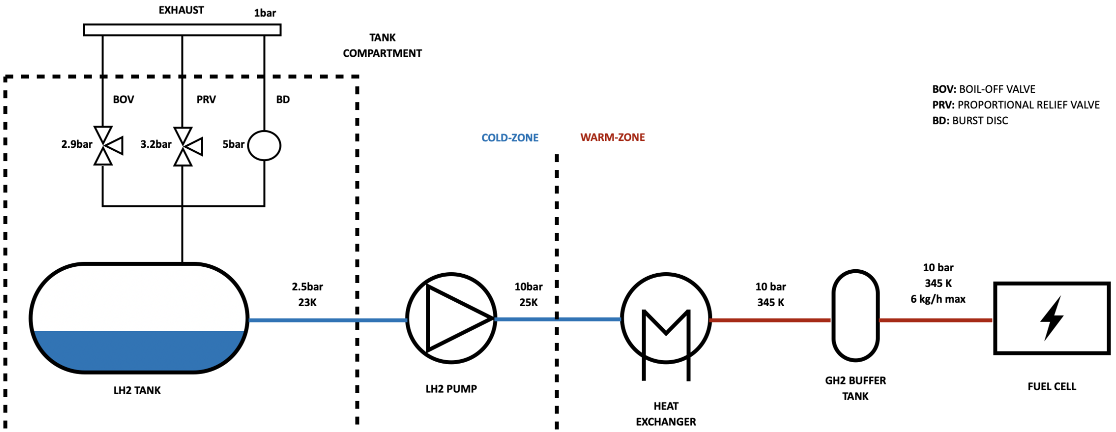

Figure 3.1: LHSS Plant Model Overview - Systems and Operating Conditions

The model has been implemented using GT Suite, a multi-physics simulation platform that allows to simulate the whole tank-to-wheel system in a computationally efficient 1D framework. In this environment, components are represented by simplified one-dimensional flow and energy models rather than full 3D geometries, which allows to evaluate system performance efficiently while still capturing the essential physics.

The simulations are carried out using the benchmark vehicle provided by Dallara, characterized by the parameters listed in table 3.1:

Parameter	Unit	Value
Vehicle		
Mass $m_{vehicle}$	kg	1400
Brake bias $\%bb$	–	55
Aerodynamic drag coefficient $C_x S$	–	1.068
Aerodynamic drag coefficient $C_z S$	–	2
Rear tire rolling radius r_r	mm	318.43
Front tire rolling radius r_f	mm	303
Environment		
Pressure p_{amb}	bar	1
Temperature T_{amb}	$°C$	15
Relative humidity χ_{amb}	$\%$	50
Density ρ_{amb}	kg/m^3	1.225
Powertrain		
Regenerative braking	–	On
Fuel cell max power $P_{FC,max}$	kW	82
Fuel cell control strategy P_{FC}	–	Var.

Table 3.1: Main simulation parameters concerning vehicle, environment and powertrain setup

The speed profile that is given as an input to the model corresponds to a complete lap of the Dallara Stradale vehicle on the Mugello race circuit, as illustrated in figure 3.2.

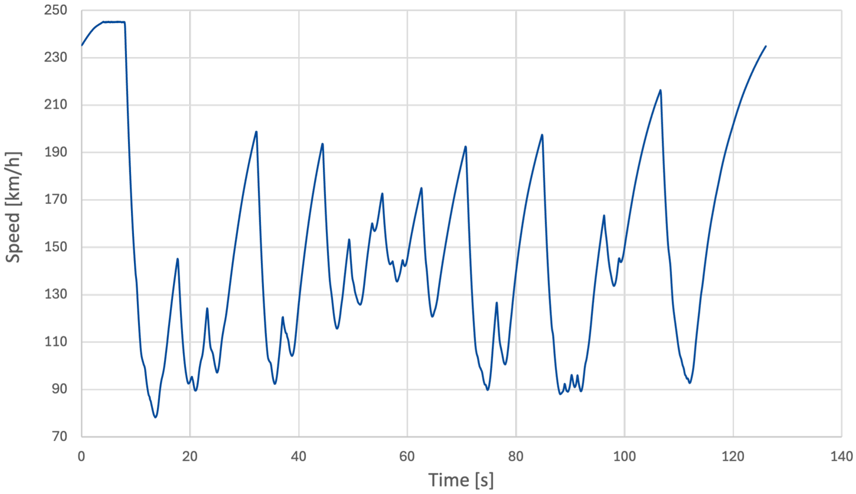

Figure 3.2: Speed Profile of Dallara Stradale vehicle at Mugello Circuit (provided by Dallara)

In the following paragraphs, the key aspects of the model development are described, including the setup procedure, simulation methodology, and the limitations of the adopted approach.

The flow model involves the solution of the Navier-Stokes equations, namely the conservation of continuity 3.1, momentum 3.2 and energy equations 3.3. These equations are solved in one dimension, which means that all quantities are averages across the flow direction. The time integration method chosen is the implicit integrator, where the mass flow, pressure and total enthalpy are the primary solution variables.

The whole system is discretised into many volumes, where each flowsplit is represented by a single volume, and every pipe is divided into one or more volumes. These volumes are connected by boundaries. The scalar variables (pressure, temperature, density, internal energy, enthalpy, species concentrations, etc.) are assumed to be uniform over each volume. The vector variables (mass flux, velocity, mass fraction fluxes, etc.) are calculated for each boundary. This type of discretization is referred to as staggered grid and displayed in figure 3.3.

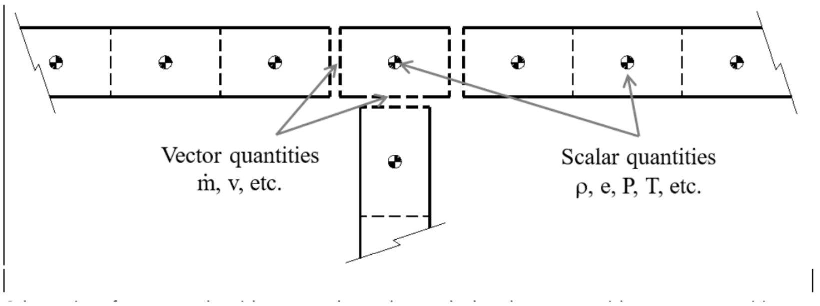

Figure 3.3: Schematic of staggered grid approach: scalars calculated at centroid, vector quantities at boundaries

The conservation equations solved by GT Suite are shown below. The left hand side represents the derivatives of the primary variables. The methods to calculate the secondary variables, such as pressure and temperature, are discussed below.

$$\text{continuity: } \frac{dm}{dt} = \sum_{boundaries} \dot{m} \tag{3.1}$$

$$\text{enthalpy: } \frac{d(\rho HV)}{dt} = \sum_{boundaries} (\dot{m}H) + V\frac{dp}{dt} - hA_s(T_{fluid} - T_{wall}) \tag{3.2}$$

$$\text{momentum: } \frac{d\dot{m}}{dt} = \frac{dpA + \sum_{boundaries}(\dot{m}v) - 4C_f \frac{\rho v|v|}{2} \frac{dxA}{D_{eq}} - K_p(\frac{1}{2}\rho v|v|)A}{dx} \tag{3.3}$$

where:

- $\dot{m}$: boundary mass flux into volume $\dot{m} = \rho A u$
- m: mass of the volume
- V: volume
- p: pressure
- A: cross-sectional flow area
- A_s: heat transfer surface area
- H: total specific enthalpy
- h: heat transfer coefficient
- T_{fluid}: fluid temperature
- T_{wall}: wall temperature
- v: velocity at the boundary
- C_f: Fanning friction factor
- K_p: pressure loss coefficient
- D_{eq}: equivalent diameter
- dx: length of mass element in the flow direction (discretization length)
- dp: pressure differential acting across dx

The implicit method solves the values of all sub-volumes at the new time simultaneously, by iteratively solving a non-linear system of algebraic equations. Because the implicit solution is iterative, it is important to verify that the solution for each step has numerically converged. The time step used in the implicit solver is chosen at $\Delta t = 0.001\,s$ and is not limited or determined by the Courant condition.

Similarly, GT Suite allows to solve equations in the electrical and chemical domain. Taking the fuel cell stack as an example, an object is defined to specify the electrochemical and mass transport properties of the PEMFC. This reference object uses physical characteristics of the fuel cell membrane electrode assembly to predict fuel cell performance based on various correlations, which are specified in section 2.1.1 and in the appendix A. This reference object is used to define the voltage, species transport, and heat generation that will be applied in the fuel cell.

An overview on the model implementation in GT Suite is provided in figure 3.4, where the entire fuel supply line from the tank to the fuel cell inlet are presented.

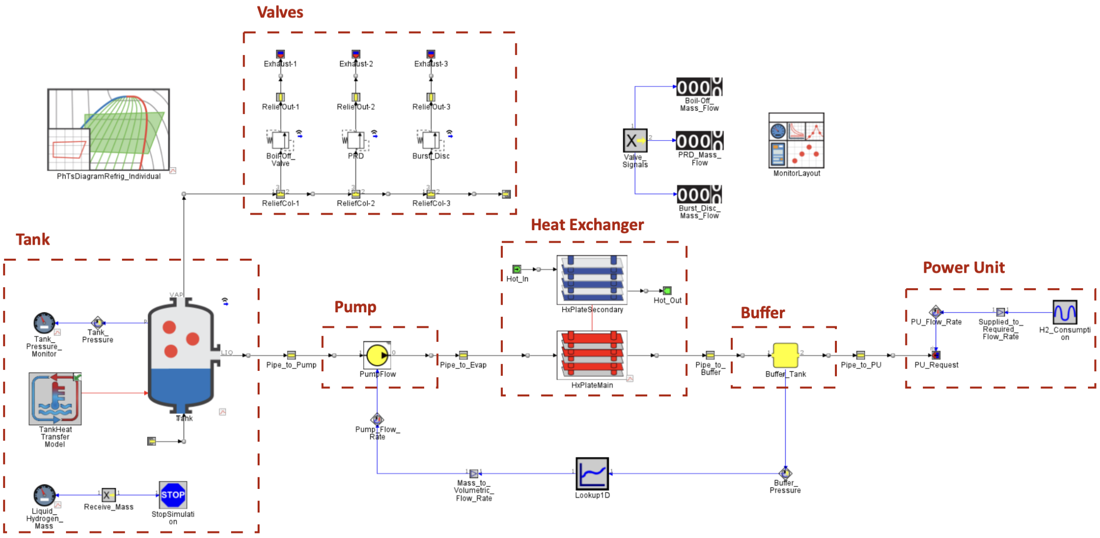

Figure 3.4: LHSS Plant Overview with GT Suite Interface

Tank Compartment

Starting with the tank compartment, the hydrogen fuel is modeled as a refrigerant fluid. This template is used for modeling the properties of a fluid expected to operate in the two phase state. The refrigerant properties will be calculated by a subroutine within the code that is written by the National Institute of Standards and Technology (NIST) in the REFPROP program. It is stored within the tank at an initial pressure of $p_{tank} = 2.5\, bar$ and quality of

$$qt = \frac{m_{H_{2,l}}}{m_{tot}} = \frac{\frac{\rho_{H_{2,l}}}{V_{H_{2,l}}}}{\frac{\rho_{H_{2,g}}}{V_{H_{2,g}}} + \frac{\rho_{H_{2,l}}}{V_{H_{2,l}}}} \tag{3.4}$$

where:

- $\rho_{H_{2,l}}, \rho_{H_{2,g}}$: densities of liquid and gaseous hydrogen at the given pressure
- $V_{H_{2,l}}, V_{H_{2,g}}$: volumes occupied by the two phases

with

$$V_{H_{2,l}} = 0.9 \cdot V_{tot} \tag{3.5}$$

indicating that the fluid is for 90% in liquid and 10% in gaseous phase.

The tank is modeled as a cylinder that acts as a phase separator with a volume $V_{tank} = 40\, l$ that is defined by the packaging constraints of the fuel cell electric vehicle model provided by the company. A cylinder height term is defined as $H_{tank} = 588\, mm$ to account for gravity effects. The pressure at the outlet of the tank will be effectively increased via a body force acceleration term that is calculated based on this height input. More, a heat flux is imposed at the tank wall through a thermal convection connection, which is an output of the tank thermal model that will be addressed in section 3.2.

The other sub-assembly of the tank compartment consists of the different valves, which are responsible for the purge of gaseous hydrogen that accumulates within the storage unit. For pressure driven valves, GT Suite uses a template to impose valve behavior in which the user provides the discharge coefficient as a function of pressure drop and a time constant to approximate the dynamics of the valve. These are indicated in figure 3.4 as Boil-Off valve, PRV and Burst Disc respectively, which follow the safety guidelines indicated by the FIA regulations.

The valve is characterized as a variable orifice, which will begin to open when the pressure drop across the valve becomes greater that the cracking pressure drop. The valve will then become fully open when the pressure drop across the valve becomes greater than the pressure drop to fully open valve. In case of the boil-off valve, these two values are set at $p = 2.8\,bar$ and $p = 3\,bar$ respectively, where the latter is also defined as the maximum exceedable operating pressure (MEOP). Regarding the burst disc, it serves as a mechanical safety device designed to rupture when a specific pressure threshold is reached, thereby allowing the rapid release of any remaining gaseous hydrogen from the tank.

The design parameters chosen to model the tank compartment are listed in table 3.2:

Parameter	Unit	Value
Tank		
Volume V_{tank}	L	40
Height H_{tank}	mm	588
Diameter D_{tank}	mm	294
Initial pressure p_{tank}	bar	2.5
Initial temperature T_{tank}	K	23.75
Quality qt	–	0.0051
Valves		
Diameter D_{valve}	mm	1.37
BOV cracking pressure p_{OP}	bar	2.8
BOV pressure at fully open valve p_{MEOP}	bar	3

Table 3.2: Tank compartment design parameters

Pipes and Flowsplits

Both liquid and gaseous hydrogen are transported within the system through pipes and flow splits, which are modeled with a round cross-section and adiabatic walls. Their diameter is set at $D_{pipe,l} = 30\,mm$ and $D_{pipe,g} = 10\,mm$ respectively.

The design parameters chosen to model the piping system are summarized in table 3.3:

Parameter	Unit	Value
Pipe		
Pipe diameter of liquid hydrogen line $D_{pipe,l}$	mm	30
Pipe diameter of gaseous hydrogen line $D_{pipe,g}$	mm	10

Table 3.3: Pipe design parameters

Flow losses in pipes due to friction along the walls are calculated automatically via a Fanning friction factor as a function of Reynolds number and the wall surface roughness. The fanning friction factor C_f is then used in the momentum equation 3.3. The Moody Diagram, which describes the relationship between the Reynolds number, wall roughness, and the resulting friction factor, is mathematically defined by an explicit Colebrook equation that assumed fully developed flow [49].

For what concerns pressure losses, these are represented by their respective pressure loss coefficient K_p as defined in equation 3.6:

$$K_p = \frac{p_{out} - p_{in}}{\frac{1}{2}\rho v_{in}^2} \tag{3.6}$$

where:

- p_{in}: total pressure at inlet
- p_{out}: total pressure at outlet
- ρ: inlet density
- v_{in}: inlet velocity

Pump and Buffer

It is critical that these liquid hydrogen pumps are hermetically sealed and leak only very small trace amounts of hydrogen to the outside environment. As liquid hydrogen temperatures are typically at cryogenic values, it is also critical that heat input is minimized [50]. Additionally, a major challenge in the design of such pumps relies in the fluid conditions at the inlet. Due to sloshing effects in the tank, there might be gaseous hydrogen that flows into the pump. This might lead to cavitation and pump damage, which drastically reduces its efficiency and performance. To solve this, a liquid hydrogen buffer can be placed at the bottom of the tank, which ensures a direct flow into the pump (see figure 2.10).

Pump performance data is typically measured on a flow bench and consists of a series of operating points, each of which is described by rotational speed, pressure rise (head), volumetric flow rate, and isentropic efficiency. This performance data is pre-processed and displayed in form of a performance map, which is provided by the supplier.

Due to the absence of available flow maps, it is modeled by imposing a variable volumetric flow rate and a total isentropic efficiency. Given that the pressure rise is known and equal to

$$\Delta p = p_{target} - p_{tank} = 7.5\,bar \tag{3.7}$$

the pressure head is computed as follows:

$$H_p = \frac{\Delta p}{\rho g} \tag{3.8}$$

where:

- H_p: pressure head
- Δp: pressure rise
- ρ: fluid density
- g: gravity

The efficiency impacts both the outlet fluid temperature and the resulting compression power applied to the pump shaft. The temperature of the fluid in the outlet volume downstream of the pump will be affected by the change in enthalpy across the pump. The outlet enthalpy and compression power are calculated as follows:

$$h_{out} = h_{in} + \Delta h_s \frac{1}{\eta_s} \tag{3.9}$$

$$P_{fluid,tot} = \frac{\dot{m}\Delta h_s}{\eta_s} \tag{3.10}$$

$$\Delta h_s = \frac{p_{out} - p_{in}}{\rho_{in}} \tag{3.11}$$

where:

- Δh_s: isentropic enthalpy change
- η_s: isentropic (total) efficiency
- $P_{fluid,tot}$: total fluid power
- $\dot{m}$: mass flow rate
- p_{out}: outlet static pressure
- p_{in}: inlet static pressure
- ρ_{in}: inlet density

Alternatively, the isentropic efficiency can be calculated knowing the total power consumed P_{tot} and the driveline efficiency η_d.

$$\eta_s = \frac{\dot{m}\Delta h_s}{P_{tot}\eta_d} \tag{3.12}$$

The volumetric flow rate of the pump is regulated by a feed-forward control strategy designed to maintain the buffer pressure at $p_{target} = 10\,bar$. The control input is determined through a one-dimensional lookup table that maps the target pressure to the corresponding mass flow rate as shown in figure 3.5.

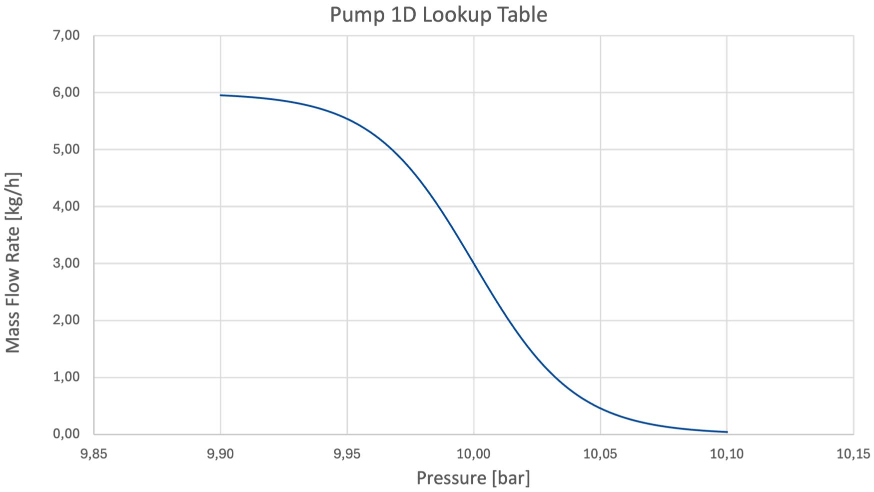

Figure 3.5: Pump Look Up Table

This value is subsequently converted into the appropriate commands signal for the pump. The implemented control logic ensures that the buffer tank pressure remains at the desired level, thereby reducing oscillations induced by the variable fuel flow demand of the power unit. For this purpose, the buffer tank volume is set at $V = 4\,l$, which ensures that the minimum pressure requirement can be sustained under the fuel flow rates demanded by the system.

The design parameters chosen to model the pump and buffer system are summarized in table 3.4:

Parameter	Unit	Value
Pump		
Maximum mass flow rate $\dot{m}_{max}$	kg/h	6
Isentropic efficiency η_{is}	$-$	1
Buffer		
Buffer volume V_{buffer}	l	4

Table 3.4: Pump and buffer parameter list

Heat Exchanger

More, the heat transfer inside the evaporator is modeled between the fluid and wall of a plate heat exchanger. This is made up of flow volumes and thermal mass components and can be internally discretised into smaller segments. The discretised model will see the plate channels connected in series, with tanks separating each pass, or in parallel depending on the flow configuration created. Each segment can be connected to a discretised wall that interacts thermally with one volume on either fluid side. Heat exchanger discretization is necessary to ensure that a thermal fluid-wall distribution is captured to model the two-phase heat exchanger. The method of heat exchanger discretization used can be seen in figure 3.6.

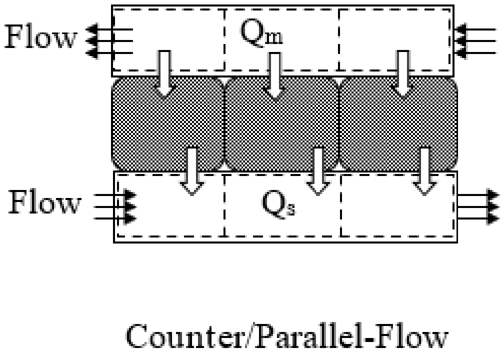

Figure 3.6: Heat exchanger discretization scheme

The heat exchanger is represented as a counter-flow, single pass configuration, with hydrogen defined as the two-phase cold fluid and water as hot fluid. The calculation includes the effects of the wall thermal capacitance, and the conductivity of the material (if modeled). The temperature of the structure in a heat exchanger is calculated from a balance of the heat transfer rates between the structure and the two fluids using the following equation:

$$\frac{dT_{wall}}{dt} = \frac{Q_m + Q_s}{\rho V c_p} = \frac{\left[\left(\frac{hA_{base}+\eta_{fin}hA_{fin}}{1+hR_f}\right)\Delta T - \frac{2kA_c\Delta T_w}{s_t}\right]_m + \left[\left(\frac{hA_{base}+\eta_{fin}hA_{fin}}{1+hR_f}\right)\Delta T - \frac{2kA_c\Delta T_w}{s_t}\right]_s}{\rho V c_p} \tag{3.13}$$

where:

- A_{base}: base heat transfer area (not including fins)
- A_c: thermal cross-sectional conduction area
- A_{fin}: fin heat transfer area
- c_p: heat capacity of the wall material
- h: fluid heat transfer coefficient
- k: thermal conductivity of the wall material
- η_{fin}: fin efficiency
- ρ: density of the wall material
- R_f: fouling resistance
- s_t: tube thickness
- ΔT: effective temperature difference between the fluid and the wall
- ΔT_w: temperature difference between the surface and average wall temperature
- V: volume of the wall material

The heat transfer rate from each fluid sub volume to the wall is calculated using the heat transfer coefficients defined by an empirical correlations. Similarly, the pressure loss of the heat exchanger is described with empirical friction models and discharge coefficients instead of lumped pressure loss components. These offer an advantage over lumped pressure loss setups by being able to capture the pressure distribution that occurs within the heat exchanger core, thus capturing the phase change of the hydrogen refrigerant. These correlations as well as a more detailed model description of the heat exchanger will be addressed in section 3.3.

The main design parameters chosen to model the heat exchanger are summarized in table 3.5:

Parameter	Unit	Value
Heat Exchanger		
Coolant inlet temperature $T_{EGW,in}$	K	346
Coolant pressure p_{EGW}	bar	1
Coolant maximum mass flow rate $\dot{m}_{EGW}$	kg/s	2.5
Hydrogen inlet temperature $T_{H_2,in}$	K	25
Hydrogen outlet temperature $T_{H_2,out}$	K	346
Hydrogen pressure p_{H_2}	bar	10
Hydrogen maximum mass flow rate $\dot{m}_{H_2}$	kg/s	0.0017

Table 3.5: Heat exchanger model parameter list

Power Unit Integration

To complete the model, the LHSS plant is coupled with the fuel supply line of the FCEV provided by the company. As the original configuration was designed for gaseous hydrogen, modifications to the model setup were required. Figure 3.7 shows the LHSS subsystem represented as a single block, integrated into the anode side of the balance of plant.

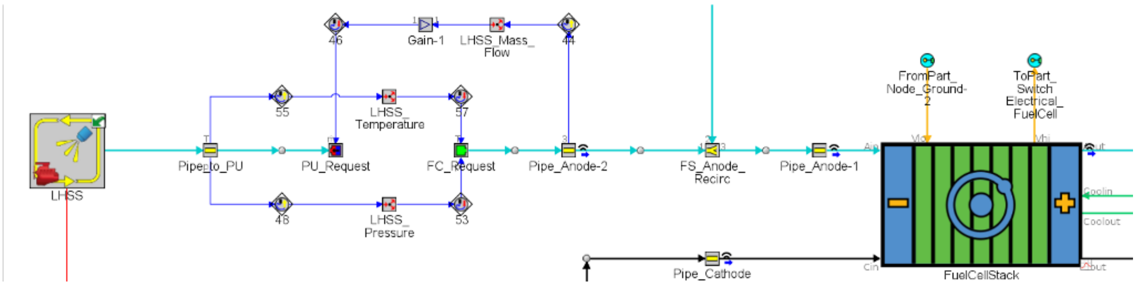

Figure 3.7: LHSS integration into FCEV Model - GT Suite Interface

As illustrated, the two systems are not directly connected but instead operate through to distinct circuits. This is a consequence of the modeling framework: the LHSS sub-assembly employs a refrigerant template to represent hydrogen, whereas the fuel cell circuit is restricted to a gaseous hydrogen template. This tool-related limitation was addressed by enforcing continuity conditions for pressure, temperature, and mass flow rate at the interface between the two circuits, thereby enabling them to operate seamlessly as a single integrate system. Through this approach, the LHSS was successfully implemented as the fuel supply fo the FCEV, allowing the vehicle model to operate on liquid hydrogen.

3.2. Tank Model

Modeling the behavior inside a liquid hydrogen tank is necessary for designing high performance tanks that can meet the dormancy and pressure control requirements. This allows for proper sizing and material selection to meet the desired targets. Different aspects will be considered during the development of the tank model:

- heat leakage
- separate phase characterization
- dynamic effects

These will be evaluated based on dormancy and boil-off effects, which mainly characterize the tank behavior.

The study of the boiling dynamics of the liquid hydrogen can be analyzed by modeling the analyzing the link between dormancy time, boil-off flow, and state of charge. The boil-off time of liquid hydrogen depends on the heat flow in the tank, that in turn affects the variation of the internal pressure (figure 3.8). This results in the container being a pressure tank and needing a pressure monitoring and control system.

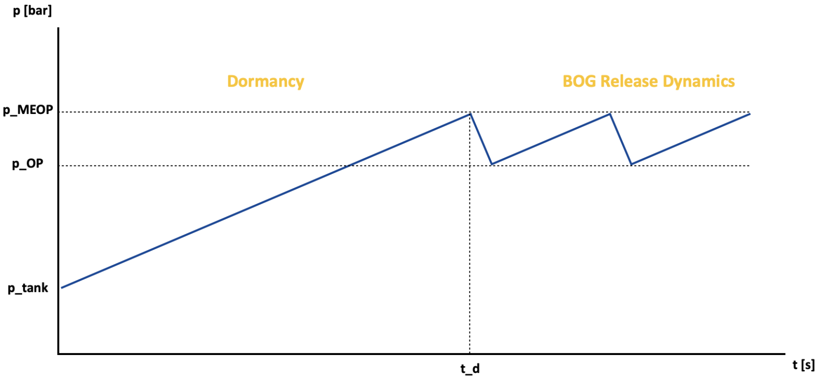

Figure 3.8: Tank states for boil-off dynamics study (provided by Dallara)

Two different phases/states of tank are being analyzed:

- **Dormancy:** the tank pressure evolution before the first valve opening (dormancy time). This behavior occurs when the tank, hence the vehicle, are in static conditions (e.g. before a race). For this reason, the thermal equilibrium assumption between the two phases is not valid anymore. Different studies [38], [41] have demonstrated that the temperature gradient between the phases does induce a relevant heat transfer. The simulation software GT Suite does not allow to model different heat fluxes of the two phases with a cryogenic fluid. Another tool that can be employed for this purpose is the software package BoilFAST [51] or CFD 3D simulations with ANSYS Fluent.
- **BOG release dynamics:** what happens after the first valve opening (calculating the released gaseous hydrogen quantity and valve opening frequency). In dynamic conditions, the two fluids are mixing with each other, hence the thermal equilibrium assumption can be considered valid. Additionally, sloshing plays a major role when the tank is moving. This effect can be analyzed through particle based simulations using Particleworks.

The tank consists of two different volumes, filled with liquid and gaseous (evaporated) hydrogen respectively. Additionally, an aperture on the tank roof is modeled to consider hydrogen venting due to boil-off.

An overview of the implemented heat flux scheme is provided in figure 3.9:

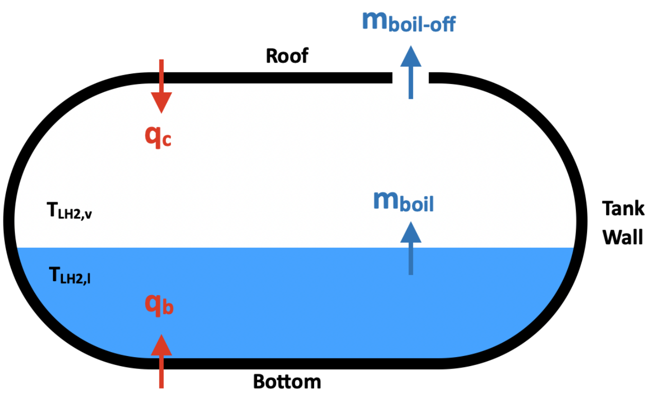

Figure 3.9: Hydrogen tank volume for heat transfer scheme

Additionally, the following model simplifications are made for implementation:

- temperature zones: only one temperature for both phases/zones, such that $T_{LH_2,v} = T_{LH_2,l}$ (well mixed) and the heat flux q_{vl} neglected
- boiling (liquid phase): just one boiling correlation model for bottom and wall
- free convection in liquid saturated phase: just one free convection correlation in saturated liquid phase for bottom and wall, also used for negative heat flux ($\Delta T < 0$ e.g. at tank filling)
- free convection in liquid subcooled phase: no correlation implemented for subcooled liquid area (modeling heat flux for subcooled liquid hydrogen not valid)
- free convection in vapor and superheated vapor phase: just one free convection correlation in vapor phase for bottom and wall
- forced convection: one forced convection correlation for both phases considered
- condensation: no correlation implemented for any condensation

Understanding the heat transfer characteristics of hydrogen pool boiling is of significance to the modeling of a tank. This study by Wang [52] provides reliable correlations to guide the boiling heat transfer analysis, which is illustrated in figure 3.10.

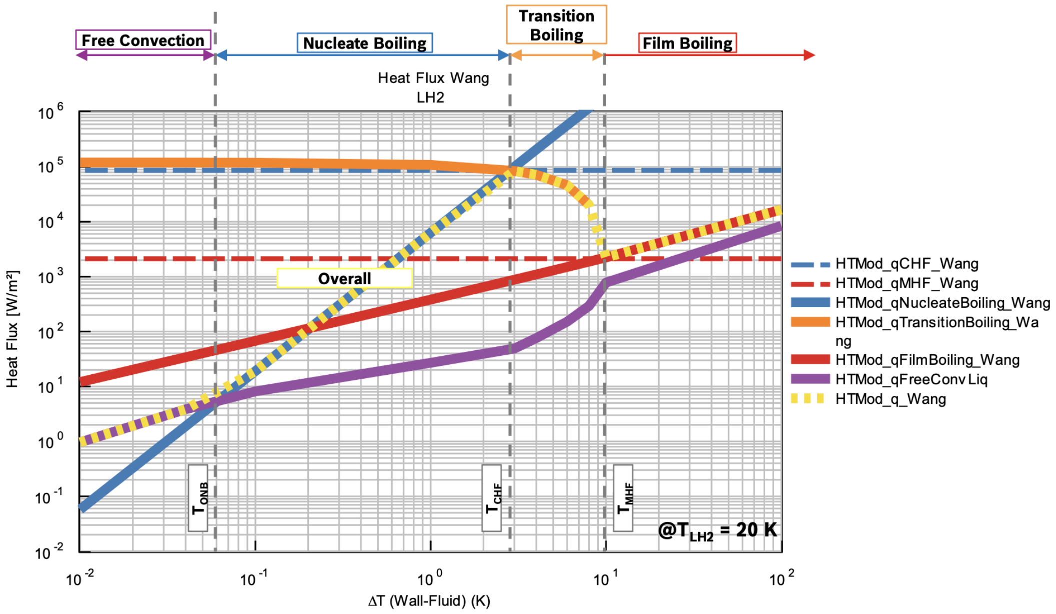

Figure 3.10: Heat flux with respect to the wall-fluid temperature difference during cool boiling (Wang [52])

Dependent on the temperature difference between the wall and liquid phase (ΔT), different states of boiling occur [52]:

- **Free Convection:** this occurs at very low heat fluxes where heat is transferred primarily through natural convection currents in the liquid hydrogen. There is no significant bubble formation, and heat transfer is dominated by conduction and convection within the liquid phase.

  $$q = C_t \frac{k_t}{L_x} (GrPr)^{n_t} \cdot \Delta T \tag{3.14}$$

  where:

  - C_t, n_t: coefficients dependent on heater type and flow regime
  - Gr: Grashof number $Gr = \frac{g\beta \Delta T L_x^3}{\nu^2}$
  - Pr: Prandtl number $Pr = \frac{\mu c_p}{\lambda}$
  - L_x: characteristic length
  - β: volume expansion ratio
  - k_t: thermal conductivity
  - ν: kinematic coefficient of viscosity
  - μ: dynamic coefficient of viscosity
  - q: heat flux
- **Nucleate Boiling:** as the heat flux increases, small bubbles start forming at nucleation sites on the heated surface (starting at T_{ONB}). These bubbles detach and rise through the liquid, enhancing heat transfer through latent heat absorption. Nucleate boiling is highly efficient as the phase change process removes significant amounts of heat.

  $$q = a \cdot \Delta T^b \tag{3.15}$$

  where:

  - a, b: $a = 6309$, $b = 2.52$ independent with pressure
- **Transition Boiling:** at higher heat fluxes, the boiling regime shifts between nucleate boiling and film boiling. The heat transfer mechanism becomes unstable, as localized vapor patches intermittently form and collapse on the heated surface. This results in fluctuating heat transfer rates and is generally considered an unstable boiling regime, located between the critical T_{CHF} and minimum T_{MHF} heat fluxes.

  $$q = q_{CHF} - \frac{\Delta T - \Delta T_{CHF}}{\Delta T_L - \Delta T_{CHF}} (q_{CHF} - q_L) \tag{3.16}$$

- **Film Boiling:** at very high heat fluxes, a continuous vapor layer forms between the heated surface and the liquid hydrogen. This vapor layer acts as an insulating barrier, significantly reducing heat transfer efficiency. Heat is primarily transferred through radiation and conduction across the vapor layer, leading to higher surface temperatures.

  $$q = \frac{0.37 + 0.28\frac{l_x}{D}}{\left(\frac{l_x \cdot \mu_v \Delta T}{\lambda_v^3 \rho_v (\rho_l - \rho_v) g h'_\lambda}\right)^{1/4}} \Delta T \tag{3.17}$$

  $$h'_\lambda = (h_\lambda + 0.34 c_{pl} \Delta T)^2 / h_\lambda \tag{3.18}$$

  where:

- h_λ: latent heat of vaporization
- h'_λ: effective latent heat of vaporization

More, the study by Darr and Hartwig [53] provides a two-phase convection heat transfer correlation for liquid hydrogen. This correlation set is fit to experimental data by using a lumped-node heat transfer model and allows us to account for forced convection effects within the tank.

- **Forced Convection:** occurs under dynamic conditions, where liquid hydrogen flows on the wall under the influence of an external force acting on the tank. The info on velocity field is derived from sloshing simulations performed through the Particleworks tool, where an average particle velocity was derived.

$$q = h \cdot (T_w - T_{sat}) \tag{3.19}$$

$$h = 61.6 Re^{-0.332} \cdot Ja^{-0.254} \cdot h^* \tag{3.20}$$

$$h^* = 0.023 Re^{0.8} Pr^{0.4} \cdot \left(\frac{k}{D}\right) \tag{3.21}$$

where:

- Ja: Jakob number $Ja = \frac{c_p(T_w - T_{sat})}{h_\lambda}$
- T_w: wall temperature
- T_{sat}: saturation temperature
- Re: Reynolds number $Re = \frac{\rho v D}{\mu}$
- v: average particle velocity
- Pr: Prandtl number $Pr = \frac{c_p \mu}{k}$
- k: thermal conductivity
- D: inner diameter

These empirical correlations provide an estimate for the heat transfer coefficient between the tank wall and hydrogen mixture in both static and dynamic conditions. This is modeled as a thermal resistance, which is identified in figure 3.11 as fluid convection connection.

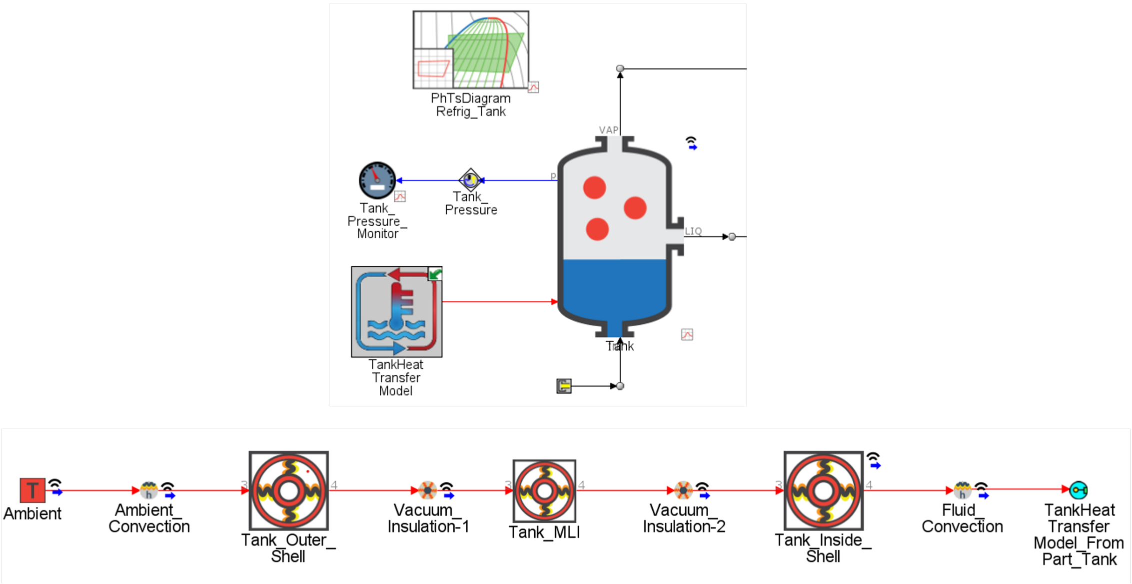

Figure 3.11: Tank Thermal Model Overview in GT Suite

The tank model illustrated above is characterized by a flow inlet, which is closed off as no filling simulations are considered in this analysis. The two flow outlets are respectively for the liquid and gaseous hydrogen. A pressure monitor is implemented to verify the correct operation of the model, ensuring that the valves regulate the internal tank pressure as intended.

The parameter used to evaluate the fuel consumption in the tank for comparison withe the gaseous hydrogen FCEV configuration is the equivalent consumption $C_{H_2,eq}$, defined as:

$$C_{H_2,eq} = \left(\frac{m_{H_2,cons}}{m_{H_2,tot}} \right) \cdot 100 \tag{3.22}$$

This parameter represents the percentage of hydrogen consumed $m_{H_2,cons}$ in the tank with respect to the initial total mass $m_{H_2,tot}$. The total mass accounts for both the fuel that has been extracted by the pump in liquid phase and the one that evaporated in gaseous phase.

As shown above, the tank model is composed of two concentric shells: an outer shell constructed from carbon fiber and an inner shell made of aluminum. Their respective thicknesses are $s_{in} = 2mm$ and $s_{out} = 6mm$, and the associated emissivity values are derived from experimental data on these materials provided by the company. Between these two shells, a cryogenic insulation system known as multi-layer insulation (MLI) is implemented. This technology minimizes heat transfer from the external environment to the stored cryogen and is widely recognized as one of the most effective insulation strategies for cryogenic applications [54]. The number of insulation layers is selected according to the desired effective thermal conductivity, which is in turn dependent on the vacuum quality.

The design parameters chosen to set up the thermal model of the tank are summarized in table 3.6:

Parameter	Unit	Value
Tank inner wall thickness $s_{w,i}$	mm	2
Tank outer wall thickness $s_{w,o}$	mm	6
Vacuum Gap s_v	mm	0.02
MLI count n_{layers}	–	1
Tank inner wall temperature $T_{w,i}$	K	23.75
Tank outer wall temperature $T_{w,o}$	K	340
Vehicle ambient temperature $T_{vehicle}$	K	340
Ambient convection heat transfer coefficient h_{amb}	W/m^2K	10
Emissivity aluminum ϵ_{al}	–	0.05
Emissivity carbon ϵ_c	–	0.9

Table 3.6: Tank thermal model simulation setup parameter list

Figure 3.11 illustrates a benchmark configuration in which a single aluminum layer of thickness $s_v = 0.02mm$ is placed inside the vacuum region. In this configuration, the dominant modes of heat transfer are:

- **Convection:** natural or forced convection occurs between the inner wall of the tank and the fuel, as well as between the external surface of the outer shell and the surrounding environment. The heat transfer resistance is calculated from Newton's Law of Cooling 3.23, where

$$R_{conv} = \frac{1}{h_{conv}} = \frac{(T_1 - T_2)}{Q} \tag{3.23}$$

- **Radiation:** within the vacuum layer, radiation constitutes the primary heat transfer mechanism. In this region, convection is absent and conduction is negligible due to the lack of a medium. Each reflective layer of the MLI contributes to increasing the overall thermal resistance by partially reflecting incident radiation. The heat transfer resistance is derived from equation 3.24:

$$R_{rad} = \frac{1}{h_{rad}A} \approx \frac{\Delta T}{\sigma \epsilon F_{12} A (T_1^4 - T_2^4)} \tag{3.24}$$

where:

- σ: Boltzmann constant
- ϵ: surface emissivity
- F_{12}: surface view factor

These mechanisms are represented in the model through a network of thermal resistances in series, which collectively restrict heat flux from the vehicle environment to the stored hydrogen. This formulation plays a critical role in determining boil-off losses and dormancy characteristics of the storage system.

In order to account for sloshing effects, simulations were carried out using the 3D tool Particleworks. These simulations provide valuable insights into two key aspects:

- **Pump Draft:** under conditions of fuel sloshing combined with a low filling level, the pump may begin to draw gaseous hydrogen from the tank, potentially inducing cavitation and leading to pump damage.
- **Increased Heat Leakage:** the simulation outputs include the velocity field of the particles within the tank, which enables the evaluation of forced convection effects according to equation 3.19.

The tank is modeled in two different configurations, with one of them including baffles designed to mitigate sloshing. These two are modeled using CREO Parametric Design and shown in figure 3.12.

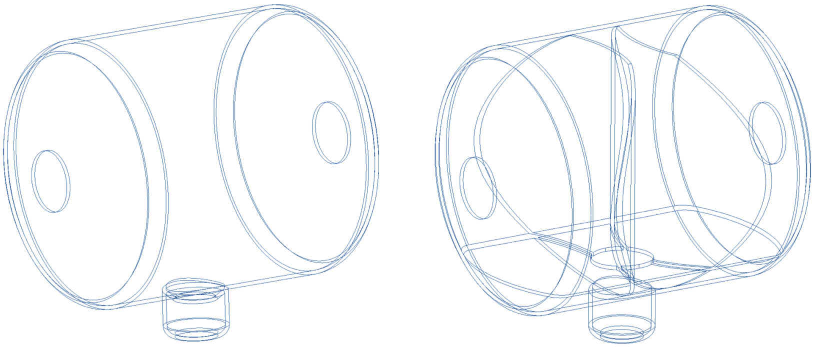

Figure 3.12: Tank 3D model plain geometry (left) and with baffles (right) for 3D simulation

To simulate dynamic conditions, the acceleration profile shown in figure 3.13 of the benchmark vehicle provided by Dallara at the reference driving cycle of the Mugello race circuit is used.

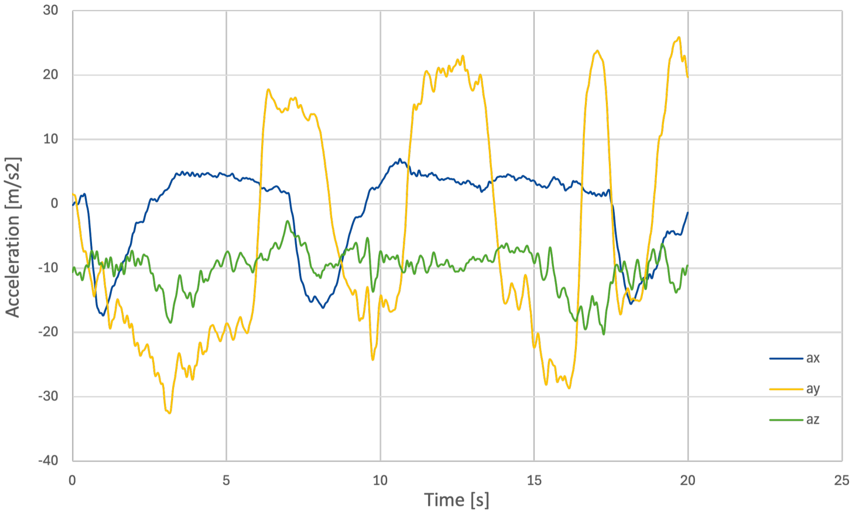

Figure 3.13: Vehicle Acceleration Profile in x,y,z of a sector of the Mugello race track

The model outputs include both visual animations, which facilitate the qualitative assessment of pump draft under the two tank configurations, and probe data used to quantify particle density at the tank outlet and velocity distributions along the inner wall. The simulations were conducted with a filling level of $l_h = 10\,\%$ and particle size of $D_p = 1\,mm$.

Furthermore, the 1D model described above treats hydrogen as a uniform two-phase mixture. This implies that the liquid and gaseous phases are at the same temperature and, consequently, that no heat transfer occurs between them. This represents a strong simplification, the validity of which depends on whether the system is analyzed under static or dynamic operating conditions. To assess the accuracy of this assumption, the 3D model of the plain tank in figure 3.12 was employed to run CFD simulations in ANSYS Fluent.

In this framework, the liquid and vapor phases are modeled as distinct media with independent temperature and pressure distributions, resolved using an unsteady, second-order bounded implicit scheme. Since this is a multiphase flow study, the volume of fluid VOF model is used by solving a single set of momentum equations and tracking the volume fraction bounded variable of each of the fluids throughout the domain. More, a viscous scale-adaptive simulation SAS is used to resolve the turbulence spectrum [55]. A constant heat flux is imposed at the tank wall, derived from the 1D GT Suite model in combination with the specified filling level. Phase change phenomena are captured using the Lee evaporation-condensation model [56], which has been experimentally validated in [57].

The setup of the two-phase model is defined according to the following parameters in table 3.7, which is used as simulation setup for both the 3D tools:

Parameter	Unit	Liquid Hydrogen	Gaseous Hydrogen
Density ρ	kg/m^3	66.5	3.06
Specific Heat c_p	J/kgK	12195	14149
Thermal Conductivity k	W/mK	0.10309	0.022385
Viscosity μ	kg/ms	$10.288e-06$	$1.2009e-06$
Molecular Weight M_{H_2}	$kg/kmol$	2.01594	2.01594
Reference Temperature T_{ref}	K	23.86	23.86
Enthalpy Δh_λ	$J/kgmol$	$2.097e+08$	0

Table 3.7: 3D CFD Simulation setup on ANSYS Fluent for liquid and gaseous hydrogen

3.3. Heat Exchanger Model

The setup of the heat exchanger model presented a significant challenge, primarily due to the lack of experimental data available for validation. To address this limitation, the device was designed on the basis of the specified boundary conditions and the volume constraints related to this type of application. In the design process, two principal aspects were considered:

- **Channel Freezing:** since liquid hydrogen operates at cryogenic temperatures, the coolant is at risk of freezing when in direct contact with the hydrogen side. From a simulation perspective, this includes accounting for temperature-dependent properties and possible flow non-uniform distribution, since even localized freezing can block channels and drastically reduce performance.
- **Phase Change:** capturing phase change of hydrogen is complex because it involves a two-phase flow with strong variations in density, heat transfer coefficients, and pressure drop. Accurate modeling requires correlations for boiling heat transfer and two-phase pressure drop that are valid at cryogenic conditions, where standard correlations may not apply.

As mentioned in 3.1, based on the given requirements a plate heat exchanger was chosen and represented in figure 3.14.

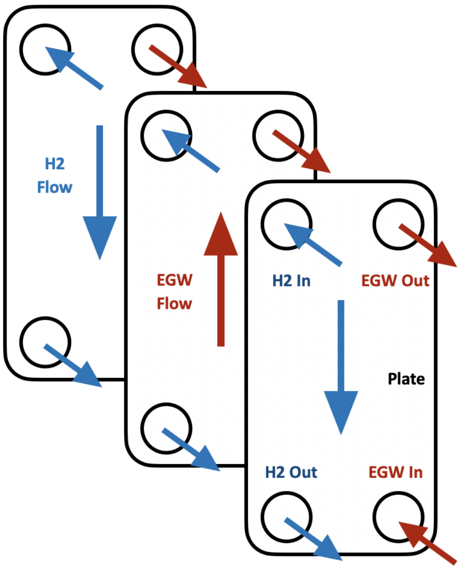

Figure 3.14: Plate Heat Exchanger Model Schematic

A plate heat exchanger (PHE) consists of a stack of thin, corrugated plates arranged so that the two fluids flow in alternating channels, separated by the plates. In this case, the main side consists of liquid hydrogen flowing through one set of channels as it absorbs heat, undergoing phase change. In the secondary side, water flows through the adjacent channels in counter-flow configuration, giving up heat to the hydrogen. The large surface-to-volume ratio of the corrugated plates enhances heat transfer, while the thin plate walls allow for efficient conduction of heat between the fluids.

This model has been implemented in GT Suite as illustrated in figure 3.15.

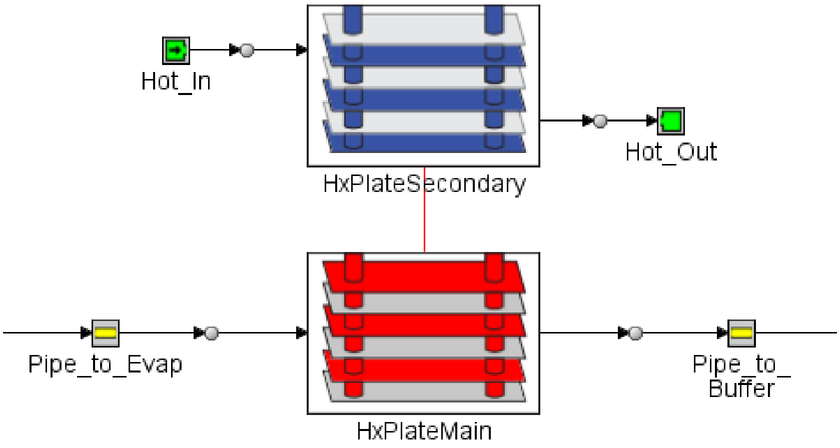

Figure 3.15: Plate Heat Exchanger Model Overview in GT Suite

This *HxPlateMain* template is used to model heat transfer between the fluid and wall of a plate heat exchanger. The fluid boundary conditions on the opposite surface of the heat exchanger mass are obtained from a connected *HxPlateSecondary* component. The initial state defined for the main, hydrogen side is:

- Inlet Pressure $p_{H_2} = 10\, bar$
- Inlet Temperature $T_{H_2,in} = 25\, K$
- Wall Temperature $T_{wall} = 340\, K$

while for the secondary side the same conditions of the fuel cell cycle coolant are chosen:

- Inlet Pressure $p_{EGW} = 1\, bar$
- Inlet Temperature $T_{EGW,in} = 346\, K$

The coolant used is an ethylene-glycol water EGW mixture with a 97:3 ratio, which provides adequate freezing protection and is commonly employed in automotive applications [45].

The following sections present an analysis of the heat exchanger model with respect to its geometry, heat transfer performance, and pressure drop characteristics.

Table 3.8 goes over the main geometric parameters of the component:

Geometry	Unit	Value
Overview		
Plate length L	mm	200
Plate width W	mm	120
Plate wall thickness s	mm	0.5
Main inlet connection diameter $D_{m,1}$	mm	30
Main outlet connection diameter $D_{m,2}$	mm	30
Secondary inlet connection diameter $D_{s,1}$	mm	30
Secondary outlet connection diameter $D_{s,2}$	mm	30
Main Channel		
Channel height h_{chan}	mm	2
Secondary Channel		
Channel Height h_{chan}	mm	2
Layout		
Number of channels on main side $n_{ch,m}$	–	20
Number of channels on secondary side $n_{ch,s}$	–	20

Table 3.8: Main geometric parameter list of heat exchanger model

The overall heat transfer coefficient U and consequently the total thermal resistance R are expressed as

$$\frac{1}{UA_s} = \frac{1}{UA_i} = \frac{1}{UA_o} = R = \frac{1}{h_iA_i} + R_{wall} + \frac{1}{h_oA_o} \tag{3.25}$$

$$= \frac{1}{h_iA_i} + \frac{R_{fi}}{A_i} + \frac{ln\left(\frac{D_o}{D_i}\right)}{2\pi kL} + \frac{R_{fo}}{A_o} + \frac{1}{h_oA_o} \tag{3.26}$$

while the rate of heat transfer for the cold and hot fluid respectively

$$Q = \dot{m}_c c_{p,c}(T_{c,o} - T_{c,i}) \tag{3.27}$$

$$Q = \dot{m}_h c_{p,h}(T_{h,i} - T_{h,o}) \tag{3.28}$$

As the outlet temperatures are known, the LMTD-method is used to compute the heat transfer rate as

$$Q = UA_s\Delta T_{lm} \tag{3.29}$$

$$\Delta T_{lm} = \frac{\Delta T_1 - \Delta T_2}{ln\left(\frac{\Delta T_1}{\Delta T_2}\right)} \tag{3.30}$$

As mentioned in section 3.1, the heat transfer rate from each fluid sub-volume to the wall is calculated using heat transfer coefficients defined by empirical correlations.

To describe the heating of the single phase turbulent flow on both the main and secondary side, the Dittus-Boelter correlation 3.31 is used:

$$Nu = 0.023 \cdot Re^{0.8}Pr^{0.4} \tag{3.31}$$

where

$$Nu = \left(\frac{hL}{k}\right) \tag{3.32}$$

with

- L: reference length
- k: thermal conductivity of the fluid
- Nu: Nusselt number

This correlation is valid for fully developed flow only, namely when

$$\frac{L}{D} \geq 10; \quad 0.6 \leq Pr \leq 160; \quad Re \geq 10000.$$

The two phase correlation used to describe the phase change process is the one of Kandlikar for plate-style evaporators 3.33:

$$h = \left(2.312 \cdot Co^{-0.3} \cdot E_{CB} + 667.3 \cdot Bo^{0.7} \cdot F_{fl} \cdot E_{NB}\right)\left(1 - qt\right)^{0.003} \cdot h_{lo} \tag{3.33}$$

with

$$E_{CB} = 0.512, \quad E_{NB} = 0.338 \quad \text{and} \quad F_{fl} = 1$$

and

- h_{lo}: heat transfer coefficient as calculated by Dittus-Boelter in equation 3.31.
- Co: convection number $Co = \left(\frac{1-qt}{qt}\right)^{0.8}\left(\frac{\rho_g}{\rho_l}\right)^{0.5}$
- Bo: boiling number $Bo = \frac{q}{m''(h_g-h_l)}$
- qt: quality
- q: heat flux
- m'': mass flux
- h_g: gas phase enthalpy
- h_l: liquid phase enthalpy

Similarly, the friction loss model used for the single phase fluid state is the one for pipe flow, where the Fanning friction factor is computer from the following formulation:

$$f = \begin{cases} \frac{16}{Re} & Re_D < Re_{cr} \\ \frac{1}{4}\left(4.781 - \frac{(A-4.781)^2}{B-2A+4.781}\right) & Re_D > 4000 \end{cases} \tag{3.34}$$

where

$$A = -2.0log_{10}\left(\frac{\epsilon/D_h}{3.7} + \frac{12}{Re_D}\right)$$

$$B = -2.0log_{10}\left(\frac{\epsilon/D_h}{3.7} + \frac{2.51A}{Re_D}\right)$$

For the two phase fluid state, the Friedel correlation applies a multiplier Φ^2 to the Pipe Flow approach to adjust for increased energy and momentum transfer. The equations for this correlation are described below:

$$\Phi^2 = E + \frac{3.24 \cdot F \cdot H}{Fr_h^{0.045} We^{0.035}} \tag{3.35}$$

where

$$E = (1-x)^2 + x^2 \frac{\rho_l f_g}{\rho_g f_l}$$

$$F = x^{0.78}(1-x)^{0.224}$$

$$H = \left(\frac{\rho_l}{\rho_g}\right)^{0.91}\left(\frac{\mu_g}{\mu_l}\right)^{0.19}\left(1 - \frac{\mu_g}{\mu_l}\right)^{0.7}$$

with

- Fr: Froude number $Fr = \frac{m''^2}{\rho D \rho^2}$
- We: Weber number $We = \frac{m''^2 D}{\sigma\rho}$

3.4. Layout Alternative Model

As outlined in section 2.2, one of the objectives of this study is to evaluate potential design alternatives for the LHSS plant. One of those includes the use of a compressor stage that provides the required pressure rise, thus replacing the cryogenic pump. The latter is set to work with liquid hydrogen at cryogenic temperatures, which as stated in 3.1 can affects its reliability. Figure 3.16 illustrated the modified P&ID diagram that corresponding to this alternative design.

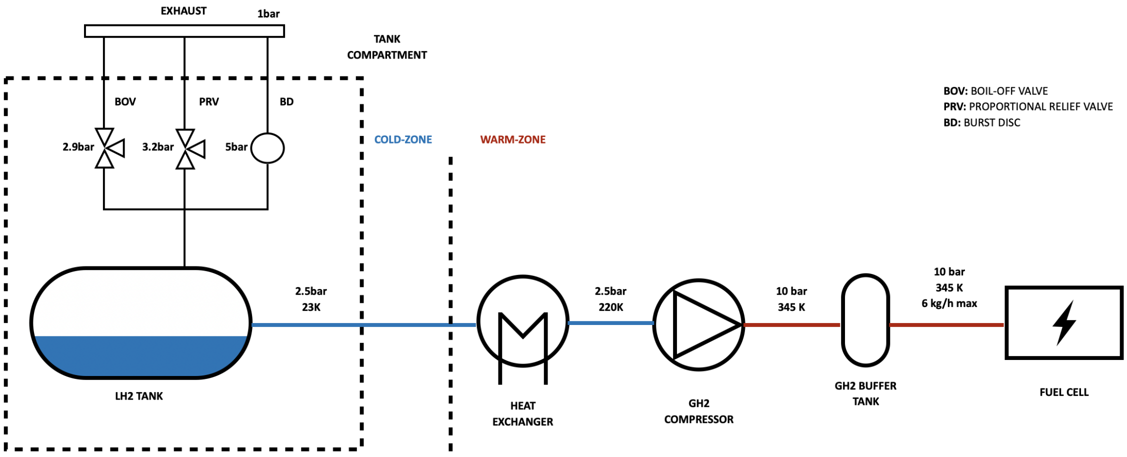

Figure 3.16: LHSS Plant Model Alternative Overview - Systems and Operating Conditions

As shown above, the compressor is positioned downstream of the heat exchanger, as it operates with gaseous hydrogen as the working fluid. In this configuration, the compressor delivers the hydrogen to the buffer stage at the required pressure. after the heat exchanger. As a consequence of the compression process, the fluid experiences a significantly higher temperature rise compared to the pump configuration. This difference originates from the distinct thermal properties of the respective working fluids. To preserve the boundary conditions of the plant, the heat exchanger must therefore be resized to reduce the outlet temperature accordingly.

Figure 3.17 provides an overview on the model implementation in GT Suite, where the entire fuel supply line from the tank to the fuel cell inlet is presented.

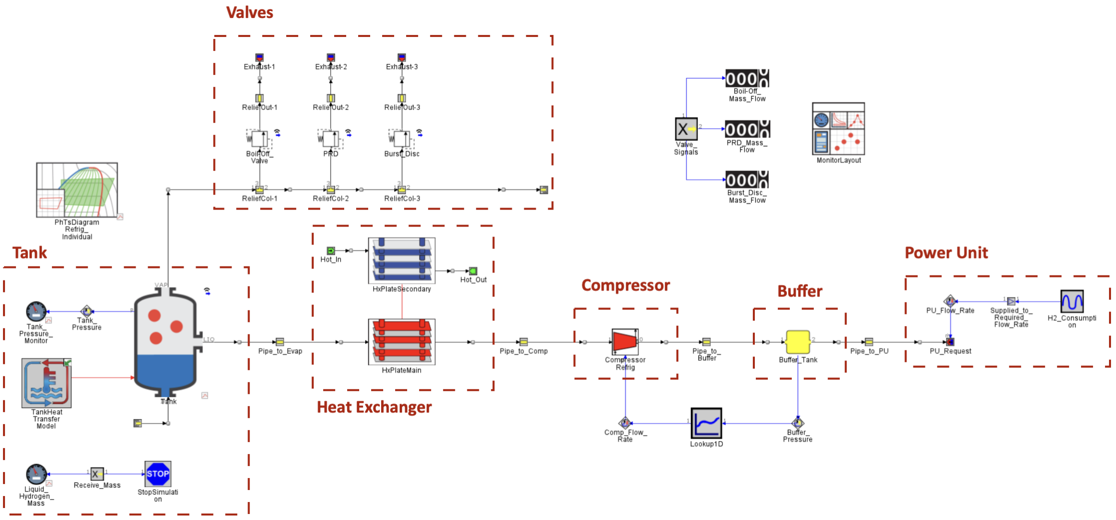

Figure 3.17: LHSS Plant Model Alternative Overview with GT Suite Interface

The compressor is modeled by prescribing a mass flow rate with the same control logic as the one applied to the pump model. This approach ensures that the buffer tank pressure remains at the desired level, thereby reducing oscillations induced by the variable fuel flow demand of the power unit.

More, two other parameters are defined:

- **Isentropic Efficiency:** allows the effect of irreversibility to be accounted for in terms of the actual and isentropic work amount as shown in figure 3.18. It is defined as the ratio of the work input in the isentropic process, to the work input in the actual process between the same inlet and outlet pressures. If the kinetic and potential energies are negligible, the isentropic efficiency is reduced to the enthalpy difference ratio of equation 3.36:

$$\eta_{isentropic} = \frac{h_{2s} - h_1}{h_2 - h_1} = \frac{\Delta h_{isentropic}}{\Delta h} \tag{3.36}$$

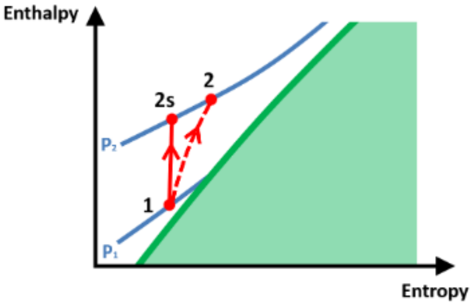

Figure 3.18: Compressor h-s Diagram

- **Mechanical Efficiency:** this can include friction and bearing losses, as well as motor losses. The value will be used to compute the total power consumption from the fluid power in equation 3.37:

$$P_{tot} = \frac{P_{fluid}}{\eta_{mech}} \tag{3.37}$$

Table 3.9 goes over the main parameters chosen to model the component:

Geometry	Unit	Value
Isentropic efficiency η_{is}	–	1
Mechanical efficiency η_{mech}	–	1

Table 3.9: Compressor model setup parameter list

4

Results

This chapter presents the results of the simulations carried out on the models introduced in chapter 3. At first, an analysis of the overall operation of the LHSS will be presented, focusing on the behavior of the individual subsystems and their interaction with the FCEV. This is followed by a comparison with the gaseous hydrogen vehicle configuration, providing an initial assessment of the differences between the two technologies. A more detailed investigation of the tank model is then carried out under both static and dynamic conditions, with particular attention to heat leakage as well as thermal stratification and sloshing effects. In addition, the validation of the heat exchanger model is addressed, emphasizing the impact of its integration on the vehicle as a whole. Finally, the results of a preliminary study of an alternative LHSS layout including a compressor stage will be presented.

4.1. Full Line Model

To best describe the behavior of the fuel throughout the entire two-phase circuit, state diagrams are employed. These provide an insight into the thermodynamic state of the fluid at the different stages of the LHSS and are shown in figure 4.1.

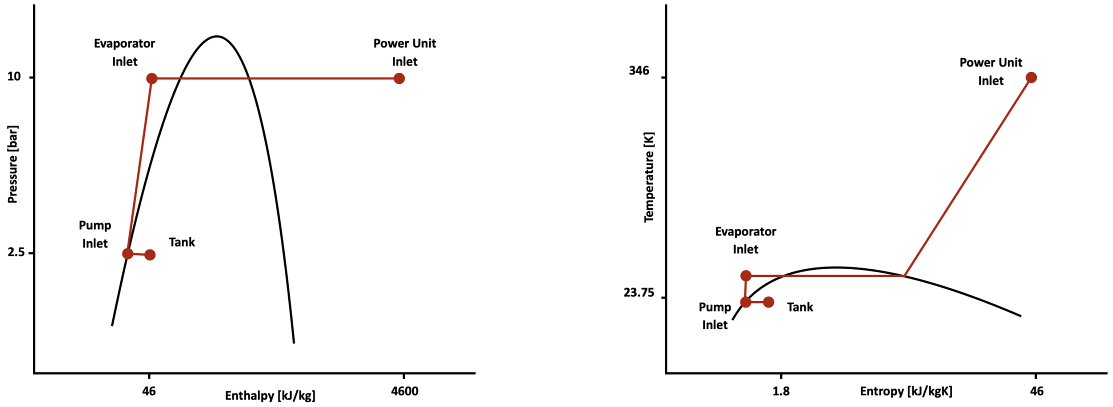

Figure 4.1: Pressure-enthalpy (left) and temperature-entropy (right) state diagrams of the entire system

The main thermodynamic processes can be summarized as follows:

- Isentropic Compression in the Pump
- Isobaric Evaporation in the Heat Exchanger

As illustrated in figure 4.1, the storage tank contains a two-phase mixture of liquid and gaseous hydrogen in thermodynamic equilibrium. At the pump inlet, only saturated liquid hydrogen is present, which then enters the evaporator as subcooled liquid. Within the evaporator, the fluid undergoes a phase change and eventually reaches a superheated state, being delivered as gaseous hydrogen at the required temperature and pressure to the power unit inlet.

4.1.1. System Operation

As mentioned in section 3.1, the system has been validated by analyzing the vehicle behavior during one lap around the Mugello racing circuit. Following the plant overview of figure 3.1, the outputs of the individual subsystems starting from the tank up to the fuel cell will be presented.

Tank Compartment

Starting with the storage tank, the profiles of the main variables that describe the system are presented in figure 4.2.

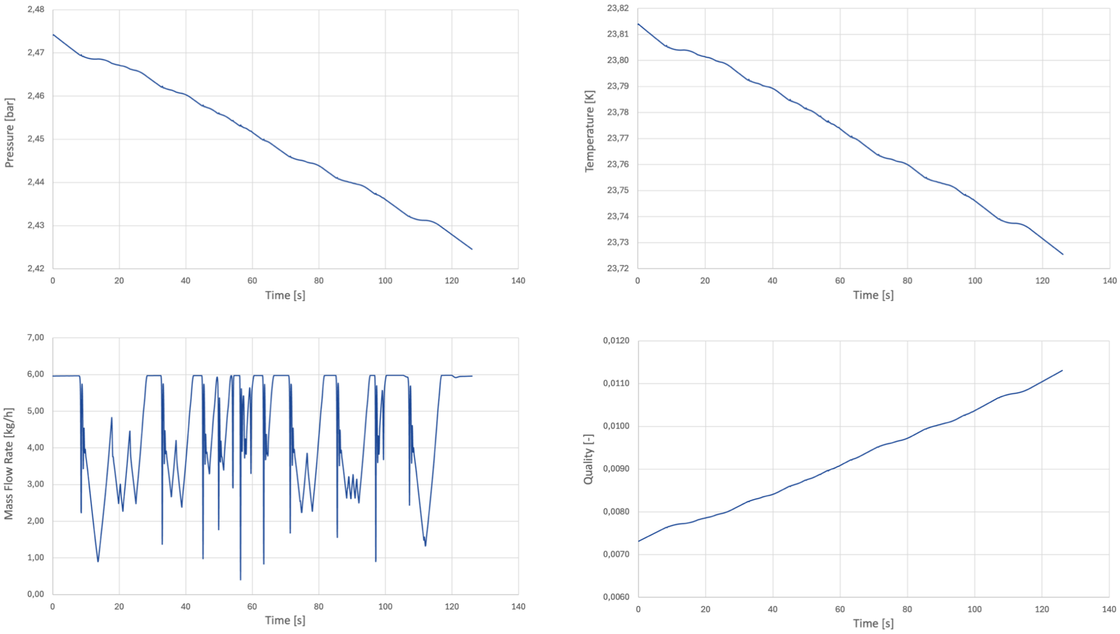

Figure 4.2: Tank pressure (top-left), temperature (top-right), mass flow rate (bottom-left) and quality (bottom-right) profiles

At first, it is possible to observe is that the pressure inside the tank is slowly decreasing. This behavior arises from the fact that, although a portion of liquid hydrogen evaporates due to heat leakage, the outflow of liquid hydrogen from the tank, shown in the bottom left plot, is approximately two orders of magnitude greater than the evaporation rate. As a result, the MEOP is never reaches, and the relief valves do not open. The mass of gaseous hydrogen in the tank is therefore slightly increasing, which is reflected in the upward trend of the quality profile.

The model also outputs a single bulk temperature for the tank, as the liquid and vapor phases are assumed to be in thermal equilibrium, and uniformly distributed. While this represents a reasonable approximation under dynamic operating conditions, thermal stratification could influence the thermal distribution during static conditions. this aspect will be further investigated through simulations using the 3D CFD model presented in section 3.2.

To gain further insight into the behavior of the relief valves, a boil-off simulation is done under static conditions, in which the vehicle remains stationary and no liquid hydrogen is flowing out of the tank. The simulation is conducted over the entire emptying process of the tank with a lower threshold defined by a minimum fuel mass of $m_{fuel,min} = 0.1\,kg$.

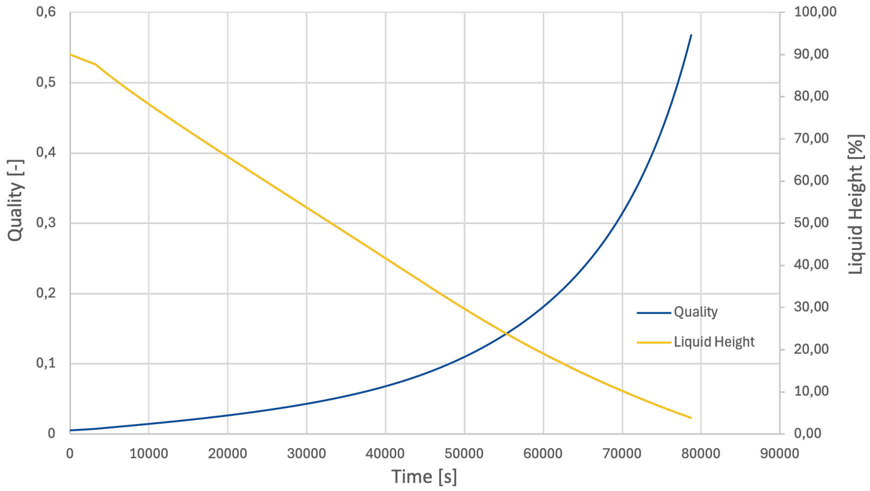

Figure 4.3: Tank quality and liquid height profiles

Figure 4.3 illustrates the evolution of the mixture phase composition during the emptying process. As a consequence of the boil-off, the liquid height in the tank gradually decreases, while the vapor quality exhibits a corresponding increase.

The heat leakage of the tank is computed using the coupled thermal model introduced in section 3.2 and corresponds to $q = 12.50\, W/m^2$. This value is constant throughout the entire process, since both the internal wall temperature and the bulk fluid temperature remain essentially unchanged. The latter outcome results from the assumption of a uniform temperature distribution within the tank, which as previously described above, may introduce inaccuracies under static conditions. The implications of this assumption will be examined later in section 4.2.2.

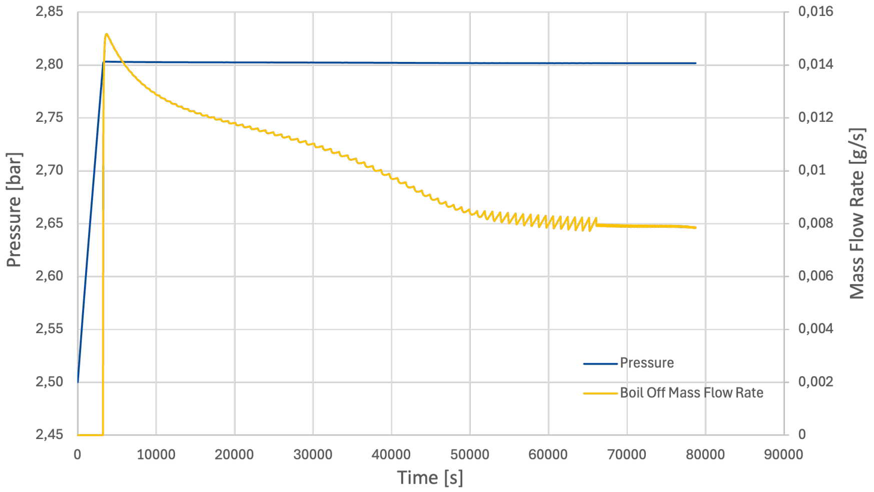

Figure 4.4: Tank pressure and boil-off valve mass flow rate

Figure 4.4 provides an insight into the dynamics of the Boil-Off valve. This pressure-driven device begins to open when the pressure drop across the valve approaches the cracking pressure drop, which is set to $p = 2.8\, bar$. At this point, gaseous hydrogen will start to flow out of the tank through the valve, which will record a peak of flow rate at around $m_{bo} = 0.015\, g/s$. Subsequently, the flow rate decreases as the vapor quality within the tank increases, indicating that progressively smaller amounts of hydrogen must be vented in order to maintain the internal pressure at the prescribed level.

This analysis provides a first estimate of the dormancy and boil-off time of the system, while also confirming that the hydrogen release rates remain below the limits prescribed by the FIA for LHSS design in this application. For a tank with the given geometry and heat flux, these values correspond to:

$$t_d = 4977\,s \approx 1.4\,h$$

$$t_{bo} = 78753\,s \approx 21.9\,h$$

$$\dot{m}_{bo,max} = 0.015\,g/s$$

Pipe

As mentioned in section 3.1, the pipes in the systems are modeled as adiabatic but flow losses due to friction along the walls will affect the pressure profile. Despite the modeled smooth surface having minimal roughness, the friction losses induce a minimal certain pressure drop that can be considered negligible.

Pump and Buffer Logic

The pump imposes a mass flow rate in the middle of the circuit, which is regulated by the feed-forward control strategy described in section 3.1. The resulting target static pressure rise is an output of the model and displayed in figure 4.5.

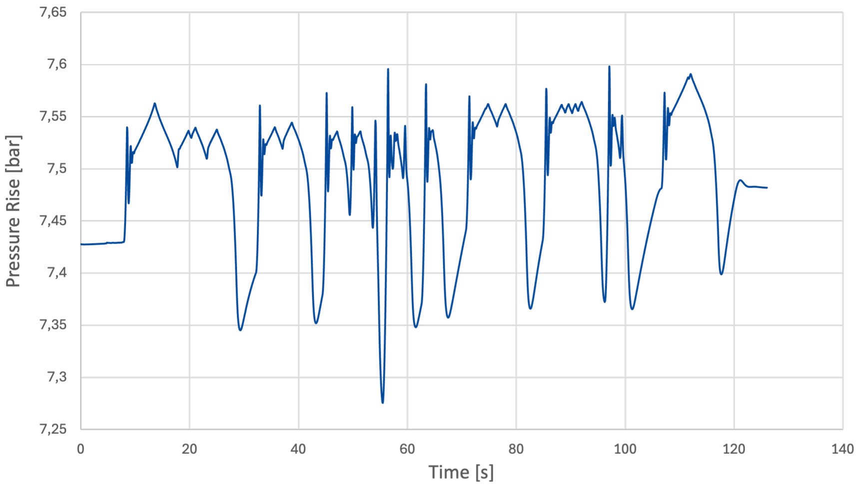

Figure 4.5: Pump static pressure rise - output signal of the control strategy

To further assess the correct operation of the control logic, figure 4.6 examines a representative time window of the simulation, illustrating the relationship between the requested and supplied pump mass flow rates and the corresponding buffer pressure, which ultimately determines the pressure rise.

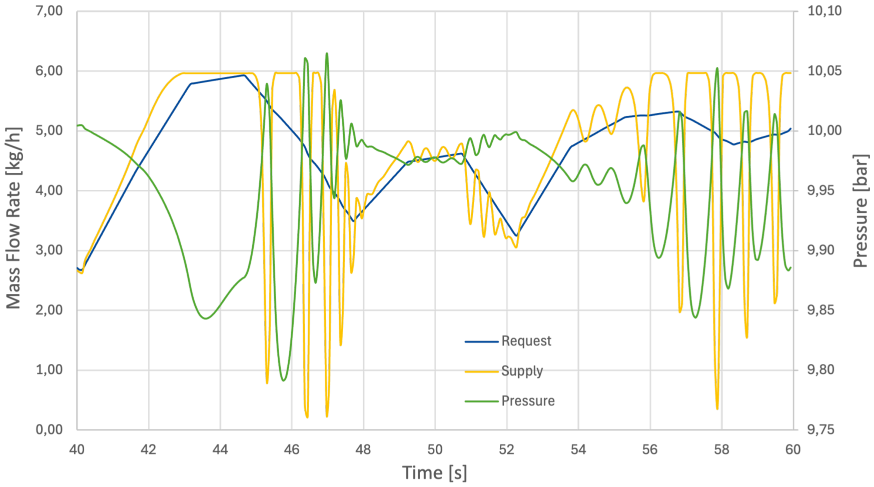

Figure 4.6: Pump and buffer control strategy

At $t = 40\,s$, the PU demands an increased fuel mass flow rate to satisfy higher power requirement. Consequently, the buffer begins to discharge, leading to a pressure drop below the prescribed threshold. This pressure deviation acts as an input to the control logic, which maps the corresponding pressure to an appropriate pump mass flow rate. The pump then fills up the buffer once more, restoring its pressure to the target value.

Concerning the buffer model, a more detailed analysis is carried out to investigate the relationship between the buffer volume and maximum pump flow rate. In this study, the maximum mass flow rate requested by the PU is set as $\dot{m}_{max} = 6\,kg/h$, while the pump flow rate can vary in an interval of $\dot{m}_{pump} = 4\,kg/h - 9\,kg/h$. Figure 4.7 reports the minimum plenum pressure as a function of the maximum pump flow rate for different buffer volumes, ranging from $V_{buffer} = 1\,l - 10\,l$.

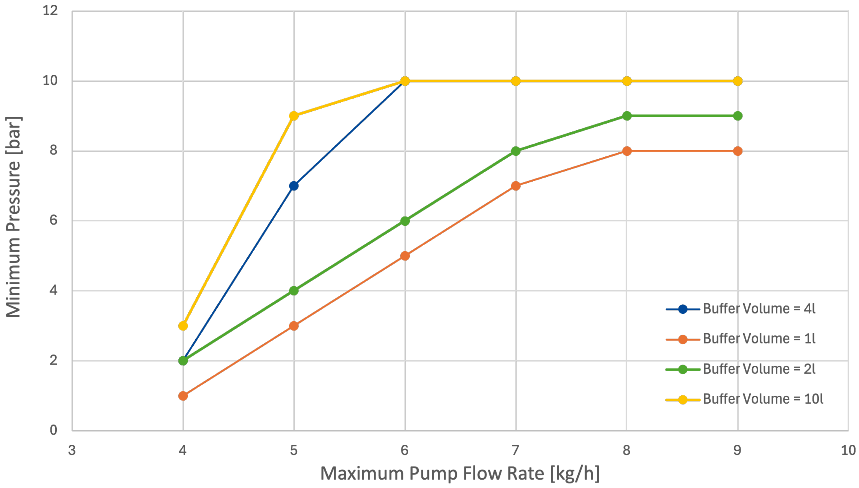

Figure 4.7: Minimum buffer pressure as a function of the maximum pump flow rate for different buffer volumes

As expected, larger plenum volumes are able to keep a higher pressure at a given mass flow rate. To maintain the target pressure of $p_{target} = 10\,bar$ at the maximum requested mass flow rate, the pump flow rate cannot fall significantly below the required threshold Consequently, the smaller plenums are unable to satisfy the target, which can be achieved by buffer volumes of $V_{buffer} = 4\,l$ or higher.

In fact, a bigger buffer volume allows to better compensate for fluctuations in requested fuel mass flow rate, thus gaining a better control over the target pressure. This difference can be observed in figure 4.8, where the pressure and mass flow rate profiles for two different plenum sizes are displayed.

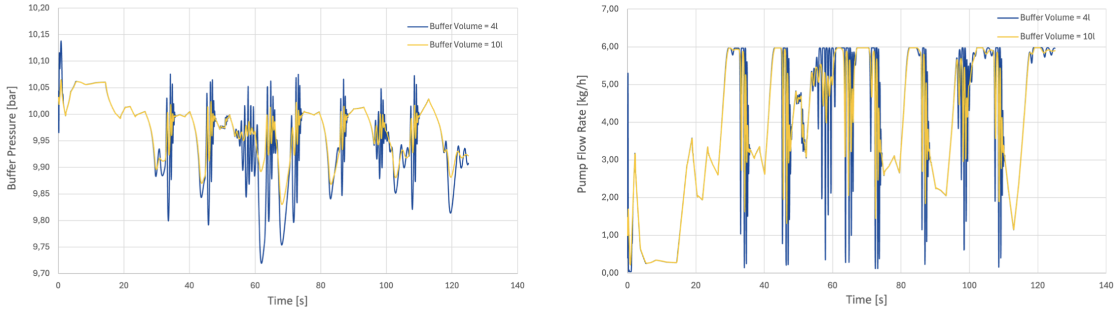

Figure 4.8: Buffer mass flow rate (left) and pressure (right) profiles for two different volumes

A considerable difference can be observed between the cases, as the bigger volume is represented by a smoother pressure and mass flow rate profile.

Heat Exchanger

The heat exchanger model introduced in section 3.1 was designed to meet the temperature requirements displayed in figure 4.9.

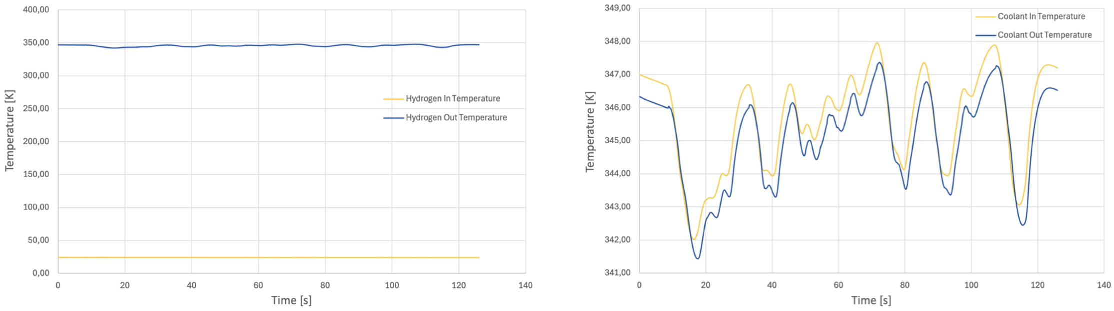

Figure 4.9: Cold fluid (left) and hot fluid (right) inlet and outlet temperature profiles

A shown, the cold fluid is heated up to the target temperature of $T_{target} = 346\,K$ while simultaneously undergoing phase change. On the coolant side, the fluid experiences a modest decrease in temperature, which is to be attributed to the substantially higher mass flow rate of $m_{EGW,max} = 8280\,kg/h$ compared to the one on the main side stream. More, the target pressure is not affected by the friction losses within the heat exchanger, as these can be considered to be almost negligible on both the hydrogen and coolant sides.

Power Unit Integration

Initially, as mentioned in section 3.1, integration of the LHSS into the FCEV was constrained by a limitation of the simulation tool, which required the fuel supply line and the anode side of the fuel cell to be modeled as two separate circuits. To overcome this, a continuity condition was imposed at the interface, thus allowing the vehicle to operate on liquid hydrogen. This implementation is validated by the plots in figure 4.10, which demonstrate that the boundary conditions for pressure, temperature, and mass flow rate are accurately satisfied.

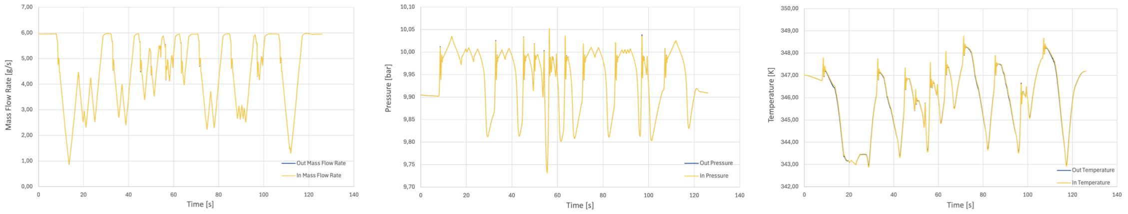

Figure 4.10: Boundary mass flow rate (left), pressure (mid) and temperature (right) of the two circuits

Moving to the final part of the circuit, the fuel now enters the anode circuit and ahead of entering the fuel cell, it mixes with the recirculated hydrogen that is injected back into the system. The fuel supply to the power unit is therefore the sum of these two quantities and is displayed in figure 4.11.

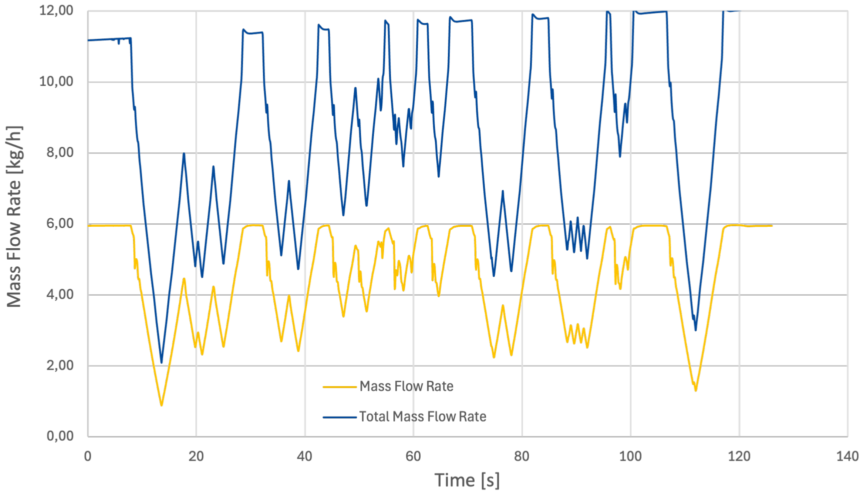

Figure 4.11: LHSS supplied hydrogen (yellow) and total fuel supply into the fuel cell (blue)

At last, it is important to underline the relationship between the required fuel flow rate and the vehicle's dynamic behavior. As the vehicle follows the prescribed speed profile of the Mugello race track, it must deliver the corresponding torque and power. As described in section 2.1.1, this power demand is shared between the battery and the fuel cell. This device will then provide the appropriate voltage and current by converting the chemical energy associated with the reaction between hydrogen and oxygen. The electrical energy generated is directly related to stoichiometric ratio of the reaction, thus the amount of hydrogen fuel requested to produce a certain power. This process is best illustrated in figure 4.12, which concludes the general overview on the system operation, from the tank up to the fuel cell of the vehicle.

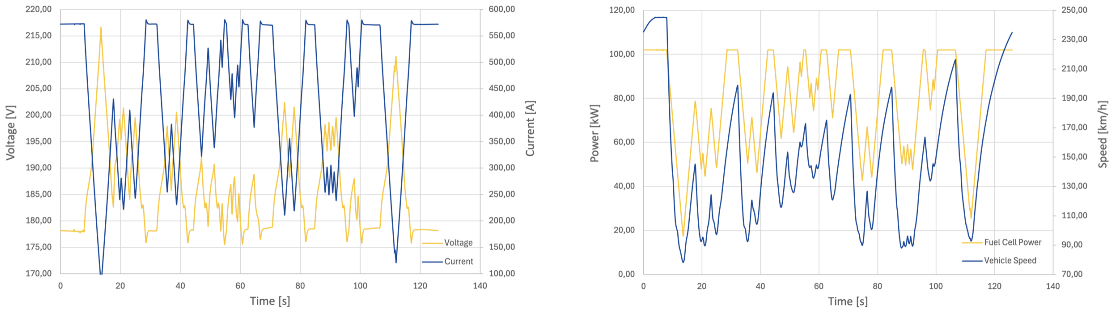

Figure 4.12: Fuel cell electrical energy relation to hydrogen supply

4.1.2. Technology Comparison

This section focuses on evaluating the differences between the liquid and gaseous fuel supply systems for the fuel cell electric vehicle. To be more specific, these two configurations will be assessed in terms of range of the vehicle, which can be limited by two main factors:

- **Battery Capacity:** as one of the two main power sources of the vehicle, the battery size, thus energy storage directly affects the achievable driving range
- **Hydrogen Storage Capacity:** while liquid hydrogen offers a higher energy density compares to its gaseous form, the packaging constraint of the onboard storage tank limits the quantity that can be carried, thereby influencing the overall range.

To quantify these effects, three simulation scenarios were conducting, differing in fuel type (liquid or gaseous hydrogen) and vehicle mass. The liquid hydrogen configuration has a total vehicle mass of $m_{vehicle,l} = 1400\,kg$, whereas the gaseous hydrogen configuration is slightly lighter at $m_{vehicle,g} = 1370\,kg$. The additional mass is attributed to the LHSS, which requires extra components such as the cryogenic pump and heat exchanger. The weight of these components was estimated from preliminary design data and industry references for similar systems.

From a vehicle dynamics perspective, the increased mass results in higher energy losses, primarily due to greater rolling resistance. These losses are quantified as $\Delta E_{loss} = 43\,J$, corresponding to an approximate 0.5 % increase relative to the lighter configuration. Consequently a higher tractive force is required to maintain the same speed profile, leading to an increased overall power demand. Since the fuel cell operates near its maximum allowable power output, this additional demand is entirely supplied by the battery. Figure 4.13 illustrates this effect by comparing the battery power profiles of the different configurations.

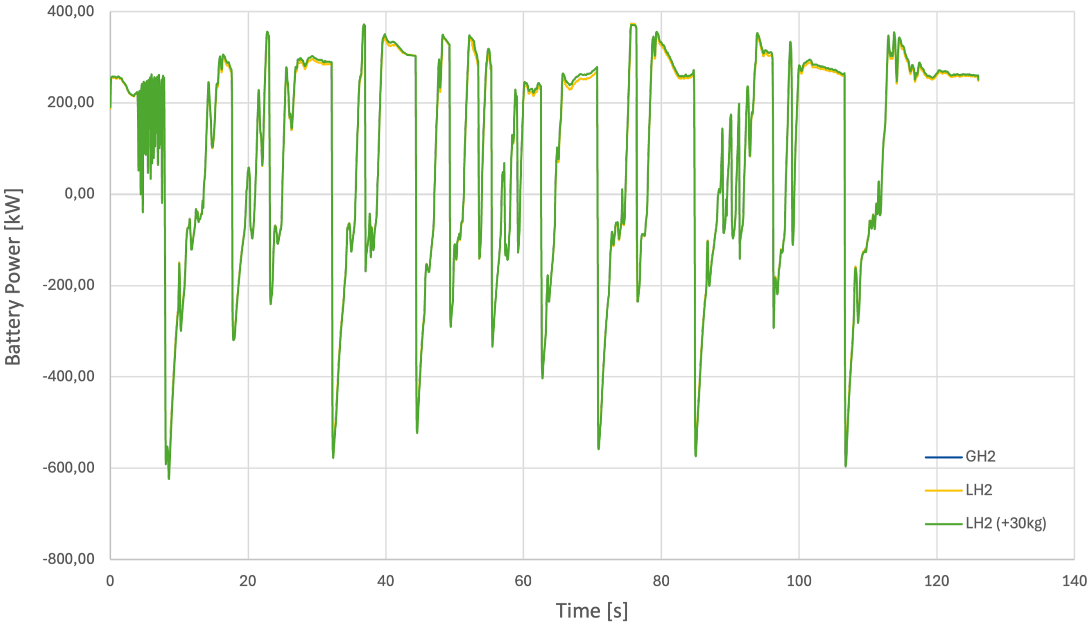

Figure 4.13: Battery power profile

As a result, the liquid hydrogen configuration exhibits a lower SOC, with a difference of approximately $\Delta SOC = 2\,\%$ of the total battery sized at $C_{batt} = 11.2\,kWh$ after a single lap. This corresponds to an estimated 4 % SOC depletion compared to the lighter gaseous hydrogen vehicle.

Furthermore, when considering the tank storage capacity as the limiting factor, the use of a LHSS results in a significant extension of the vehicle's driving range. During a single lap of the circuit, the filling level of the liquid hydrogen tank decreases by only $C_{H_2,eq} = 7.06\,\%$, which is 32 % less than if the gaseous hydrogen tank were to be used. This difference can be traced back to the ratio between the stored masses of the fluids at their operating conditions. At $T = 23\,K$ and $p = 2.5\,bar$, the fuel mixture in the cryogenic tank has a density of $\rho_{H2,mix} = 60\,kg/m^3$, thus an initial mass of $m_{H2,l} = 2.4\,kg$. For what concerns the gaseous hydrogen tank, at $T = 430\,K$ and $p = 700\,bar$, $\rho_{H2,g} = 40\,kg/m^3$ so that $m_{H2,g} = 1.6\,kg$, which is approximately 30 % less as expected.

Overall, the vehicle range is evaluated separately for the two limiting scenarios. When only the hydrogen storage capacity constraint is considered, the estimated ranges are $S_{H_2,l} = 74\,km$ and $S_{H_2,g} = 50\,km$ for the liquid and gaseous hydrogen powered vehicle respectively. If the battery size is taken into account, then these values drastically decrease to $S_{Batt,l} = 13\,km$ and $S_{Batt,g} = 14\,km$. These values are derived by computing the number of laps achievable with the respective hydrogen or battery consumption rates and multiplying by the track length of $L_{track} = 5.2\,km$. As expected, the battery proves to be the main limiting factor in this analysis, thus not allowing to fully explore the potential of a LHSS. In fact, when accounting for the additional weight of the LHSS components, the total range of the liquid hydrogen vehicle becomes slightly lower than that of the gaseous configuration.

To further investigate the theoretical advantage of liquid hydrogen, a sensitivity analysis was performed to identify the battery capacity required for the vehicle range to be constrained by tank depletion rather than by battery discharge. In this analysis, the additional weight associated with a larger battery was neglected to isolate the storage effect. The results presented in figure 4.14 provide a first comparison of the range potential between the two storage technologies.

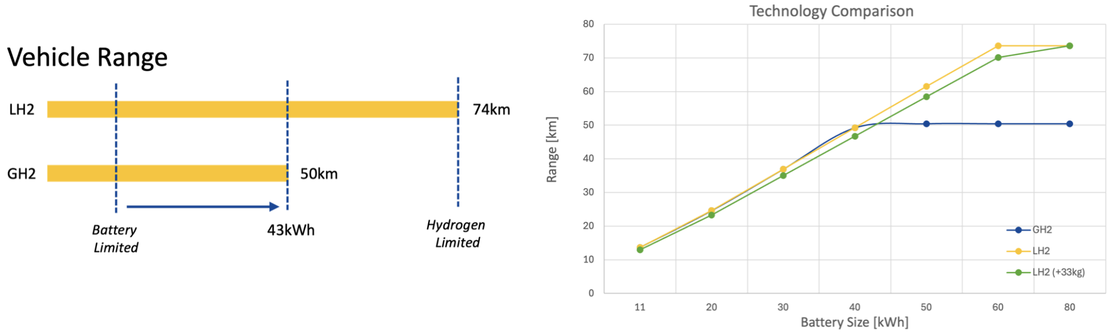

Figure 4.14: Technology comparison with varying battery size

As shown in the results, once the battery capacity exceeds $C_{batt} = 43\,kWh$, the vehicle's range becomes limited by the fuel storage rather than the battery, allowing the LHSS to demonstrate a clear advantage in driving range. In fact, after crossing that threshold, the range of the gaseous hydrogen configuration no longer increases with additional battery capacity, indicating that the storage tank becomes the dominant limiting factor. These findings are summarized in the table of figure 4.15, where the overall range is reported as the minimum of the values found in the two scenarios described.

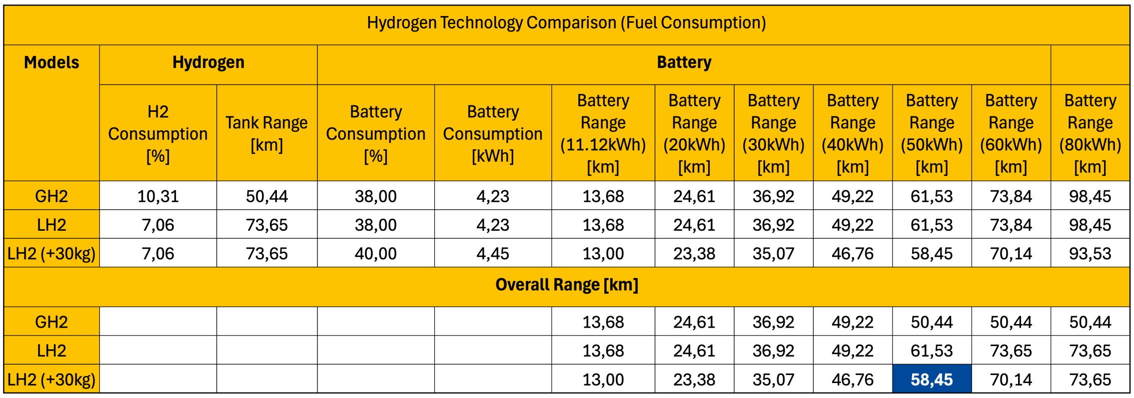

Hydrogen Technology Comparison (Fuel Consumption)										
Models	**Hydrogen**		**Battery**							
	H2 Consumption [%]	Tank Range [km]	Battery Consumption [%]	Battery Consumption [kWh]	Battery Range (11.12kWh) [km]	Battery Range (20kWh) [km]	Battery Range (30kWh) [km]	Battery Range (40kWh) [km]	Battery Range (50kWh) [km]	Battery Range (60kWh) [km]	Battery Range (80kWh) [km]
GH2	10,31	50,44	38,00	4,23	13,68	24,61	36,92	49,22	61,53	73,84	98,45
LH2	7,06	73,65	38,00	4,23	13,68	24,61	36,92	49,22	61,53	73,84	98,45
LH2 (+30kg)	7,06	73,65	40,00	4,45	13,00	23,38	35,07	46,76	58,45	70,14	93,53
Overall Range [km]											
GH2					13,68	24,61	36,92	49,22	50,44	50,44	50,44
LH2					13,68	24,61	36,92	49,22	61,53	73,65	73,65
LH2 (+30kg)					13,00	23,38	35,07	46,76	**58,45**	70,14	73,65

Figure 4.15: Technology comparison study table results

4.2. Tank Model

As outlined in section 3.2, several key aspects were addressed in the development of the tank model. First, the influence of varying external conditions and of heat leakage on the dormancy and boil-off behavior is examined. More, the outcomes of the 3D CFD and particle based simulations are presented to evaluate thermal stratification and fuel sloshing within the tank.

4.2.1. Heat Leakage

This section examines the influence of tank insulation on the overall heat flux and dormancy time, thereby summarizing the key finding of the thermal modeling approach applied to the tank system.

Static vs Dynamic Conditions

This study is carried out to evaluate whether the mixing between the phases that occurs in dynamic conditions could potentially increase the heat transfer between the fluid and the wall. This effect can be quantified by analyzing dormancy time and heat flux in the tank based on the heat transfer coefficient indicated as fluid convection in figure 3.11.

In static conditions, the free convection coefficient is obtained from figure 3.10. With a temperature difference between the internal wall and fluid of $\Delta T = 0.1\,K$ nucleate boiling occurs, thus providing a heat transfer coefficient of

$$h_{static} = 140\,W/m^2K.$$

Under dynamic conditions, the tank is subject to external forces deriving from the acceleration of the vehicle, whose profile is illustrated in figure 3.13. To capture this effect, the 3D sloshing simulation on Particleworks is used to report the particle velocity profile displayed in figure 4.16:

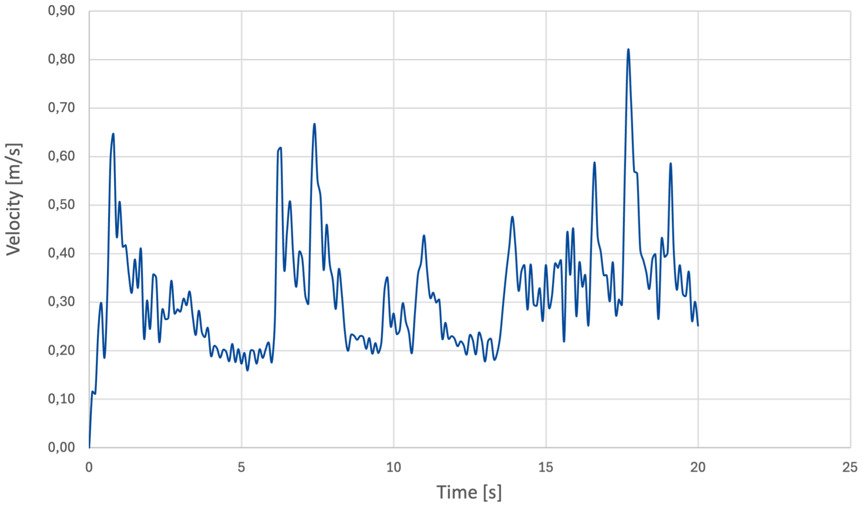

Figure 4.16: Individual particle velocity within the tank under external forces

From an average particle velocity of $v_{avg} = 0.32\,m/s$ and using the forced convection equation 3.19 gives a heat transfer coefficient for dynamic conditions of

$$h_{dynamic} = 2500\,W/m^2K.$$

Despite the significant increase in heat transfer coefficient, the overall heat flux inside the tank remains nearly unchanged. This is primarily because the tank's insulation minimizes the wall-fluid temperature difference, preventing any meaningful reduction in dormancy time under dynamic conditions.

MLI Sensitivity

As mentioned in section 3.2, the tank insulation consists of a vacuum gap, where multiple reflective layers are placed between the two concentric shells.

An initial study was conducted to evaluate how the use of vacuum and MLI affects heat flux and, consequently, dormancy time. Three insulation configurations were analyzing, and the resulting heat leakage is shown in figure 4.17:

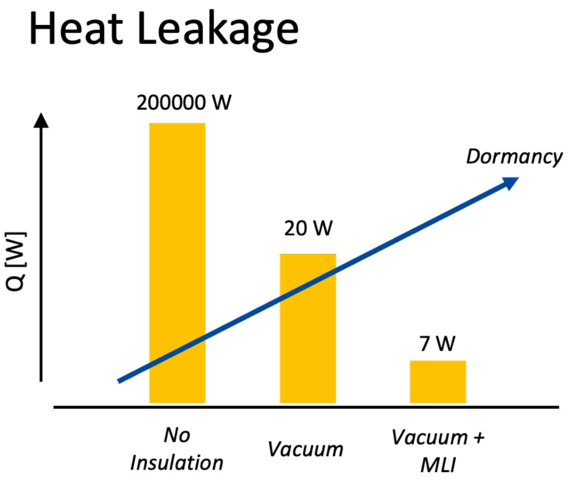

Figure 4.17: Tank insulation effects in three different scenarios

The results clearly demonstrate that MLI technology significantly reduces the heat rate in the tank, thereby increasing dormancy time. Moreover, the presence of a vacuum layer is essential for maintaining cryogenic temperatures, as it keeps heat flux levels far below those of a conventional fuel tank In fact, the loss of vacuum in the tank represents on of the major challenges in the design. This effect increases the heat flow by multiple orders of magnitude, which implicates the following:

- once the MEOP is reached, the pressure can no longer be decreased again down via the oil-off path, so that additional PRV's such as the ones displayed in figure 3.4 need to open to avoid burst
- the absence of vacuum cannot be adequately managed within the operational limits of the boil-off valve

Accurately quantifying this failure scenario would require modeling complex phenomena such as material rupture and the mixing of hydrogen with the outside air mixture. In this study, the no vacuum case is simplified as an uninsulated tank scenario for comparison purposes.

More, focus is placed on the MLI technology by studying its effects on heat leakage. Figure 4.18 displays the heat flux and corresponding heat transfer coefficient in relation to the number of MLI layers applied.

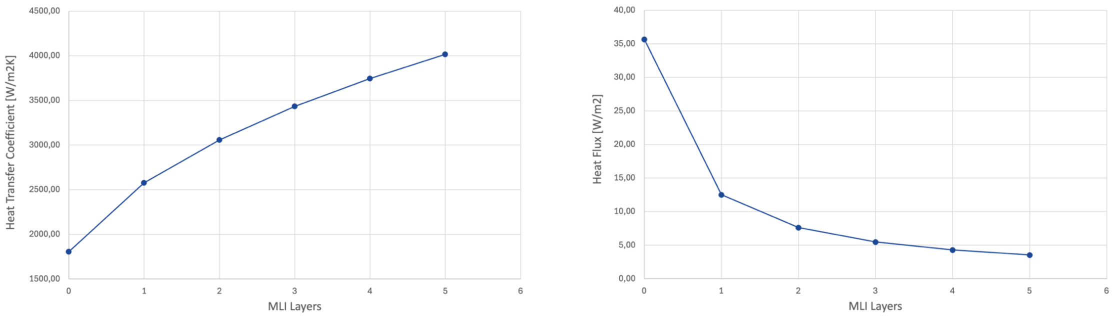

Figure 4.18: Tank heat transfer coefficient (left) and heat flux (right) in relation to the number of MLI layers

Increasing the number of MLI layers reduces the heat flux within the tank to values below $q = 5\,W/m^2$, beyond which additional layers provide diminishing returns while complicating the manufacturing process and keeping a proper vacuum within the tank. Consequently, the dormancy time improves significantly with MLI as illustrated in figure 4.19, where adding up to $n_{layers} = 5$ layers can increase it by a factor of 10.

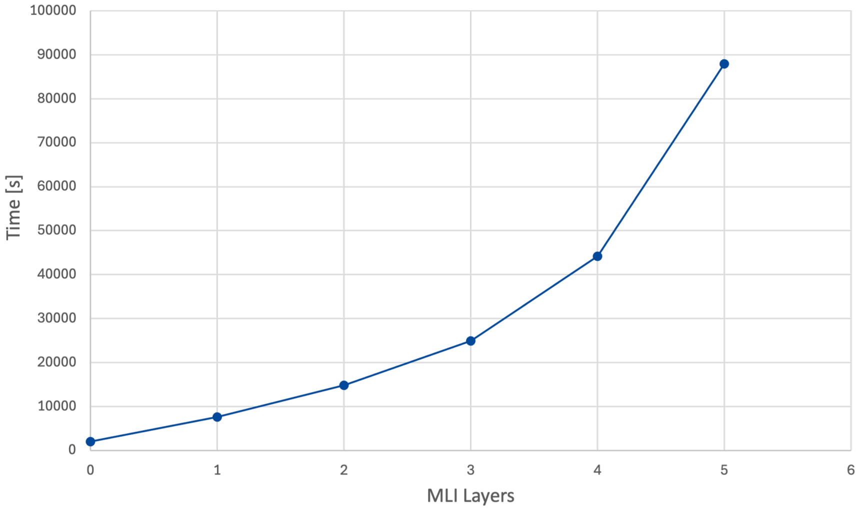

Figure 4.19: Tank dormancy time in relation to the number of MLI layers

Vehicle Temperature Sensitivity

Similarly, an analysis is done to examine the influence of the external vehicle temperature on the tank heat leakage. The objective is to estimate how variations in ambient temperature, represented as the boundary condition in figure 3.11, affect dormancy time. The results, which further validate the accuracy of the thermal model, are presented in figure 4.20.

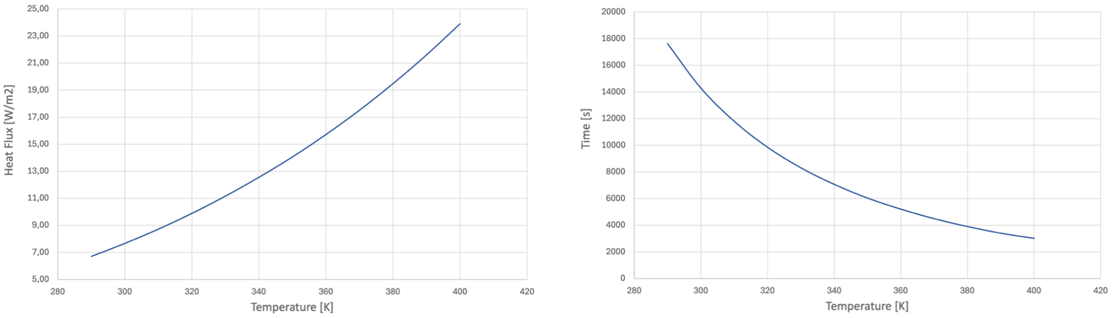

Figure 4.20: Tank heat transfer coefficient (left) and heat flux (right) in relation to the vehicle temperature

According to the heat transfer relationships expressed in equations 3.23 and 3.24, an increase in heat flux is expected as the temperature difference between the cryogenic fluid and the surroundings grows. In this study, the external temperature is varied in a range of $T_{vehicle} = 280\,K - 420\,K$, resulting in a total dormancy time reduction of approximately $t_d = 15000\,s$.

4.2.2. Thermal Stratification

One of the key assumptions in the tank model described in section 3.1 is that hydrogen can be treated as a uniform two phase mixture characterized by a single temperature profile. Based on the literature background presented in 2.1.3, this assumption is considered valid primarily under dynamic operating conditions, where external forces promote mixing between the liquid and vapor phases, thereby enhancing heat transfer. Under static conditions this phenomenon does not occur, and a temperature gradient appears to be developing within the tank. To assess the validity of this hypothesis, 3D CFD simulations are carried out to analyze the thermal stratification within the tank, and the resulting findings are presented below.

For the static scenario, the temperature distribution in the tank at a certain time step is displayed in figure 4.21.

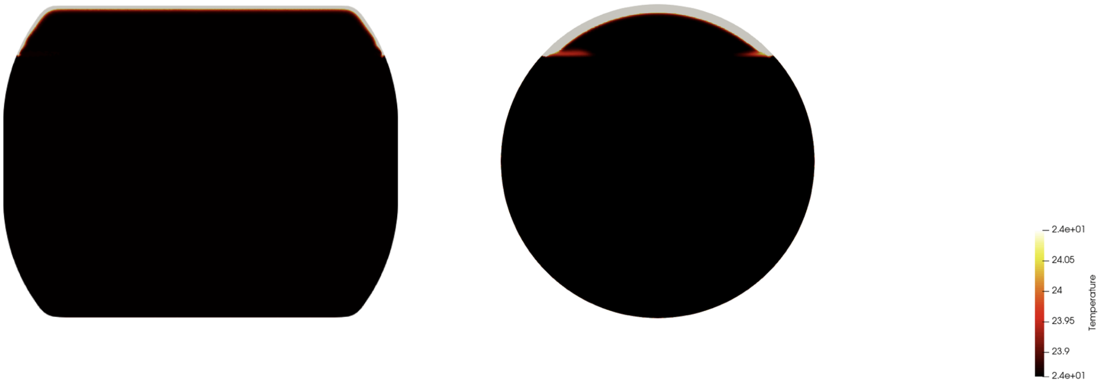

Figure 4.21: Temperature distribution in the static tank displayed on two different planes

It is clear that due to the imposed heat flux, a temperature gradient across the tank forms, which is driven by the evaporation of liquid hydrogen. This leads to the formation of a superheated liquid region and a subcooled vapor zone. A comparable output for the dynamic case is shown in figure 4.22.

Figure 4.22: Temperature distribution in the dynamic tank displayed on two different planes

Unlike the static case, external forces induce fluid motion mixing, resulting in a more uniform temperature profile. This allows to consider the assumption of hydrogen as a uniform two-phase mixture assumption as valid.

4.2.3. Sloshing

At last, the other phenomenon requiring a 3D analysis is the sloshing effect introduced in section 3.2. The first output of this study provided further insight into heat leakage associated with the forced convection induced by fuel movement within the tank. This was addressed in section 4.2.1 of the results part. The other objective of this study is to ensure that, under sloshing conditions and low filling levels, the pump doe not start to draw gaseous hydrogen from the tank.

For this purpose, two different tank designs have been developed and simulated under the external forces induced by the vehicle acceleration profile in figure 3.13. At a certain time step, the particle distribution and velocity gradients are displayed for the two different configurations in figure 4.23:

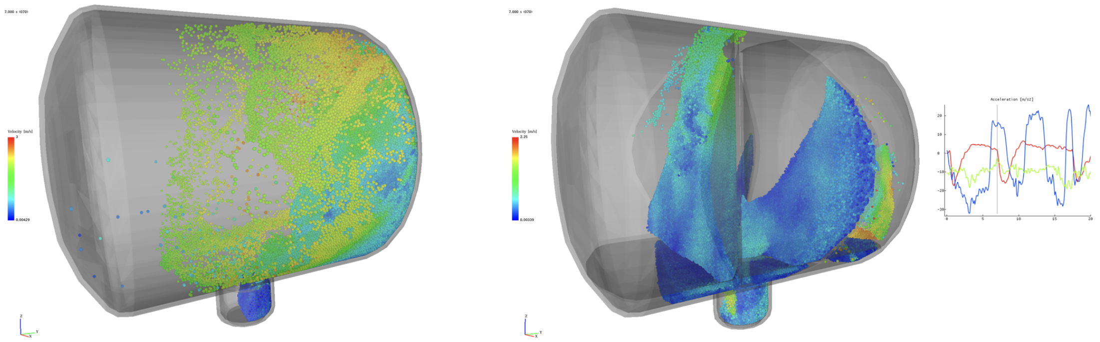

Figure 4.23: Tank particle distribution in no baffles (left) and baffles (right) configuration

As can be observed above in figure 4.23, the tank model without baffles on the left does not fully cover the pump outflow region at the bottom, allowing gaseous hydrogen to be drawn out. Additionally, the fluid particles are characterized by a greater velocity profile, which further enhances heat leakage effects within the tank. For these two reasons, two baffles are designed in the tank model shown on the right of figure 4.23. Under the same external forces acting on the tank, this configuration maintains the liquid phase more effectively within the tank outflow region, while at the same time reducing particle velocities. As a result, the baffle design enables to safely draw out fuel by limiting sloshing effects even at low tank filling levels.

4.3. Heat Exchanger Model

This section presents the results of the heat exchanger model study introduced in section 3.3. In particular, these will be classified into two main categories, reflecting the key criteria considered in the model's development. The first criterion addresses the design objectives, focusing on achieving the target hydrogen outlet temperature, while the second one concerns the component integration into the fuel cell cooling system.

4.3.1. Model Validation

This part will focus on presenting the results of the heat exchanger model in terms of output temperatures and energy rates of both the main and secondary side. This will include design, calibration and scaling considerations.

Design

As stated in section 3.3, the heat exchanger is composed of a stack of thin, corrugated plates arranged so that the two fluids flow in alternating channels. On the main side, the cold fluid flows exchanges heat with the hot fluid in a counter-flow configuration. An overview of the effective temperature distribution of the hydrogen flow across the plate is illustrated in figure 4.24.

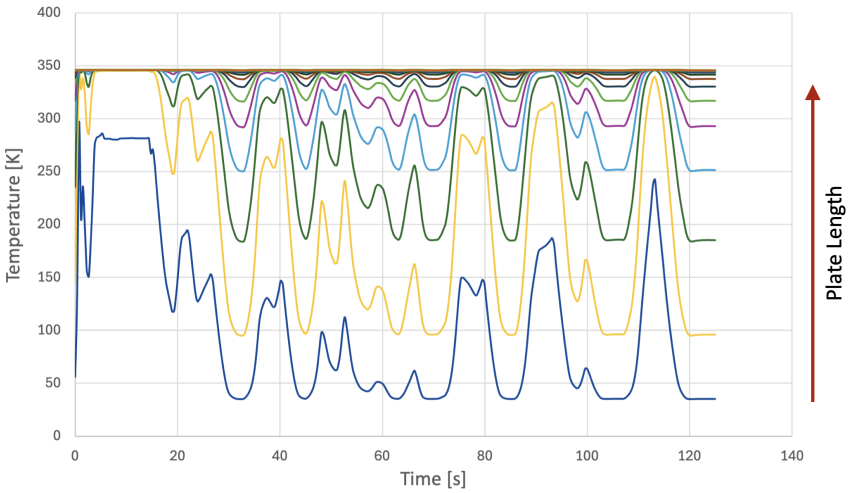

Figure 4.24: Cold fluid plate temperature distribution

The graph of figure 4.24 shows the temperature increase across the plate, which shows significant oscillations due to the varying mass flow rate of hydrogen that goes through the heat exchanger. The target outlet temperature of $T_{target} = 346\,K$ is already achieved halfway through the plate already.

The corresponding convective heat transfer rate and heat transfer coefficient of the hydrogen side are presented in figure 4.25.

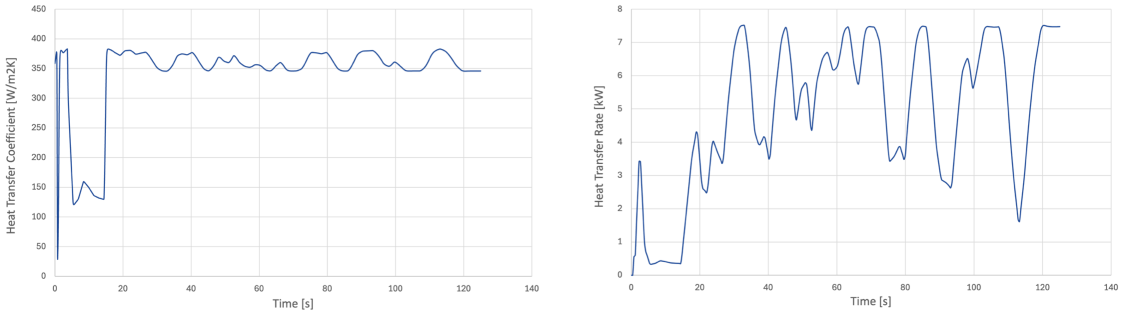

Figure 4.25: Convective heat transfer rate (left) and heat transfer coefficient (right)

During this process, the two-phase hydrogen mixture undergoes phase change, so that the energy rate required can be divided into three different contributions:

- Sensible heat $Q_{sens,l}$ part for liquid hydrogen to go from subcooled to saturated conditions
- Latent heat of vaporization Q_{latent} to transform liquid into gaseous hydrogen
- Sensible heat $Q_{sens,g}$ part for gaseous hydrogen to reach target outlet conditions

These different components combined make up the energy balance shown in figure 4.25. At a given mass flow rate of $\dot{m}_{H_2,max} = 6\,kg/h \approx 0.0017\,kg/s$, the total heat transfer rate equals to $Q_{tot} = 7.5\,kW$, which can be sub divided into

$$Q_{sens,g} = 0.2\,kW$$

$$Q_{latent} = 0.4\,kW$$

$$Q_{sensible,g} = 6.9\,kW$$

The heat transfer coefficients shown in figure 4.25 were determined using the empirical correlations presented in section 3.2.

Calibration Accuracy

During the modeling phase of the device, the heat transfer rate is calculated using heat transfer coefficients defined by an empirical correlation. These are then usually used for the calibration process and automatically fit to the experimental data provided by the manufacturer. In this case, the only data available concerned a cryogenic evaporator operating with R1234YF as the working fluid. To assess the applicability of this calibration to hydrogen, a comparative study is carried out at the maximum operating flow rates of

$$\dot{m}_{H_2,max} = 0.0017\,kg/s$$

$$\dot{m}_{EGW,max} = 2.5\,kg/s$$

The two different model configurations were compared and the results are here summarized in table 4.1:

Parameter	Calibrated	Analytical
Heat rate Q	7.40 kW	7.51 kW
Hydrogen outlet temperature $T_{H_2,o}$	340 K	346 K
Heat transfer coefficient h	320 W/m^2K	345 W/m^2K
Effectiveness ϵ_{eff}	0.97	0.99
Pressure Drop Δp	0.0010 bar	0.0020 bar

Table 4.1: Result comparison between calibrated and analytical model of heat exchanger

The comparison indicates that the calibrated model systematically underestimates both the heat transfer rate and the pressure drop relative to the analytical approach. This discrepancy can be attributed to two primary factors:

- Experimental data range: the supplier's calibration data is collected at flow rates outside of the range of those employed in this experimental site. Extrapolating the correlation beyond its validated range introduces uncertainty in the computed heat transfer and friction coefficients
- Single-phase reference fluid: the calibration is done using a single-phase refrigerant that does not undergo phase change, which represents a different operating condition than this case

For these reasons, the decision is made to use an analytical model for the heat exchanger based on the geometry provided by the company.

Scaling Analysis

The layout presented in section 3.3 is based on a preliminary geometry provided by the company on a cryogenic heat exchanger. Since an analytical model is employed, the geometry can be adjusted to control the resulting heat transfer rate and outlet temperature. In particular, the number of channels in the plate heat exchanger can be varied to evaluate scaling effects. Figure 4.26 shows the outcomes of this analysis, illustrating how the predicted heat rate and hydrogen outlet temperature change with the number of channels.

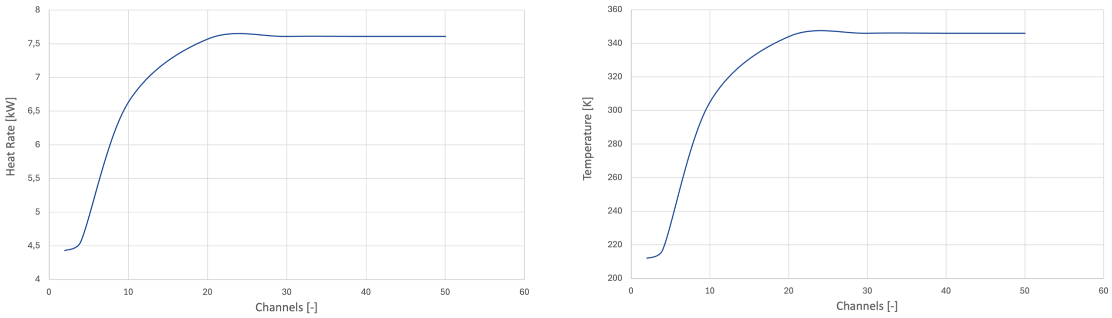

Figure 4.26: Heat rate (left) and hydrogen outlet temperature (right) in relation to the number of channels

As shown, the selected configuration with $n_{channels} = 40$ channels meets the target outlet temperature requirements. Moreover, the results indicate that the system could be further downsized to approximately $n_{channels} = 20$ while still achieving the desired thermal output.

4.3.2. Vehicle Integration

This part of the study will go over the integration process of the device into the vehicle. The resulting effects in terms of system integration, radiator sizing, fuel consumption and cooling pump requirements will be presented.

System Integration

As introduced in section 3.3, the heat exchanger operates using water as hot fluid. This design choice was made to be able to integrate the component into the existing fuel cell cooling cycle of the FCEV. The cooling system consists of a tube-fin heat exchanger that lowers the coolant temperature exiting the fuel cell. In this configuration, the plate heat exchanger is positioned between the fuel cell outlet and radiator inlet.

The impact of incorporating the cryogenic evaporator on the radiator's thermal characteristics is illustrated in figure 4.27, which compares the two configurations of the FCEV operating with liquid and gaseous hydrogen respectively.

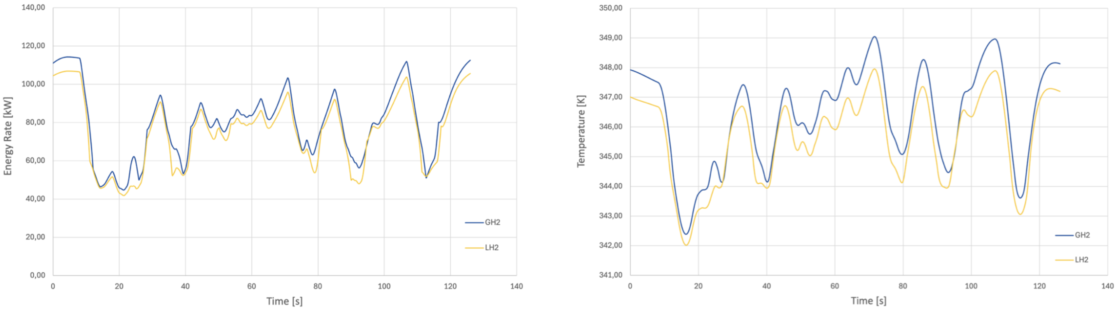

Figure 4.27: Fuel cell radiator thermal energy (left) and fuel cell coolant outlet temperature (right)

As expected, the plate heat exchanger induces a reduction in thermal energy of the radiator by already lowering the coolant flow temperature. Consequently, the coolant arrives at a lower temperature at the radiator inlet, reducing the amount of heat that needs to be removed from it. The addition of the cryogenic evaporator also leads to a slight overall reduction in the coolant temperature throughout the cycle.

Radiator Sizing

The results showed above indicate that, as a consequence of the integration of the plate heat exchanger into the cooling cycle, it would be possible to reduce the size of the fuel cell radiator to obtain the same thermal conditions as the original configuration of the gaseous hydrogen vehicle.

This analysis is based on the following assumptions:

- Ambient temperature $T_{amb} = 35\,°C$: chosen to represent a worst case scenario, where the radiator is exposed to hotter incoming air compared to the baseline $T_{amb} = 15\,°C$
- Constant fuel cell power $P_{FC} = 82\,kW$: ensures a steady fuel consumption rate and a constant mass flow rate of hydrogen through the plate heat exchanger of $\dot{m}_{H_2} = 0.0020\,kg/s$
- No coolant thermostat bypass: assumes a fixed coolant flow rate of $\dot{m}_{EGW} = 2.5\,kg/s$ throughout the cycle
- Constant vehicle speed $u_{vehicle} = 150\,km/h$: provides a steady flow of ambient air through the radiator
- Simplified cooling pump model: no performance map will be used but an imposed mass flow rate equal to $\dot{m}_{EGW}$

At first, the benchmark configuration with the fuel cell and radiator only is presented. Figure 4.28 shows a simplified scheme of the fuel cell cooling cycle with the corresponding heat rates and inlet and outlet coolant temperatures.

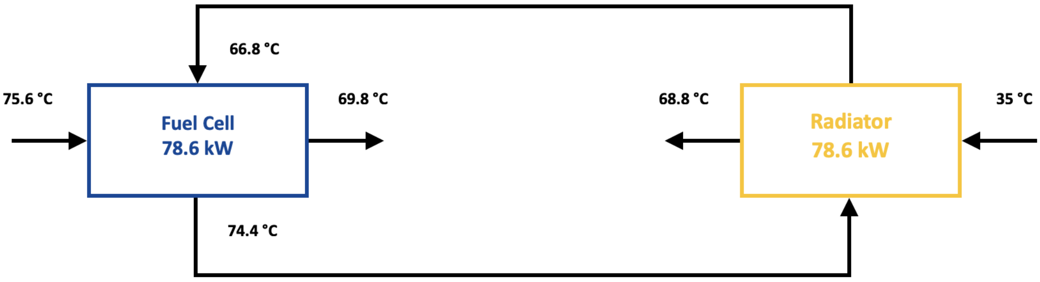

Figure 4.28: Fuel cell cooling cycle plant overview before integration

This configuration shows that the heat absorbed by the coolant in the fuel cell is balanced by the heat released through the radiator. Specifically, the coolant experiences a temperature increase of $\Delta T_{EGW} = 7.6\,°C$, while the air heats up by $\Delta T_{air} = 33.8\,°C$.

Once the plate heat exchanger is added to the system, the temperatures and heat rates look as shown in figure 4.29.

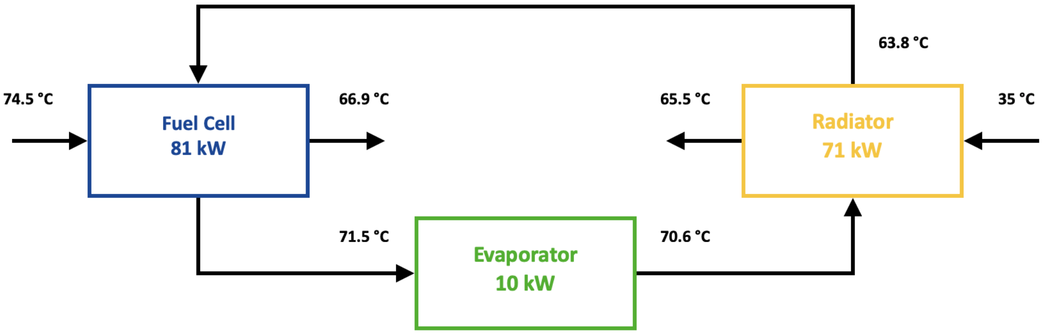

Figure 4.29: Fuel cell cooling cycle plant overview after integration

In this case, the total thermal energy to be dissipated by the coolant is shared between the evaporator and the radiator. This results in a reduction in temperature difference of both the coolant $\Delta T_{EGW} = 6.8\,°C$ and air $\Delta T_{air} = 30.5\,°C$.

To reach a similar configuration as the initial benchmark, the fuel cell radiator outlet temperatures can be altered by reducing its size. In a tube-fin heat exchanger, the area depends on two main parameters, the main channel length MC and stack height SH. These two are reduced to a value of $MC = 520\,mm$ and $SH = 410\,mm$, which result in an area that is 12 % smaller than the original geometry. The resulting cooling system profile after this radiator size reduction is shown in figure 4.30.

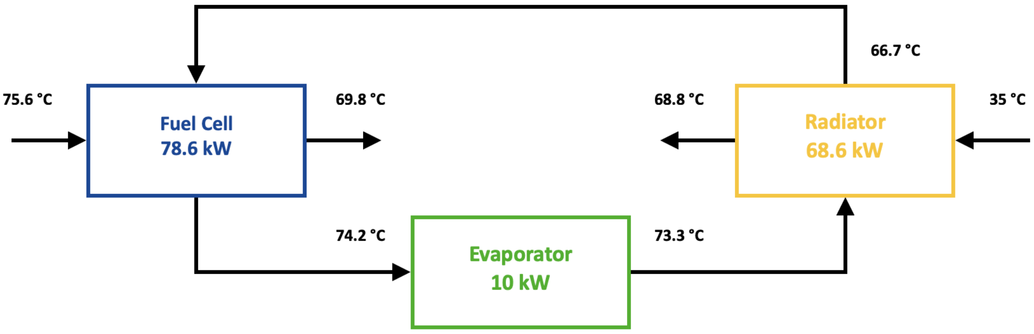

Figure 4.30: Fuel cell cooling cycle plant overview after integration and radiator sizing

As illustrated, the coolant inlet and outlet temperatures at the fuel cell now closely match those of the benchmark configuration, thereby confirming that the radiator size reduction compensates for the integration of the plate heat exchanger.

Cooling Pump Sensitivity

As mentioned in section 3.3, a key design consideration for the plate heat exchanger is the risk of channel freezing. The purpose of this analysis is to evaluate how operating conditions influence the likelihood of coolant freezing within the channels. Figure 4.31 illustrates the relationship between the coolant flow rate and the evaporator outlet temperature.

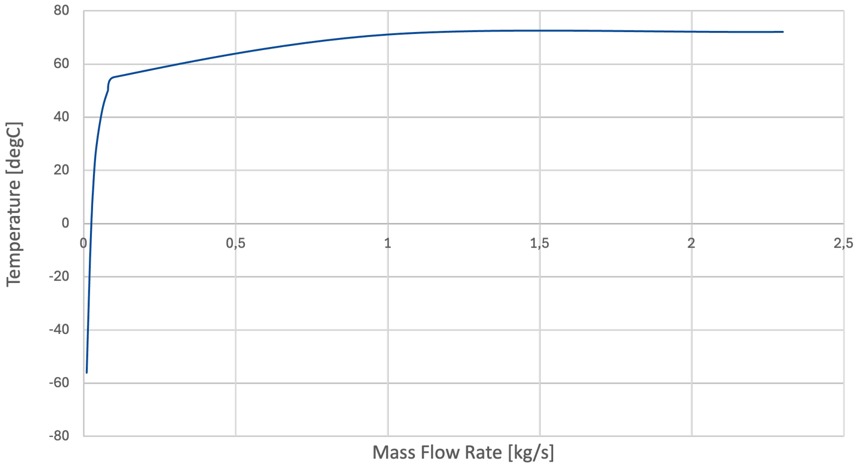

Figure 4.31: Fuel cell cooling pump flow rate with respect to the evaporator coolant outlet temperature

For the operating conditions considered, the average coolant flow rare is $\dot{m}_{EGW,avg} = 2.3\,kg/s$, which remains safely above the threshold where freezing might occur. The onset of freezing is predicted only at extremely low flow rates of around $\dot{m}_{EGW,f} = 0.025\,kg/s$, which is well below this operating range.

4.4. Layout Alternative Model

This section presents the results of the preliminary study of an alternative LHSS layout design that uses a compressor instead of a pump. This analysis first examines the system level implications of this design change and then outlines the potential strategies for integrating the new configuration.

As shown for the model in section 4.1, the state diagrams representing the modified two-phase circuit behavior are presented in figure 4.32.

The main thermodynamic processes in this case can be summarized as follows:

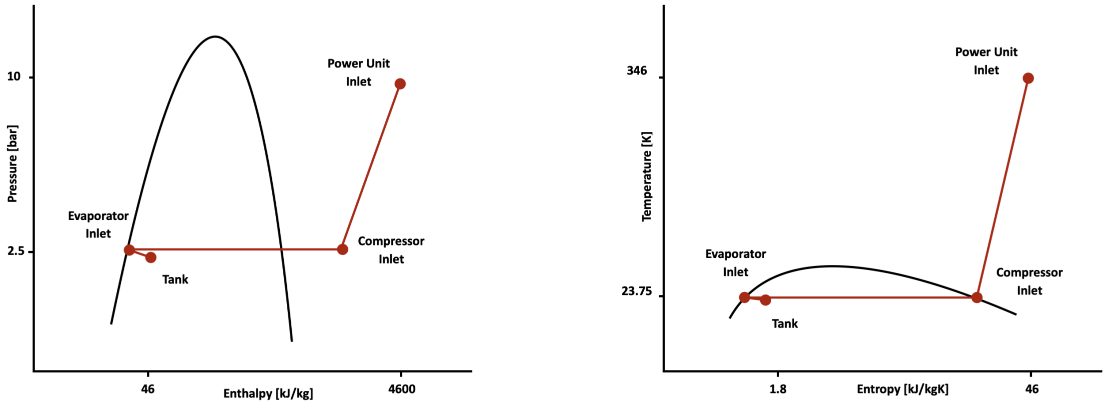

Figure 4.32: Pressure-Enthalpy (left) and Temperature-Entropy (right) state diagrams of the entire system

- Isobaric Evaporation in the Heat Exchanger
- Isentropic Compression in the Compressor

As illustrated in figure 4.32, liquid hydrogen now enters the evaporator at the tank pressure of $p_{tank} = 2.5\,bar$, where it undergoes phase change and reaches a superheated state. At this point, it enters the compressor at the intermediate temperature of $T_{int} = 220\,K$ and is compressed to the target pressure $p_{target} = 10\,bar$ and temperature $T_{target} = 346\,K$ to then reach the power unit in gaseous form.

A direct comparison between the two different systems leads to the following results shown in figure 4.33:

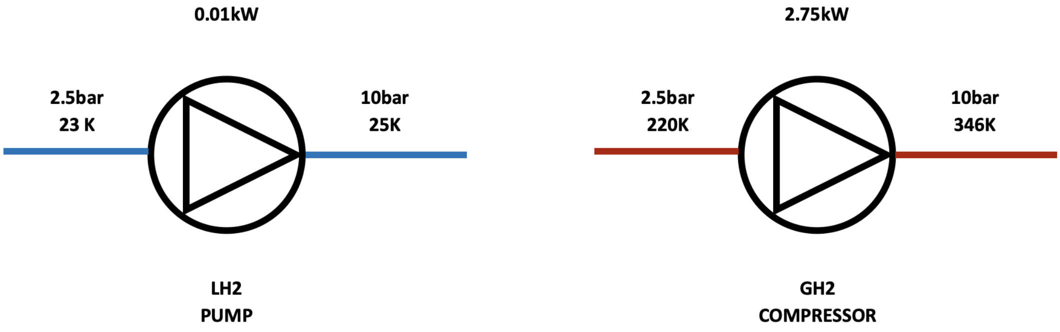

Figure 4.33: Pump (left) and Compressor (right) inlet and outlet conditions

The compression stage in this configuration is imposing a ΔT to the fluid which is much larger than the one from the pump. This is related to the fact that hydrogen is now compressed in gaseous form, such that the $\Delta T_{pump} = 2\,K$, while $\Delta T_{comp} = 125\,K$. For this reason, to keep the same boundary conditions at the entrance of the FCEV, the temperature at the outlet of the heat exchanger needs to be lowered.

Two scaling strategies were evaluated to achieve the target intermediate temperature of $T_{int} = 220\,K$:

- Channel scaling: reducing the number of channels from $n_{channels} = 40$ to $n_{channels} = 4$ while keeping the same plate geometry allows to reduce the heat rate of the evaporator to $Q = 3.2\,kW$, which results in the desired output temperature
- Plate geometry scaling: at a constant channel number, reducing the plate length to $L = 85\,mm$ and width to $W = 60\,mm$ provides the same output of the first scenario

These modifications ensure that the fluid now exits the heat exchanger at a thermodynamic state that satisfies the target conditions at the outlet of the compressor.

Additionally, compressing gaseous hydrogen also requires a lot more work from the system to achieve the target requirements in terms of pressure. In fact, due to the difference in thermal properties between the two phases, it takes up to $P_{comp} = 2.75\,kW$ as opposed to only $P_{pump} = 0.01\,kW$ to compress the fluid in ideal conditions.

5

Discussion

5.1. Full Line Model

The full line model provided an integrated perspective on the liquid hydrogen storage system and its interaction with the vehicle powertrain. This has been developed using data provided by the company regarding a preliminary study on a fuel cell electric vehicle working on gaseous hydrogen and guidelines of the FIA on the design requirements of such systems. The modular approach used enables a potential adaptation to other vehicle architectures power units, demonstrating the flexibility of this study beyond the Dallara Stradale case.

The simulation results confirmed that boil-off effects are relatively limited under the considered operating conditions. This outcome can be attributed to the adopted insulation strategy and the low mass flow rates required by the fuel cell. The predicted tank dormancy times and boil-off rates align well with the data provided by the company. This serves as a further proof of the suitability of the tank thermal model of a high performance vehicle.

Adiabatic pipes were assumed to simplify the analysis, thus isolating the primary thermal challenges to the tank and heat exchanger without introducing evaporation effects in the distribution lines. A critical finding concerns the logic of the pump-buffer interaction, which showed high sensitivity to transient changes in mass flow rate. The basic control strategy that is currently implemented highlights the pump as critical design element, requiring refined logic and experimental calibration to ensure reliable operation during all driving cycles.

Moreover, the packaging constraints of the Dallara Stradale vehicle significantly influenced system efficiency, thus affecting the comparison with the gaseous hydrogen vehicle. As the vehicle has not been originally designed with a chassis for a fuel cell, limited space was available to integrate the tank and battery systems. This resulted in reduced ranges of the vehicle, thus requiring to make specific assumptions related to the powertrain to allow to fully explore the potential of the LHSS. The power distribution strategy, with the fuel cell operating in parallel to the battery, successfully met the dynamic requirements of a racing lap but underscores the importance of a proper energy management strategy to avoid excessive stress on the fuel cell.

5.2. Tank Model

The tank model enabled a detailed investigation of heat leakage based on insulation effectiveness and of dynamic effects such as thermal stratification and sloshing. An average particle velocity across all directions to provide a first estimate of the increased heat flux due to forced convection effects. The empirical correlation used showed an increase in heat transfer coefficient, which resulted in a limited increase in overall heat flux due to the small temperature difference between the fluid and wall. The study on the insulation technology delivered results that found evidence in the literature. In particular the MLI sensitivity analysis delivered a heat flux profile at varying number of layers which followed the predictions made in literature. In practice, achieving a stable vacuum and consistent, uniform layering can be quite challenging, leading to heat leakage rates that may deviate substantially from the ideal predictions of the model. The vehicle temperature sensitivity analysis highlighted that an increasing internal vehicle temperature while driving will results in an increased heat leakage, thus reduced dormancy time.

While the model captured phase change using one boiling correlation for the fluid, it still represents an ideal scenario in which hydrogen is assumed to be a uniform two phase mixture. To capture localized effects in the subcooled and superheated areas of the tank, a 3D CFD simulation was required. This allowed to account for local temperature gradients within the fluid, demonstrating how in a dynamic condition the temperature distribution is more uniform, thus validating the hypothesis made.

Additionally, sloshing analysis provided a reasonable first approximation of the fluid dynamics within the tank. While the tool was not able to account for the phase change, it still provided a first indication on pump draft at low filling levels in dynamic driving scenarios. Together, these finding underline the need for combined 1D and 3D approaches for future work to address the combination of these effects and carry out studies to further validate the model.

5.3. Heat Exchanger Model

The heat exchanger model focused on the liquid-to-gas conversion stage, on which very little background data was publicly available. The plate-fin geometry selected for the simulation was based on a preliminary design provided by Dallara for a cryogenic heat exchanger. This configuration provided a benchmark for this study, which was oriented towards making this device work with a two-phase fluid on the main side and for the coolant on the secondary side to be integrated into the vehicle cooling cycle. The final geometry chosen for device proved to be over-dimensioned for the target temperature requirements. This was a consequence of model convergence issues related to the device discretization, thus not allowing to run the system with a more optimized configuration with a lower number of plates.

Nevertheless, the results of the vehicle cooling system integration study demonstrated the potential to reduce the fuel cell radiator size or overall fuel consumption. The latter has not been fully explored yet and would be a consequence of the fact that a reduced coolant temperature would bring the fuel cell in a more efficient operating condition, thus requiring less fuel to provide the same power output.

Calibration of the heat exchanger model remains an open task due to the lack of experimental data on two-phase refrigerants. Collaboration with industrial partners will be essential to refine the NTU-effectiveness correlations and verify effectiveness under racing-specific duty cycles.

5.4. Layout Alternative Model

Finally, the layout alternative model investigated a configuration that replaces the liquid hydrogen pump with a gaseous hydrogen compressor. This alternative was proposed due to concerns over the reliability of cryogenic pumps, which are subject to cavitation and sealing challenges. The analysis revealed a trade-off between the reduction in evaporator sizing requirements and the significant increase in power consumption associated with the compression. The preliminary results suggest that further work is required to properly assess the layout alternative configuration.

6

Conclusion and Recommendations

This thesis set out to investigate the design and performance of a liquid hydrogen storage system for a high performance fuel cell vehicle, taking the Dallara Stradale as a case study. The work addressed the system-level modeling and integration of the storage system and comparison with the conceptual study of the same vehicle but with gaseous hydrogen technology. Additionally, it focused on the design and thermal behavior of the cryogenic tank and heat exchanger, as well as the evaluation of an alternative layout using a gaseous hydrogen compressor. The overall aim was to provide a simulation framework and engineering insights that can guide the implementation of liquid hydrogen technology in future motorsport applications.

The full line model was developed to evaluate the differences between the liquid and gaseous fuel supply systems for the fuel cell electric vehicle. These two configurations were assessed in terms of range of the vehicle, which could be limited by battery and hydrogen storage capacity factors. The study demonstrated that a liquid hydrogen configuration offers a decisive advantage in terms of fuel energy density, this vehicle range compared with a gaseous hydrogen high pressure system. Despite the additional complexity of cryogenic components in terms of reliability and design requirements, the LHSS achieved boil-off rates and dormancy times within the lower range of literature data. This confirmed that careful insulation combined with low fuel mass flow demands of the power unit can keep hydrogen losses to a minimum. These results establish liquid hydrogen as a technically feasible and competitive option for motorsport vehicles, provided that packaging and thermal management are carefully managed.

The dedicated tank model was set provide insights into the influence of varying external conditions and of heat leakage on the dormancy and boil-off behavior. More, thermal stratification and fuel sloshing effects were studied to gather further knowledge on hydrogen behavior within the storage unit. The dedicated tank model quantified heat leakage under static and dynamic conditions and highlighted the critical role of MLI and vehicle temperature. The simulations showed limited sensitivity of the total heat flux to particle velocity effects because of the small temperature gradients inside the tank. Additionally, they revealed that practical MLI implementation can lead to significant deviations from ideal predictions. Some preliminary results concerning dynamic phenomena such as thermal stratification and sloshing were captured only in an approximate manner, underlining the need for combined 1D and 3D approaches in future work.

For what concerns the heat exchanger, the results show that the two key criteria considered in the model development have been respected. The design objectives based on achieving the target temperature of hydrogen were achieved using a compact plate geometry in a counter-flow configuration. More, the component was successfully integrated into the fuel cell cooling system, allowing for potential reductions in radiator size. Even though convergence issues and the absence of experimental calibration limit the current predictive accuracy, this model provided a solid benchmark for future work on the system.

At last, the layout alternative model evaluated the replacement of the cryogenic pump with a gaseous hydrogen compressor. While the compressor reduces evaporator sizing requirements and mitigates pump reliability concerns, it substantially increases electrical power consumption, which in turn impacts fuel cell and battery sizing. This preliminary study underlined the importance of evaluating different systems designs in a phase were regulations are still in the process of being made and potential to evaluate different configurations is present.

This work contributes to the field by developing an integrated 1D system model of a liquid hydrogen storage system for a racing fuel cell vehicle, capable of predicting dormancy, boil-off and transient operation. It provided a tank model that captures key heat transfer mechanisms and offers a basis for insulation sensitivity studies and operating temperature analyses. Additionally, it presented an initial heat exchanger design framework for cryogenic liquid to gaseous hydrogen conversion for motorsport applications. Lastly, it quantified the trade-offs of an alternative compressor layout, offering guidance for future FIA hydrogen class vehicle designs.

Limitations of the study reside in the fact that it is primarily simulation based and relies on simplified 1D and 3D representations and limited experimental validation. The pump control logic, the detailed physics of thermal stratification and phase change, and the calibration of heat exchanger effectiveness remain open issues. Furthermore, the packaging constraints of the Dallara Stradale imposed compromises in tank volume and battery capacity that may not fully represent future hydrogen racing prototypes.

The results of this thesis demonstrate that liquid hydrogen storage is a viable and technology for high performance fuel cell racing vehicles. Although significant engineering challenges remain, the modeling framework and design insights developed here provide a solid foundation for the next generation of hydrogen powered motorsport prototypes and contribute to the broader effort of achieving carbon-neutral racing.

6.1. Recommendations

To build on the findings of this thesis, different actions are recommended and summarized as follows:

- Full line model: the entire vehicle model could be simulated under different speed profiles, thus racing tracks as well us different power unit types and fuel consumption profiles. More, evaluate effects of valve geometries, heat transfer from piping to ambient as well as a pump map for its control. Extend the potential of the model by simulating safety related scenarios such as the purge of hydrogen as well as the tank filling process.
- Tank model: use of 3D CFD analysis to estimate the fluid to wall heat transfer coefficient in static and dynamic conditions. Additionally, implement a phase change model for sloshing simulations for greater accuracy as well as propose heat transfer models for the two phases separately and their interaction with the wall. At last, look into the loss of vacuum case and its implications in terms of design adjustments and safety concerns.
- Heat exchanger model: validate the model geometry and output characteristics by implementing calibration maps based on experimental data and geometry. Study the effects of integrating the device in other cooling cycles of the vehicle such as the one of the electric motors or battery. Look into additive manufacturing techniques to develop such systems.
- Layout alternative model: carry out a more detailed analysis on the system that provide insights into the practicability of such solution based on system-level simulations on the whole FCEV.
- Other: explore other potential design implementations of the LHSS such as the use of boil-off gas as a power source or its re-liquefaction through cryogenic refrigeration cycles.

References

[1] Muhammad Younas et al. “An Overview of Hydrogen Production: Current Status, Potential, and Challenges”. In: *Fuel* 316 (2022), p. 123317. DOI: `https://doi.org/10.1016/j.fuel.2022.123317`.

[2] United Nations Climate Change. *The Paris Agreement*. URL: `https://unfccc.int/process-and-meetings/the-paris-agreement`.

[3] Davide Calandra et al. “Management of hydrogen mobility challenges: A systematic literature review”. In: *Journal of Cleaner Production* 410 (2023), p. 137305. DOI: `https://doi.org/10.1016/j.jclepro.2023.137305`.

[4] Greg Dingle. “Sustaining the race: a review of literature pertaining to the environmental sustainability of motorsport”. In: *Journal of Sports Marketing and Sponsorship* 11.1 (2009), pp. 75–91. DOI: `https://doi.org/10.1108/IJSMS-11-01-2009-B006`.

[5] FIA Environment and Sustainability Commission. “FIA Environmental Strategy 2020-2030”. In: *Online* (2021).

[6] Extreme H. *Extreme H Race Cars Ready for Action*. 2025. URL: `https://www.extreme-e.com/en/news/1336_Extreme-H-Race-Cars-Ready-for-Action` (visited on 01/09/2025).

[7] Shell. *Forze Hydrogen Racing*. URL: `https://www.shell.com/what-we-do/technology-and-innovation/innovation-in-motorsport/shell-and-forze/forze-hydrogen-racing.html`.

[8] FIA WEC. *ACO Press Conference: key announcements*. 2024. URL: `https://www.fiawec.com/en/news/aco-press-conference-key-announcements/8003` (visited on 06/14/2024).

[9] Mission H24. *A new challenge for the H24EVO*. 2025. URL: `https://www.missionh24.fr/en/2025/01/28/a-new-challenge-for-the-h24evo/` (visited on 01/28/2025).

[10] Walter Peschka. *Liquid Hydrogen Fuel of the Future*. 1st ed. Springer Vienna, 20121.

[11] BMW. *Hydrogen - A fuel of many talents*. URL: `https://www.bmwgroup-classic.com/en/history/hydrogen.html`.

[12] Toyota. *Innovation fueled by hydrogen power*. URL: `https://www.toyota.com/h2solutions/`.

[13] Alexander Trattner Manfred Klell Helmut Eichlseder. *Hydrogen in Automotive Engineering*. 1st ed. Springer Wiesbaden, 2023.

[14] Steven Arnold Subodh Mital John Gyekenyesi. “Review of Current State of the Art and Key Design Issues With Potential Solutions for Liquid Hydrogen Cryogenic Storage Tank Structures for Aircraft Applications”. In: *NASA STI* (2006).

[15] Toyota Gazoo Racing. *Toyota reveals liquid hydrogen GR LH2 racing concept at 2025 24 hours of le Mans*. 2025. URL: `https://www.24h-lemans.com/en/news/toyota-reveals-liquid-hydrogen-gr-lh2-racing-concept-at-2025-24-hours-of-le-mans-59729`.

[16] Alexander I. Ikeuba et al. “A review on exploring the potential of liquid hydrogen as a fuel for a sustainable future”. In: *Sustainable Chemistry One World* 3 (2024), p. 100022. DOI: `https://doi.org/10.1016/j.scowo.2024.100022`.

[17] Qian Cheng et al. “Review of common hydrogen storage tanks and current manufacturing methods for aluminium alloy tank liners”. In: *International Journal of Lightweight Materials and Manufacture* 7.2 (2024), pp. 269–284. DOI: `https://doi.org/10.1016/j.ijlmm.2023.08.002`.

[18] Etienne Rivard, Michel Trudeau, and Karim Zaghib. “Hydrogen Storage for Mobility: A Review”. In: *Materials* 12.12 (2019). DOI: `10.3390/ma12121973`.

[19] The Engineering Toolbox. *Hydrogen - Thermophysical Properties*. 2008. URL: `https://www.engineeringtoolbox.com/hydrogen-d_1419.html`.

[20] Frano Barbir. *PEM Fuel Cells*. 1st ed. Elsevier, 2005.

[21] D. A. J. Rand Andrew L. Dicks. *Fuel Cell Systems Explained*. 3rd ed. Wiley, 2018.

[22] Mauro Carignano and Ramon Costa-Castelló. "Toyota Mirai: Powertrain Model and Assessment of the Energy Management". In: *IEEE Transactions on Vehicular Technology* 72.6 (2023), pp. 7000–7010. DOI: `10.1109/TVT.2023.3237173`.

[23] Kavishka Dissanayake and Dulsha Kularatna-Abeywardana. "A review of supercapacitors: Materials, technology, challenges, and renewable energy applications". In: *Journal of Energy Storage* 96 (2024), p. 112563. DOI: `https://doi.org/10.1016/j.est.2024.112563`.

[24] Seyed Ahmad Hamidi, Emad Manla, and Adel Nasiri. "Li-ion batteries and Li-ion ultracapacitors: Characteristics, modeling and grid applications". In: *2015 IEEE Energy Conversion Congress and Exposition (ECCE)* (2015), pp. 4973–4979. DOI: `10.1109/ECCE.2015.7310361`.

[25] Mahdi Soltani and S. Hamidreza Beheshti. "A comprehensive review of lithium ion capacitor: development, modelling, thermal management and applications". In: *Journal of Energy Storage* 34 (2021), p. 102019. DOI: `https://doi.org/10.1016/j.est.2020.102019`.

[26] Jean-Christophe Olivier et al. "Multiphysics modeling and optimization of the driving strategy of a light duty fuel cell vehicle". In: *International Journal of Hydrogen Energy* 42.43 (2017), pp. 26943–26955. DOI: `https://doi.org/10.1016/j.ijhydene.2017.06.243`.

[27] Xu-Feng Cheng et al. "A high step-up multiphase interleaved boost converter for fuel cells power system". In: *International Journal of Hydrogen Energy* 56 (2024), pp. 667–675. DOI: `https://doi.org/10.1016/j.ijhydene.2023.12.210`.

[28] Christopher H. Onder Lino Guzzella. *Introduction to Modeling and Control of Internal Combustion Engine Systems*. 2nd ed. Springer Berlin, Heidelberg, 2009.

[29] Soren Ebbesen et al. "Time-optimal Control Strategies for a Hybrid Electric Race Car". In: *IEEE Transactions on Control Systems Technology* 26.1 (2018), pp. 233–247. DOI: `10.1109/TCST.2017.2661824`.

[30] Roberto Lot and Simos Evangelou. "Lap Time Optimization of a Sports Series Hybrid Electric Vehicle". In: (2013). DOI: `10.13140/2.1.2166.3522`.

[31] Tadeas Sedlacek, Dirk Odenthal, and Dirk Wollherr. "Minimum-time optimal control for battery electric vehicles with four wheel-independent drives considering electrical overloading". In: *Vehicle System Dynamics* 60.2 (2022), pp. 491–515. DOI: `10.1080/00423114.2020.1823004`.

[32] Daisie D. Boettner et al. "Proton Exchange Membrane Fuel Cell System Model for Automotive Vehicle Simulation and Control". In: *Journal of Energy Resources Technology* 124.1 (2002), pp. 20–27. DOI: `10.1115/1.1447927`.

[33] Ivan Arsie et al. "Modeling and Analysis of Transient Behavior of Polymer Electrolyte Membrane Fuel Cell Hybrid Vehicles". In: *Journal of Fuel Cell Science and Technology* 4.3 (2006), pp. 261–271. DOI: `10.1115/1.2743071`.

[34] W. Peschka. "Liquid hydrogen pumps for automotive application". In: *International Journal of Hydrogen Energy* 15.11 (1990), pp. 817–825. DOI: `https://doi.org/10.1016/0360-3199(90)90018-T`.

[35] Jaroslaw Polinski. "Materials in cryogenics". In: *European Course in Cryogenics, CERN, Geneva* (2010).

[36] Ahmad Naquash, Neha Agarwal, and Moonyong Lee. "A Review on Liquid Hydrogen Storage: Current Status, Challenges and Future Directions". In: *Sustainability* 16.18 (2024). DOI: `10.3390/su16188270`.

[37] Salvador M. Aceves et al. "Safe, long range, inexpensive and rapidly refuelable hydrogen vehicles with cryogenic pressure vessels". In: *International Journal of Hydrogen Energy* 38.5 (20013), pp. 2480–2489. DOI: `https://doi.org/10.1016/j.ijhydene.2012.11.123`.

[38] Saif Z. S. Al Ghafri et al. "Modelling of Liquid Hydrogen Boil-Off". In: *Energies* 15.3 (2022). DOI: `10.3390/en15031149`.

[39] G. Petitpas. "Boil-off losses along LH2 pathway". In: *Lawrence Livemore National Laboratory* (2018).

[40] H.D. Nisanga Nuwantha, Dongho Jung, and Cheol Huh. “Improvement in predicting the thermal behavior of liquid hydrogen storage through novel thermal modeling”. In: *International Journal of Hydrogen Energy* 72 (2024), pp. 1143–1158. DOI: `https://doi.org/10.1016/j.ijhydene.2024.05.382`.

[41] Eytan J. Adler and Joaquim R. R. A. Martins. “Liquid Hydrogen Tank Boil-off Model for Design and Optimization”. In: *Journal of Thermophysics and Heat Transfer* 0.0 (0), pp. 1–15. DOI: `10.2514/1.T7005`.

[42] API Standard 520. *Sizing, Selection, and Installation of Pressure-relieving Devices in Refineries*. 8th ed. energyAPI, 2008.

[43] Jr. Weiland D.W. Adams W.F. “Heat-transfer characteristics of a water-to- cryogenic-hydrogen heat exchanger”. In: *NASA* (1969).

[44] S.P. Lynch. *2 - Hydrogen embrittlement (HE) phenomena and mechanisms*. Woodhead Publishing, 2011.

[45] Seo Yeon Kang and Seok Pil Jang. “Performance analysis of a low-pressure cryogenic vaporizer for liquified hydrogen supply system”. In: *International Journal of Hydrogen Energy* 87 (2024), pp. 1198–1206. DOI: `https://doi.org/10.1016/j.ijhydene.2024.09.050`.

[46] Ryu M. et al. “A study on thermal and flow characteristics of liquefied hydrogen heat exchanger for train using computational analysis”. In: *Journal of Mechanical Science and Technology* 38.10 (2024), pp. 5467–5477. DOI: `10.1007/s12206-024-0920-4`.

[47] Gamma Technologies. *GT Solutions for Fuel Cell Development*. 2025. URL: `https://www.gtisoft.com/fuel-cell-simulation-solutions/#1701092695613-1546384d-66c2`.

[48] Dallara. *Dallara Stradale*. 2025. URL: `https://stradale.dallara.it`.

[49] C F COLEBROOK. “TURBULENT FLOW IN PIPES, WITH PARTICULAR REFERENCE TO THE TRANSITION REGION BETWEEN THE SMOOTH AND ROUGH PIPE LAWS.” In: *Journal of the Institution of Civil Engineers* 11.4 (1939), pp. 133–156. DOI: `10.1680/ijoti.1939.13150`.

[50] Barber Nichols. *Liquid Hydrogen Pumps*. 2025. URL: `https://barber-nichols.com/products/pumps/cryogenic-pumps/liquid-hydrogen-pumps/`.

[51] Future Energy Exports. *BoilFAST - Cryogenic Boil-off Simulator*. 2025. URL: `https://www.fenex.org.au/software/boilfast/`.

[52] Lei Wang et al. “Correlations for calculating heat transfer of hydrogen pool boiling”. In: *International Journal of Hydrogen Energy* 41.38 (2016), pp. 17118–17131. DOI: `https://doi.org/10.1016/j.ijhydene.2016.06.254`.

[53] Jason W. Hartwig Samuel R. Darr. “Two-phase convection heat transfer correlations for liquid hydrogen pipe chilldown”. In: *Cryogenics* 105 (2020), p. 102999. DOI: `https://doi.org/10.1016/j.cryogenics.2019.102999`.

[54] Johnson W. Kogan A. Fesmire J. and Minnick J. “Cryogenic Vacuum Insulation for Vessels and Piping”. In: *NASA* (2010).

[55] ANSYS Inc. *Fluent Theory Guide*. 2024. URL: `https://ansyshelp.ansys.com/public/account/secured?returnurl=/Views/Secured/corp/v242/en/flu_th/flu_th.html`.

[56] W.H. Lee. “A Pressure Iteration Scheme for Two-Phase Flow Modeling”. In: *Energy Division - Los Alamos Scientific Laboratory* ().

[57] D. Makarov et al T. Kangwanpongpan. “LES model of flash-boiling and pressure recovery phenomena during release from large-scale pressurised liquid hydrogen storage tank”. In: *International Journal of Hydrogen Energy* 50 (2024), pp. 390–405. DOI: `https://doi.org/10.1016/j.ijhydene.2023.07.126`.

[58] T. E. Springer, T. A. Zawodzinski, and S. Gottesfeld. “Polymer Electrolyte Fuel Cell Model”. In: *Journal of The Electrochemical Society* 138.8 (1991), p. 2334. DOI: `10.1149/1.2085971`.

A

Model Background

Fuel Cell Loss Model

Activation Losses

These losses occur due to the electrochemical reactions at the electrodes, where electrons are transferred. They are most significant at low current densities, requiring additional energy to initiate the reactions. They are defined using the Butler-Volmer equation, which expresses the relationship between the activation overpotential and the current density as $i = f(E_{act})$.

The equation is given in an implicit form as:

$$i = i_0 \left(exp\left[\frac{\alpha_{Rd} F(E_{act})}{R_{gas}T}\right] - exp\left[\frac{\alpha_{Ox} F(E_{act})}{R_{gas}T}\right] \right) \tag{A.1}$$

where:

- E_{act}: activation losses
- i: current density
- i_0: exchange current density
- R_{gas}: universal gas constant
- T: temperature

Since equation A.1 is valid for both the anode and cathode, two different values of E_{act} are calculated. The overall activation loss is the sum of both. The exchange current density i_0 is a key parameter, representing the rate of electrochemical reactions at the electrodes. It depends on the temperature, pressure, and material properties at the reaction sites. It is typically determined under reference conditions, then adjusted to the actual boundary conditions (pressure and temperature) with equation A.2:

$$i_0 = i_0^{ref} a_c L_c \left(\frac{p_r}{p_r^{ref}}\right)^{\gamma} exp\left[\frac{E_{act}}{R_{gas}T}\left(1 - \frac{T}{T_{ref}}\right)\right] \tag{A.2}$$

where:

- i_0^{ref}: reference exchange current density (at reference temperature and pressure)
- a_c: catalyst-specific area
- L_c: catalyst loading
- p_r: reactant partial pressure

- p_r^{ref}: reference pressure of the reactant
- γ: pressure dependency coefficient 0.5 to 1
- T_{ref}: reference temperature

Given that the Butler-Volmer equation is implicit, thus computationally expensive to solve, a simplified form known as the Tafel equation A.3 is often used to estimate activation losses.

$$E_{act} = \frac{R_{gas}T}{\alpha F} \cdot \ln\left(\frac{i}{i_0}\right) \tag{A.3}$$

As shown in equation A.3, activation losses follow a logarithmic trend with respect to the current density. Figure A.1 shows how they are significant at low loads and become almost constant as the load increases.

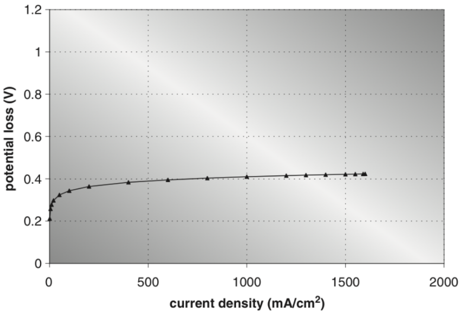

Figure A.1: Activation Losses - voltage versus current density [20]

Fuel Crossover and Internal Currents

Even when the fuel cell is at open circuit voltage, some reactants pass through the electrolyte (such as the membrane in PEMFCs), causing a small internal current. Since activation losses increase sharply at low current densities, even a small reactant crossover can result in a notable voltage drop. Using the Tafel equation A.3, the current is considered as the sum of the external current required to supply the load i_{ext} and the internal current i_{int}, which represents the fuel crossover phenomenon:

$$i = i_{ext} + i_{int} \tag{A.4}$$

From the Tafel equation A.3, considering a condition in which no load is present ($i_{ext} = 0$), the open circuit voltage loss can be expressed as:

$$E_{oc,loss} = \frac{R_{gas}T}{\alpha F} \cdot \ln\left(\frac{i_{int}}{i_0}\right) \tag{A.5}$$

Ohmic Losses

This voltage drop results from the resistance to electron flow through the electrodes, electrolyte, and other conductive components. It follows a linear relationship with current density. These losses can be quantified using Ohm's law:

$$\Delta E_{ohm} = R \cdot I \tag{A.6}$$

The resistance R in equation A.6 is not constant. It depends on the fuel cell's operating conditions, particularly the membrane humidity and the operating temperature. One of the most used models to evaluate ohmic resistance is the Springer correlation [58]. This model was developed based on an isothermal, 1D steady-state model for a PEMF using a Nafion 117 membrane. The model accounts for two primary mechanisms of water transport:

- water transport through the porous electrode
- water transport through membrane electrolyte

Water equilibrium in the membrane is determined by the water activity (a), which is evaluated as the ratio between the partial pressure of the water vapor (p_v) and the saturation pressure (p_{sat}):

$$a = \frac{p_v}{p_{sat}} \tag{A.7}$$

The water activity is a parameter needed for calculating the water content in the membrane (λ). The relationship between the water activity and the water content is not linear, such that an empirical formula is used to approximate it:

$$\lambda = 0.043 + 17.81a - 39.85a^2 + 36a^3 \tag{A.8}$$

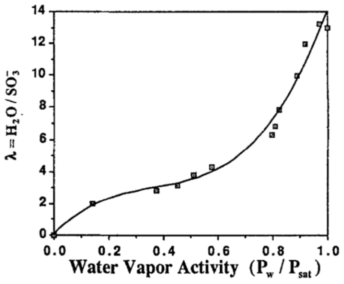

Figure A.2: Ohmic Losses - water content versus water activity [58]

In this simulation model, constant humidity along the membrane is assumed. For this reason, the water contend along the membrane thickness is given as a constant value. This allows us to compute the proton conductivity (σ), which is related to the membrane humidity, hence to the water content:

$$\sigma(T_{cell}) = exp\left[1268\left(\frac{1}{303} - \frac{1}{273 + T_{cell}}\right)\right] \cdot \sigma_{30} \tag{A.9}$$

where:

$$\sigma_{30} = b_{11}\lambda - b_{12} \tag{A.10}$$

is the experimental proton conductivity obtained at 30°C, which is a function of the water content (λ) and two calibration parameters ($b_{11} - b_{12}$). Proton conductivity is the inverse of resistance. By integrating the inverse of conductivity over the membrane thickness, it is possible to calculate the ohmic resistance of the membrane R_m as:

$$R_m = \int_0^t \frac{1}{\sigma(X(z))}dz \tag{A.11}$$

If the conditions at the anode and cathode are assumed to be constant, the ohmic resistance R_m is also constant and the ohmic loss is linearly increasing with the current.

Concentration Losses

As the fuel is consumed, its concentration decreases at the reaction sites. If the system cannot supply sufficient fuel to maintain a stable concentration, this depletion leads to a significant voltage drop, particularly at high current densities. To evaluate the concentration losses, it is necessary to begin by computing the flux of the reactants N using Fick's law:

$$N = \frac{D \cdot (C_b - C_s)}{\delta} A_{el} \tag{A.12}$$

where:

- D: diffusion coefficient of the reactants
- C_b: bulk concentration of the reactants
- C_s: concentration of the reactant at the surface catalyst
- A_{el}: electrode active area
- δ: diffusion distance

Under steady-state conditions, the consumption rate of the reactants is equal to the diffusion flux:

$$N = \frac{i}{nF} \tag{A.13}$$

From equations A.12, A.13 it is possible to obtain:

$$i = \frac{nF \cdot D \cdot (C_b - C_s)}{\delta} \tag{A.14}$$

From equation A.14, it becomes clear that the reactant concentration at the surface decreases as the current density increases. Knowing this relationship, it is possible to evaluate the current density at which the reactant consumption rate is the same as the supply rate. This condition corresponds to the maximum current available from the fuel cell as no more reactants are available to sustain the reaction. This occurs when the reactant concentration $C_s = 0$, such that the limiting current is:

$$i_L = \frac{nF \cdot C_b}{\delta} \tag{A.15}$$

Using the Nernst equation, it is possible to evaluate the concentration losses (ΔE_{conc}) as a function of the limiting current density:

$$\Delta E_{conc} = \frac{RT}{nF} \ln \left(\frac{i_L}{i_L - i} \right) \tag{A.16}$$

According to equation A.16, when the current density approaches the limiting current density, the voltage loss would have a sharp increase. However, in practice, the trend is typically more gradual than the sharp rise predicted in the equation.

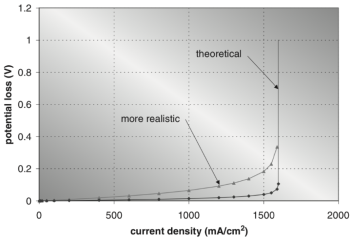

Figure A.3: Concentration Losses - voltage loss versus current density [20]